NEURAL POPULATION DYNAMICS IN PORCINE STELLATE GANGLION IN NORMAL AND HEART FAILURE STATES

by

Koustubh Bindiganavile Sudarshan

Submitted in partial fulfillment of the requirements
for the degree of Doctor of Philosophy

at

Dalhousie University
Halifax, Nova Scotia
October 2022

This thesis is dedicated to mum and dad

Table of Contents

List of Tables

List of Figures

Abstract

Neural populations in the sympathetic nervous system are involved in hierarchical closed loop control of the heart involving multiple intrathoracic ganglia. They receive afferent information from cardiopulmonary regions and process such information through various networks for cardiac control. This thesis expands on processing and networking capabilities of such neuronal populations with a focus on the stellate ganglion (SG).A large proportion of SG neurons, termed local circuit neurons, are involved in processing of cardiopulmonary information. To examine cardiopulmonary processing, approximately eight hour extracellular recordings (16 channel LMA probe) were made from the left stellate ganglion. These were considered for anesthetized healthy and heart failure pigs' neural activity along with simultaneous measurements of left ventricular pressure (LVP) and respiratory pressure (RP). Analysis of stellate population activity depended upon a novel, 'competitive masking', unsupervised spike detection algorithm. Spatial coherence analysis between populations was then estimated using events representing instances with a majority of pairs of recorded sites displaying high co-activity. Dynamic linkages between stellate population activity and cardiopulmonary information was derived from a novel, neural specificity metric.Stellate neuronal activity showed an integration of cardiopulmonary information.(i)Weak periodicity of population activity with respect to heart and respiratory rates is observed.(ii)Neural specificity to cardiopulmonary markers is independent of spiking rate and biased, relative to random sampling, toward specific LVP regions in both animal groups.(iii)Heart failure animals showed higher population spatial coherence coupled to greater variation in neural specificity compared to healthy pigs in baseline.(iv)Heart failure animals showed greater variation in neural specificity during instances of high spatial coherence than the healthy animals. These findings reveal a network whose linkage to cardiopulmonary dynamics is strongly dependent on animal status despite the general consistency of cardiopulmonary observables between animal groups. The studies of stellate architecture and their simultaneous linkages to cardiopulmonary dynamics have improved our general understanding of cardiac control. These insights should be useful to help answer questions surrounding the mechanics of ventricular arrhythmia and assess the risk of sudden cardiac death (SCD).

List of Abbreviations and Symbols Used

ANS autonomous nervous system.

ARI activation recovery interval.

CAP compound action potential.

CGRP calcitonin gene-related peptide.

ChAT choline acetyltransferase.

CSD Cardiac sympathetic denervation.

DA dorsal ansa.

DRG dorsal root ganglion.

HRP horseradish peroxidase.

ICNs intrinsic cardiac neurons.

LMA linear microelectrode array.

LSG left stellate ganglion.

LVP left ventricular pressure.

MCG middle cervical ganglion.

MI myocardial ischemia.

NGF nerve growth factor.

nNOS neuronal nitric oxide synthase.

PGP 9.5 protein gene product 9.5.

PVC premature ventricular contractions.

RP respiratory pressure.

RSG right stellate ganglion.

RTX resiniferatoxin.

SCD sudden cardiac death.

SG stellate ganglion.

SP substance P.

TH tyrosine hydroxylase.

TRPV1 transient receptor potential vanilloid-1.

VA ventral ansa.

VF ventricular fibrillation.

VIP vasoactive intestinal peptide.

VT ventricular tachycardia.

Acknowledgements

It is with genuine pleasure that I wish to thank my supervisor Dr. Guy Kember for helping me produce this doctoral work. I walked into his office just about four years back and little did I realize that I was getting into a very important and highly challenging field of research. Transitioning into a very new field, I was never made to feel intimidated or discouraged in asking questions of any kind. His passion and enthusiasm for mathematics and the field of neurocardiology has been infectious and has set me off on a quest to replicate it in my future endeavours. My greatest takeaways from working with him are persistence, dedication, humour and an uncompromising work ethic. I also had the pleasure of spending some time with Dr.Kember's family and would like to extend my gratitude to them for making me feel very welcome during my PhD.

I owe a great sense of gratitude to my co supervisor Dr. Olujimi Ajijola. He taught me a great deal about physiology and helped me raise my standards as a researcher. His knowledge, scientific approach, experience and timely advice helped me produce excellent publications along my PhD.

I would like to extend my gratitude to my thesis committee member Dr. Frank Smith. I had the pleasure of working with Dr. Smith for a term and had an excellent time learning about the background of what would be my doctoral work. His patience and empathy in guiding me through a steep learning curve along with an excellent learning plan helped me a lot during the initial stages of my PhD.

I would also like to thank Dr. Nil Gurel who has been an excellent mentor to me during the second half of my PhD. I was fortunate to work on two publications with Dr. Gurel and came out a better researcher after each of them. Her experience, integrity and a rigorous approach to science have helped me reach the end of my doctoral work.

In the department of Engineering Math, I'd like to thank Claire Chisolm for her kindness and always being accessible for any sort of help during my PhD. I'd also like to thank Dr. Farzaneh Naghibi, Dr. Gordon Fenton, Dr. Reza Rahimi, Dr. Edward

Yao and Josh Latka for being excellent instructors during my teaching assitantships with them. Lastly, I'd like to thank my office mates Jon Savoie and Alex Karavos for amazing conversations and a very professional working environment.

Most importantly, I'd like to thank my Dad Sudarshan and my mom Jyothi for being the most amazing parents. I had the greatest fortune of living with my parents for some time during my PhD. These days have been the most memorable days of my life. While I was writing my thesis, they were always there for me, shared my success and my failures and never let any sort of stress get to me. In return, I completely dedicate my doctoral work to them. I'd also like to extend my thanks to my family and friends for being very supportive in my journey and sharing my happiness and successes. Finally, I'm grateful for the sport of cricket, the Indian cricket team and my home franchise the Royal Challengers Bangalore. Knowingly and unknowingly sometimes, the game has been a part of all my life and has been a source of passion, calm and enjoyment during stressful times. I am very thankful for its existence and all the moments of the game I got to cherish with family and friends.

Chapter 1

INTRODUCTION

The autonomous nervous system (ANS) is involved in beat-beat regulation of cardiac function [6, 9]. The two parts of the ANS, the sympathetic and the parasympathetic nervous system exert cardiac control in a complex manner as opposed to a simple reciprocal manner observed in early studies. Modern findings indicate that the ANS with respect to cardiac function consists of nested feedback loops with the intrinsic cardiac ganglia, extracardiac intrathoracic ganglia, the spinal cord and higher centers. Neural interactions within and between these control centers put together are involved in beat to beat regulation of the heart. In the context of sympathetic cardiac control, beat to beat maintenance of cardiopulmonary indices such as blood pressure and respiratory pressure is referred to as regulation. Dysregulation at the level of these control centers can lead to the cardiac disease such as arrhythmia and heart failure.

This thesis is aimed at bridging the gaps in the understanding of neural interactions in the extracardaic intrathoracic ganglia, specifically the stellate ganglion with the help of healthy and diseased animal studies. Stellate ganglion neurons are thought to possess processing capabilities with respect to cardiac and respiratory information in addition to sensing cardiac mechanical and chemical stimuli [4, 5]. Understanding the processing capabilities and neural network dynamics of stellate neurons will help in furthering the current knowledge about autonomic cardiac regulation and evolution of pathology such as sudden cardiac death.

The following sections provide a review of studies that involve direct and indirect afferent pathways between the heart and the stellate ganglion, stellate ganglion as a cardiac control center, sympathetic efferent postganglionic cardiac projections through the stellate ganglion, stellate ganglion in the setting of heart failure and potential therapeutic techniques targeted at the stellate in treating sudden cardiac death due to ventricular arrhythmia.

1.1 AFFERENT INFORMATION FROM THE HEART

Afferent information from the heart is transduced through localized and functionally independent sensory neurites. The sensory neurites of cardiovascular receptors are anatomically found to be localized on the atria, ventricles, and the aorta of the dog [1]. The atrial receptors are localized in the superior vena cava, sinoatrial node region, and the upper region of the right atrium which are all sensitive to local mechanical distortion fig 1.1. These receptors are functionally grouped based on their location and the area of tissue containing the receptors. These atrial receptors contain mostly myelinated axons and project through the left stellate cardiac nerve. The ventricular receptors are located in the endocardial outflow tracts and around the ventricular anterior papillary muscle fig 1.1A and most of them have activity related to the cardiac cycle and respond to changes in epicardial stretch. These receptors may be grouped based on their behavior specific to the tissue in which they were located. Ventricular receptors also contain mostly myelinated axons and project through the recurrent cardiac nerve fig 1.1B. Mechanosensitive aortic receptors are mostly found in the ascending and arch regions of the aorta with myelinated axons that project through the dorsal cardiac nerve fig 1.1B. These aortic mechanoreceptors are also activated at different aortic pressure thresholds. Chemosensitive receptors are also found in the interventricular septum and the aortic root. Similar discharge patterns are recorded from the atrial mechanoreceptors of the cat [10]. These receptors respond to mechanical changes such as low frequency changes in length. Application of bradykinin to the endings of afferent fibers and the left atrium increased both fast conducting mechanoreceptors and slow conducting chemosensitive receptors [11]. Afferent activity recorded at the thoracic white rami and cardiac nerves also confirmed the location of various cardiac receptors distributed across the heart [12]. These receptors mostly had random discharges and responded to mechanical stimuli and changes in blood pressure.

A

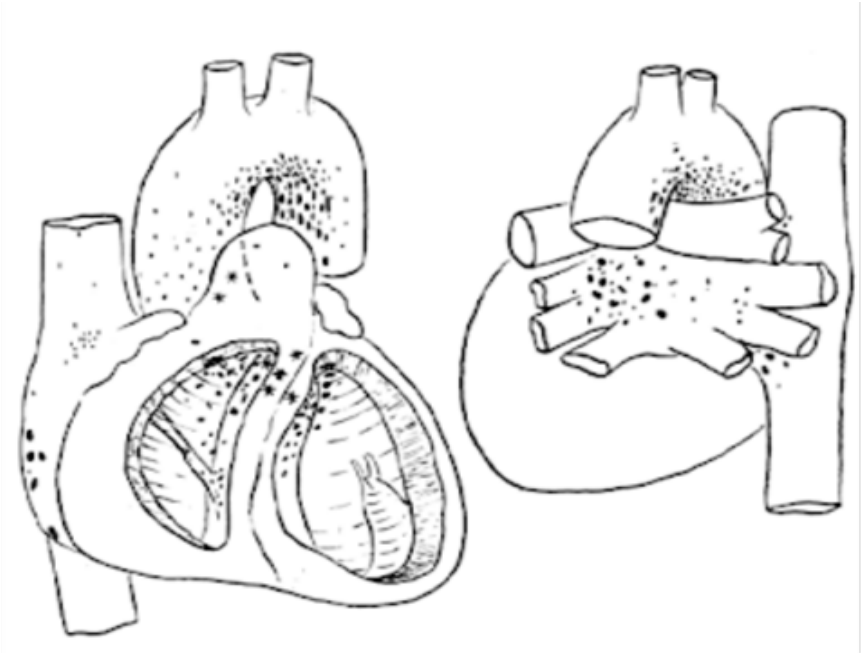

B

Receptor	Right Stellate Cardiac	Recurrent Cardiac	Craniovagal	Caudovagal	Innominate	Ventromedial	Dorsal	Ventrolateral	Left Stellate Cardiac	Total
SA node	3									3
Right atrium	4	3		5	2					14
Left atrium					4	7		1	32	44
Right ventricle		21	4	7	4					36
RV Pap muscle		13	3	3						19
Bilateral septum		1								1
Left ventricle		3			39	15			1	58
Pulmonary artery						2				2
Aorta		8			19	114	95			236
Chemoreceptor		4			10	4	2			20
Pulmonary inflation		2	2	2		2				8
Pulmonary deflation		2			10					12
(n = 32)										
Total	7	57	9	17	88	144	97	1	33	453

Figure 1.1: A : Location of sensory neurites of most cardiac afferent somata in the canine heart. The size of the markers indicate the size of the mechanosensory regions on the heart. B : Number and location of receptors on the heart and surrounding thoracic regions shown in the left column and corresponding locations in thoracic nerves is shown at the top. Taken from [1]

1.2 CARDIAC AFFERENT INFORMATION AT THE LEVEL OF THE STELLATE GANGLION

The afferent somata or neuron cell bodies of the sensory neurites which are projections from these somata described in section 1.1 are primarily located in the nodose ganglia, the dorsal root ganglion (DRG), intrathoracic extracardiac and intrinsic cardiac ganglia [13]. This section reviews the literature on anatomical pathways involving different kinds of afferent information received at the level of the stellate ganglion directly or from the spinal cord through the DRG. The afferent information is either processed within the stellate or used directly in sympathetic efferent postganglionic outflow from the stellate to the heart and the intrinsic cardiac nervous system.

Early findings indicated an anatomical pathway involving cardiac afferent information reaching the spinal cord and efferent postganglionic sympathetic fibers through myocardial responses. compound action potential (CAP) are recorded in cardiac afferent nerves following coronary artery occlusion induced in the cat [14]. This was followed by increased activity in preganglionic fibers after coronary occlusion in the dog [15]. Spontaneous impulse activity in phase with cardiac events is recorded from afferent fibers projected from the atria and the ventricles [16]. Mechanoreceptors found in the right heart and the pulmonary artery also activated myelinated and unmyelinated sympathetic afferent fibers [17]. These early findings provide evidence of pathways through the spinal cord in transducing cardiac afferent information. Cardiac responses in the form of increased myocardial contractile force is found with the stimulation of the ventral and the upper thoracic roots in the spinal cord in the dog [18, 19]. Stimulation of the right thoracic roots also increased inotropic responses in the left ventricle while the left thoracic roots caused the same response in the right ventricle.

In order to probe the characteristics of this pathway, retrograde labeling, intracellular recordings and immunoreactivity techniques were used in subsequent studies. These techniques helped isolate the location and characteristics of neuronal cell bodies receiving such cardiac afferent information, axonal projections and the neurotransmitters used in their transmissions. The next two sections will look into the literature involved in a specific link in the pathway described above. It will be focused on locating the pathway involving the DRG and the stellate ganglion.

1.2.1 THE DORSAL ROOT GANGLION PATHWAY

Cell bodies or somata receiving cardiac afferent information are labelled using retrograde injections of horseradish peroxidase (HRP) to various central and thoracic regions in animals. Injections into the middle cardiac nerve and the sympathetic trunk labelled cell bodies of afferent axons passing through the stellate ganglion. They are found to have an extensive rostro-caudal distribution (T1- T5) in the DRG [20]. The labeled cell bodies are not identified only as receiving cardiac afferent information but also from other thoracic structures including the heart. The location of afferent cell bodies projecting through the spinal cord specifically innervating the left ventricle region of the heart are located bilaterally in the DRG of the cat [21]. These cells are concentrated in the three upper thoracic spinal cord labels (T1-T3) in the DRG. More injections into cardiopulmonary afferent axons also found afferent somata in the ipsilateral DRG in the dog [22]. Small propotion of afferent neurons receiving information from different regions of the heart are labelled bilaterally in the DRG. Retrograde labeling also found small populations of ventricular afferent neurons in the DRG [23].

The DRG cardiac afferent neurons receive varying degrees of mechanical and chemical afferent stimuli. Activity recorded from spontaneously active DRG afferent neurons with epicardial neurites responded to both mechanical and chemical stimuli [24]. These neurons also responded to adrenergic agents at the level of the sensory neurites indicating an important role in cardiac feedback with local catecholamine release. Portions of these neurons being immunoreactive to individual or colocalized transmitters such as substance P (SP), calcitonin gene-related peptide (CGRP) and neuronal nitric oxide synthase (nNOS) indicated a diverse variety of neurotransmitters used by these afferent neurons.

These findings provide evidence to cardiac afferent information reaching the DRG and also reaching the stellate ganglion either through synaptic connections or axonal projections. The next section deals with the stellate ganglion as a control center for cardiac regulation. Literature finding anatomical connections between the DRG and the stellate ganglion, between the stellate and the heart as efferent outflow and processing of cardiac information within the stellate will be explored in the next section.

1.2.2 STELLATE GANGLION AS A CARDIAC CONTROL SYSTEM

Early works investigating the possibility of a cardiac peripheral reflex involving the stellate ganglion found synaptic connections in the cells of the cat stellate ganglion in response to excitation of axons in cardio-pulmonary regions [25]. A combination of in vitro and in situ intracellular recordings were conducted to record the synaptic responses of individual stellate cells. These responses indicate an integration of central and peripheral excitatory inputs in the stellate as well as a close association of stellate neuron activity with the cardiac and respiratory cycle. Following studies used more retrograde labeling injected into various locations of the stellate to identify the location of neurons receiving cardiac afferent information. Fewer neurons are found to be the origin of cardiopulmonary nerves in the stellate ganglion compared to the middle cervical ganglion (MCG) after retrograde labeling [2]. Most of the labelled neurons found in the stellate are regional to its cranial pole shown in fig 1.2 A. Fluorescent retrograde tracers injected in to the right atrium, right ventricle, inferior vena cava and right atria ganglionated plexus located sympathetic efferent neurons in the cranial region of the stellate innervating the porcine heart (fig 1.2B) [3].

Further electrophysiological studies recorded CAPs in efferent cardiopulmonary nerves following the stimulation of an ipsilateral afferent cardiopulmonary nerve in both acutely [26] and chronically decentralized canine stellate ganglia [27]. Such CAPs recorded in efferent cardiopulmonary nerves suggest synaptic connections in intrathoracic ganglia such as the MCG and the stellate ganglion. More synaptic connections are suggested to be present in the MCG than in the stellate ganglion due to the nature of the recorded CAPs. The possibility of the existence of multiple types of neurons such as direct afferent, and efferent neurons in the intrathoracic ganglia is explored due to CAPs generated following decentralization. Intracellular recordings made in the stellate found excitatory synaptic input from the ventral ansa (VA) , dorsal ansa (DA) and the stellate cardiac nerve in line with previous findings [28]. Activity recorded from the DA following afferent input applied to the stellate cardiac nerve further substantiated the presence of synaptic connections in the stellate ganglion. These results indicate an important role played by the neurons in the stellate towards the existence of a possible peripheral function such as a cardiac reflex. This led to more studies directly probing the activity and responses elicited by various

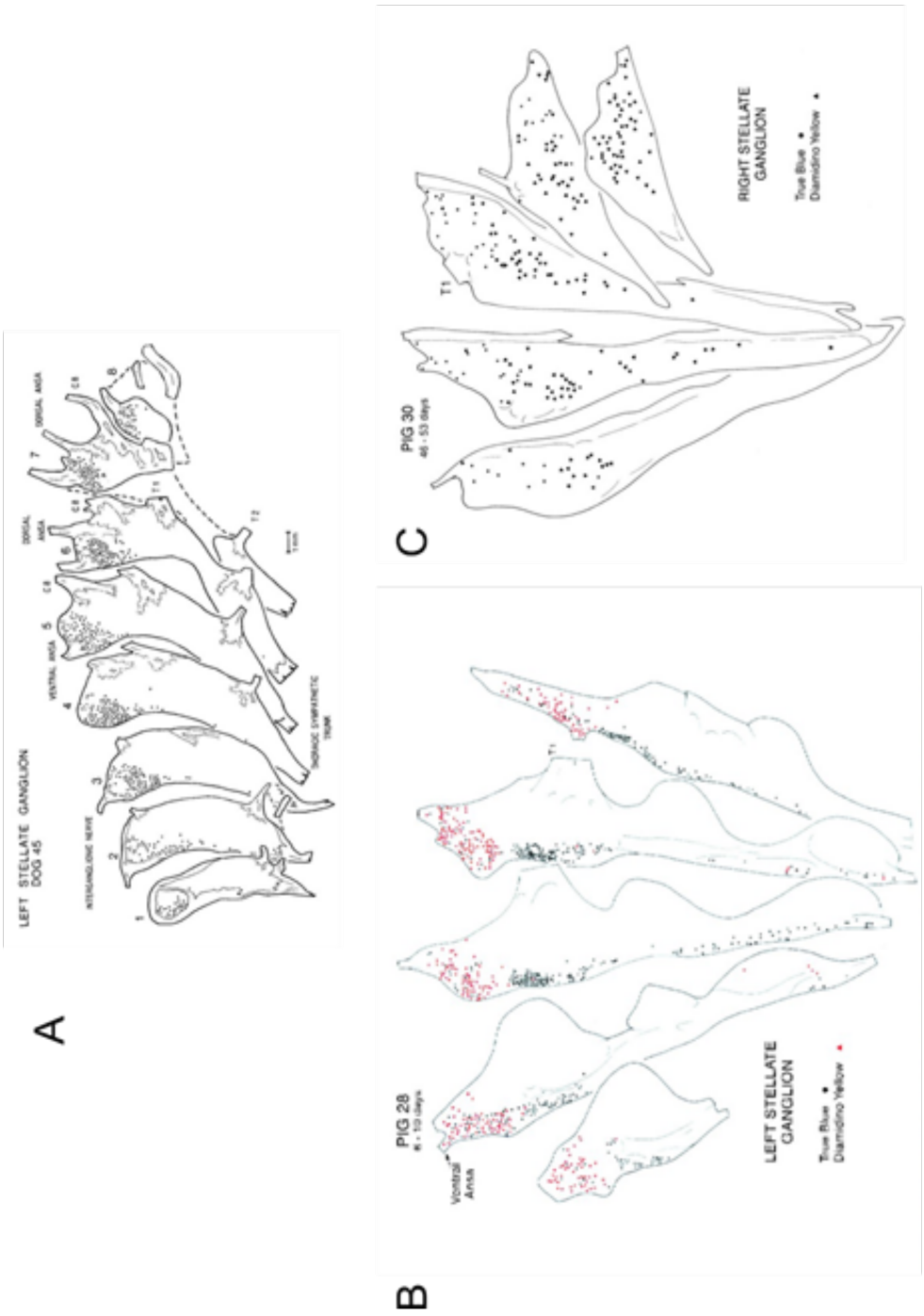

Figure 1.2: A: Efferent neurons in the cranial pole of the left stellate ganglion (LSG) following HRP injection into cardiopulmonary nerves [2].B- C :Efferent neurons in the cranial region of LSG and right stellate ganglion (RSG) using fluorescent retrograde tracers [3]

intrathoracic ganglia neurons.

Spontaneous activity is recorded with in situ extracellular recordings from both an intact and an acutely decentralized stellate of the dog [4]. These spontaneously active stellate neurons are closely associated with the cardiac and respiratory cycle and also respond to mechanical distortions in regions near the heart and the great thoracic vessels (Table 1.3). Most of these spontaneously active neurons are also unresponsive to cardiopulmonary nerve or vagosympathetic trunk stimulation. This hints at the possibility of the presence of function specific interneurons in the stellate. Further intracellular recordings from stellate neurons following chronic decentralization showed persistence in stellate activity after cardiac afferent nerve stimulation [29]. These findings obtained directly from the stellate confirmed the existence of cardiac afferent cell bodies in the peripheral ganglia. The results of the study also implied cardiac regulation occurring with the help of the intrathoracic ganglia independent of the central nervous system. More recent findings using immunofluorescent staining on the stellate ganglion found only a small proportion of cardiac afferent neurons fig 1.4. Various sites called varicosities are observed indicating sites of possible afferent to efferent neurotranmsission.

Stimulation of distinct regions in all the intrathoracic ganglia including the stellate elicited chronotropic, inotropic or both types of cardiac responses [30]. The effects of sympathetic postganglionic efferent axons was separated from those of the preganglionic axons using hexamethonium injected into an acutely decentralized stellate. Hexamethonium is a nicotinic receptor antagonist that is used in ganglionic blockage in the study. Different regions of the stellate elicited consistent, sporadic or no cardiac responses. The right stellate was mostly both chronotropic and inotropic in its response while the left stellate was mostly inotropic. Regions of the stellate without any efferent postganglionic neurons are also involved in cardiac responses. These findings along with cardiac responses elicited due to stimulation of clusters of neurons along a cardiac nerve further suggested the possibility of the existence of interneurons or functionally different neurons in the stellate. This possibility is further explored by retrograde labeled neurons with shorter axon projections separating them from their efferent counterpart within the caudal region of the cat stellate ganglion [31]. This was opposed to the finding of long axon projections found in the cranial pole

TABLE 1. Stellate ganglion neurons (145 neurons in 36 dogs)

	Number	% of total
Spontaneously active neurons		
Respiratory related (total)[a]	41	28
Active during inflation	32	
Active during deflation	7	
Active during zero pressure	2	
Cardiovascular related (total)[b]	28	19
Isovolumetric contraction	12	
Isovolumetric relaxation	19	
Systolic ejection	13	
Diastole	3	
Neurons activated by distortion of		
Thorax or abdominal wall	30	21
Neck	26	18
Pulmonary tissue[c]	26	18
Cardiovascular organs (total)[d]	16	11
Superior vena cava	1 (6%)	
Heart	4 (25%)	
Aorta	11 (69%)	
Left foreleg	15	10
Adjacent mediastinum	5	3

Figure 1.3: A large number of spontaneously active neurons located in the stellate ganglion are associated with cardiac/respiratory cycle and various mechanical distortions [4]

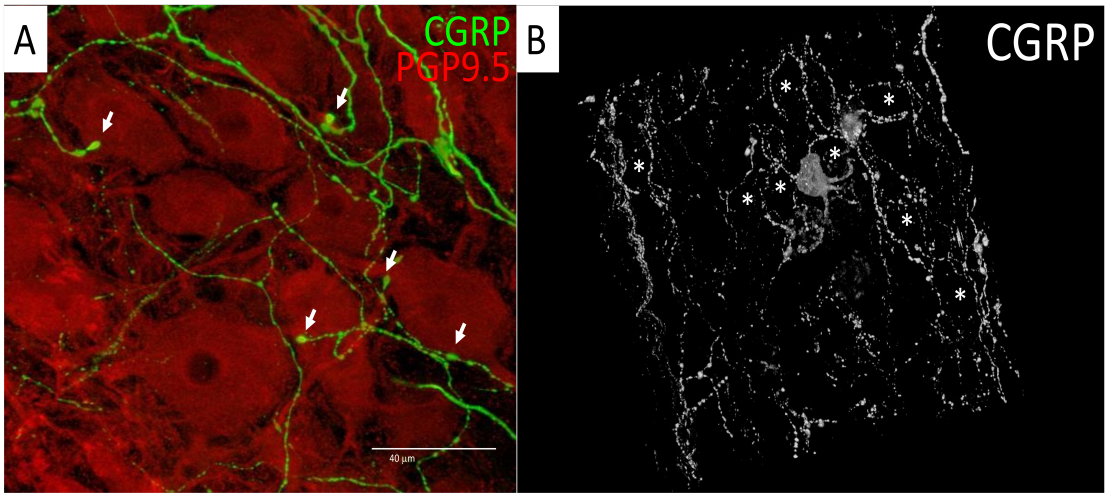

Figure 1.4: (A) Stellate ganglion neurons identified by immunofluorescent staining (red - identified by PGP9.5 staining), and adjacent afferent fibers marked by green (CGRP staining). Possible locations of afferent to efferent neurotransmission called Varicosities, are marked by white arrows. (B) Network of afferent fibers (white) shown with a lower magnification image in the stellate ganglion. The sites of some neurons, marked by the asterisk (*), show that most of the neurons are adjacent to afferent fibers [Obtained from Dr. Olujimi Ajijola]

of the stellate corresponding to neurons involved in efferent postganglionic outflow to cardiopulmonary nerves. The findings from this study further led to more studies probing the characteristics of such functionally different neurons present in the stellate ganglion and their role in the modulation or processing towards sympathetic efferent activity.

Immunoreactive studies were carried out in order to probe into characteristics such as the neurotransmitters used by various neurons in the stellate ganglia. Various neuropeptide-like immunoreactivity is found in both the right and the left stellate ganglia after chronic decentralization [32]. The distribution of this immunoreactivity is distinct from the distribution of efferent postganglionic neurons. Changes in cardiac response observed from stellate stimualtion and other intrathoracic nerves is nicotinic and cholinergic in nature [33]. Neurons present in the stellate are also involved in eliciting cardiac responses following the administration of neurochemicals such as acetylcholine, nicotine and isoproterenol [34]. These neurons are located in multiple loci in the stellate without a definitive distribution. Administration of substance P and vasoactive intestinal peptide (VIP) to the acutely decentralized stellate ganglia induced chronotropic and inotropic responses [35]. These peptide modification of cardiac responses in the stellate ganglion cease after β - adrenergic receptor ganglionic blockage.

The characteristics of such intrathoracic ganglia neurons and their influence on cardiac myocytes were further studied in vitro using a model with intrathoracic neurons co cultured with cardiac myocytes [36]. This model was effective in studying the intrathoracic neurons as well as the myocyte cells independently. Using this model, nitric oxide sensitive neurons increasing the beating rate of myocytes are found in the stellate ganglion [37]. Nitric oxide did not affect the myocytes cultured alone indicating a neurotransmitter mechanism for extracardiac intrathoracic neurons controlling the myocardium beating rate. Using the same model, stellate ganglion neurons co cultured with adult guinea pig myocytes and cultured alone in vitro exhibited various morphological characteristics and were immunoreactive to multiple neurochemicals such as tyrosine hydroxylase (TH), protein gene product 9.5 (PGP 9.5), choline acetyltransferase (ChAT) etc [38]. Cardiomyocyte responses are also elicited to ANG II administration both in an acutely decentralized stellate in situ and in vitro

using cocultured intrathoracic neurons with myocytes [39]. These findings indicate ANG II sensitive neurons present in the stellate ganglion known to cause increased chronotropic and inotropic effects in the heart [40].

Previous studies served to further the understanding of the characteristics of the stellate neurons and their role in a cardiac peripheral reflex. More recent studies looked at population activities to represent activities from different intrathoracic ganglia. The population activity represented by spiking activity for an intrathoracic ganglia recorded over a long duration was analysed using cross correlation. The cross correlation analysis between all the major extracardiac intrathoracic ganglia and intrinsic cardiac ganglia did not reveal any coherence among their populations [5]. Ventricular epicardial mechanical stimuli did not alter stellate activity but altered that of the MCG and the intrinsic cardiac neurons (ICNs). Altering cardiac after load by occlusion of the aorta reduced the basal stellate activity while all extracardiac activity including the stellate activity were completely removed following acute decentralization. The activity in all the intrathoracic ganglia was modified by epicardial chemical stimuli in the form of substance P and purinergic agents. These effects are suppressed in the extracardiac intrathoracic ganglia following acute decentralization. Acute ischemia induced by coronary artery occlusion also affected the stellate activity. The effects of multiple interventions on hemodynamics, stellate activity and intrinsic cardiac activity can be found in the table below (Table 1.5). These findings indicated complex, nested feedback loops present in the peripheral nervous system with differential control over cardiac function. As presented in these results, these hierarchical cardiac control loops were found to be capable of functioning independently of the central nervous system.

These findings lay the foundation of the modern view of autonomic cardiac control seen in fig 1.6. This modern view consists of multiple control centers located in the central nervous system, extracardiac intrathoracic ganglia and the intrinsic cardiac ganglia with the help of a variety of neurotransmitters in their transmission [6]. This multiple decentralized control centers of cardiac function will be referred to as the cardiac neuraxis in the following sections.

The cardiac neuraxis focused on the stellate ganglion is also described in 1.7. Multiple cardiac reflexes at the level of multiple cardiac control centers, afferent and

Intervention	HR, beats/min	LAP, mmHg	RV IMP, mmHg	LV IMP, mmHg	LVP, mmHg	Stellate Activity, impulses/min	Intrinsic Activity, impulses/min
Control	122 ± 3	10 ± 1	24 ± 1	101 ± 9	114 ± 7	32 ± 8	20 ± 4
Epicardial touch	122 ± 3	10 ± 1	24 ± 1	101 ± 9	114 ± 7	47 ± 11	39 ± 9*
Control	117 ± 9	10 ± 2	28 ± 1	106 ± 6	112 ± 3	28 ± 9	29 ± 6
Substance P	117 ± 8	10 ± 2	28 ± 1	106 ± 6	112 ± 3	78 ± 22	132 ± 25*
Control	118 ± 7	9 ± 1	25 ± 1	94 ± 8	114 ± 6	36 ± 12	23 ± 11
Purines	118 ± 7	9 ± 1	25 ± 1	94 ± 8	114 ± 7	83 ± 27*	95 ± 23*
Control	128 ± 7	11 ± 1	21 ± 1	101 ± 8	112 ± 5	49 ± 6	21 ± 3
Respiration off	128 ± 7	11 ± 1	21 ± 1	101 ± 8	112 ± 5	32 ± 5*	11 ± 2*
Control	133 ± 7	9 ± 2	25 ± 2	93 ± 13	117 ± 7	28 ± 4	27 ± 8
CC Aorta	118 ± 12	10 ± 2	25 ± 2	128 ± 17*	181 ± 9*	13 ± 3*	113 ± 32*
Control	116 ± 9	10 ± 1	24 ± 1	88 ± 10	1114	33 ± 4	22 ± 9
CC Aorta (decentral)	118 ± 10	10 ± 1	28 ± 2	134 ± 16*	161 ± 6*	28 ± 6	117 ± 37*
Control	120 ± 10	10 ± 1	24 ± 1	95 ± 12	114 ± 6	21 ± 10	26 ± 4
Isoproterenol	145 ± 9*	11 ± 1	70 ± 1*	172 ± 21*	126 ± 10	60 ± 19	112 ± 24*
Control	119 ± 10	11 ± 1	23 ± 2	98 ± 12	112 ± 6	30 ± 5	26 ± 2
Isoproterenol (decentral)	150 ± 11*	11 ± 1	50 ± 5*	167 ± 17*	120 ± 10	33 ± 5	74 ± 12*
Control	119 ± 8	10 ± 1	25 ± 1	96 ± 10	115 ± 5	33 ± 9	19 ± 3
Dobutamine	128 ± 9	11 ± 1	70 ± 9*	173 ± 20*	146 ± 9*	32 ± 6	97 ± 24*
Control	111 ± 9	10 ± 2	28 ± 1	104 ± 6	108 ± 3	36 ± 8	18 ± 6
Coronary artery Occ	111 ± 9	10 ± 2	28 ± 1	90 ± 13	106 ± 2	30 ± 6	61 ± 5*
Control	107 ± 7	10 ± 1	28 ± 1	100 ± 5	106 ± 3	29 ± 4	18 ± 4
Coronary artery Occ (decentral)	107 ± 7	10 ± 1	28 ± 2	85 ± 11	104 ± 2	30 ± 4	33 ± 7

Values are means ± SE ($n = 8$ dogs/intervention). Changes in HR, LAP, RV IMP and LV IMP, LVP and neuronal activity are tabulated. Responses elicited by touching epicardial sensory fields as well as sensory field application of substance P and purines (adenosine and ATP) are tabulated as the effects of respiratory cessation (Respiration off), cross clamping of the aorta (CC Aorta), and dobutaine and isoproterenol before and after decentralization (decentral) of the intrathoracic autonomic ganglia. Effects of brief occlusion of the left ventral descending coronary artery (Coronary artery Occ) before and after decentralization are also presented. * $P < 0.05$ control vs. intervention.

Figure 1.5: Spontaneous activity generated by various intrathoracic neurons including the stellate ganglion neurons and corresponding responses to different mechanical and chemical interventions performed in the study. Taken from [5]

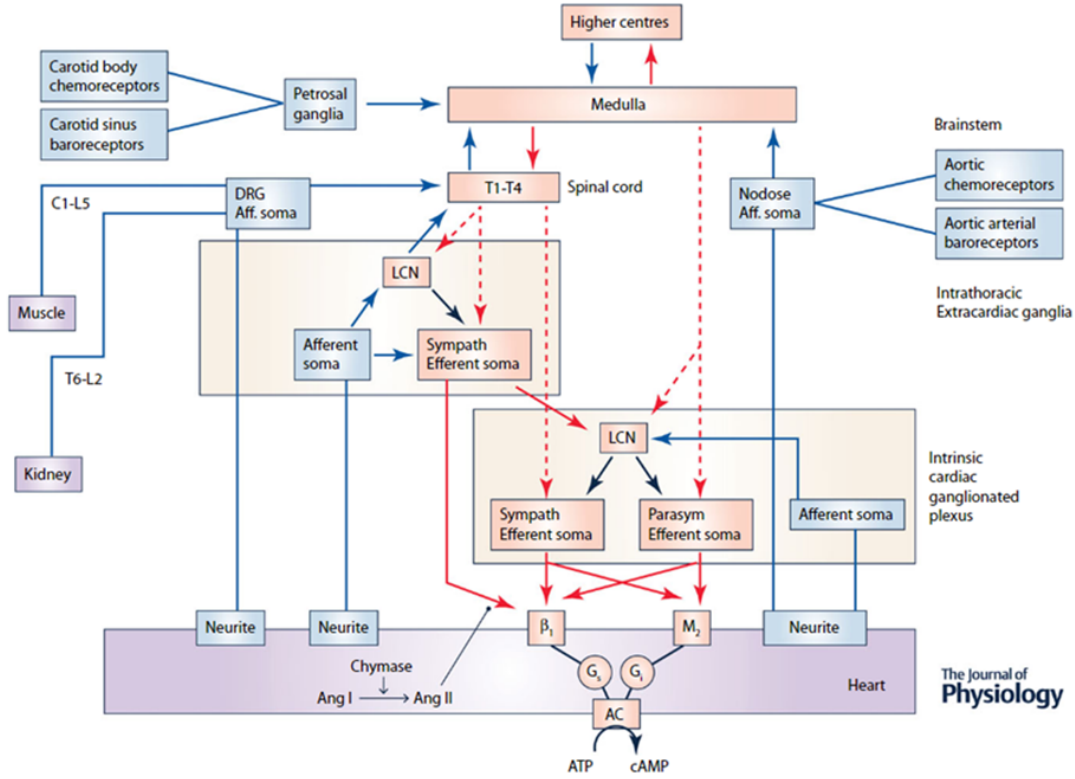

Figure 1.6: Schematic organization of the cardiac nervous system control of cardiac function. Aff: afferent; β, β: adrenergic receptor; C: cervical; DRG: dorsal root ganglion; Gi: inhibitory G-protein; Gs: stimulatory G-protein; L: lumbar; LCN: local circuit neuron; M2: muscarinic receptor; T: thoracic. Taken from [6]

efferent pathways involving the stellate are described. These anatomical pathways and control centers form the cardiac nervous system.

1.3 STELLATE GANGLION IN HEART FAILURE

While the previous sections established the stellate ganglion as a control center in healthy hearts, this section will review the role of the stellate in heart failure. With respect to heart failure, this thesis attempts to further the understanding of sudden cardiac death resulting from lethal ventricular arrhythmia by probing stellate network activity. Hence, only studies with myocardial infarction and ventricular arrhythmia models of heart failure are reviewed in this section to limit the scope of this thesis. A brief anatomical review will be presented on the efferent sympathetic projections from the stellate ganglion to the heart. This will serve to establish a sympathetic efferent postganglionic pathway from the stellate and the extent of stellate - cardiac innervation.

1.3.1 SYMPATHETIC EFFERENT POST GANGLIONIC CARDIAC INNERVATION

Electrical stimulation of the stellate ganglion was used as the primary technique to localize its efferent postganglionic sympathetic projections. Early studies observed changes in electrocardiographs and ventricular refractory periods following unilateral stellate ganglion stimulation and stellate ganglionectomy [41]. The removal of bilateral stellate ganglia prolonged refractory periods in different regions of the ventricles. These early findings indicated a possibility of rich cardiac innervation through bilateral stellate ganglia. More evidence of cardiac innervation was obtained by further anatomical studies. Surgical denervation of the epicardium removed contractile responses in localized regions of the heart following bilateral stellate ganglion stimulation in the dog [42]. From this technique, the left ventricle was found to be innervated majorly from tissues along the left anterior descending artery while the right ventricle was innervated by the right A-V groove. These cardiopulmonary nerves were found to be anatomically part of the sympathetic ganglia providing more evidence for cardiac innervation by the stellate. Another technique involving electrical stimulation of the stellate and different regions of the ventro lateral cardiac nerve changed contractile

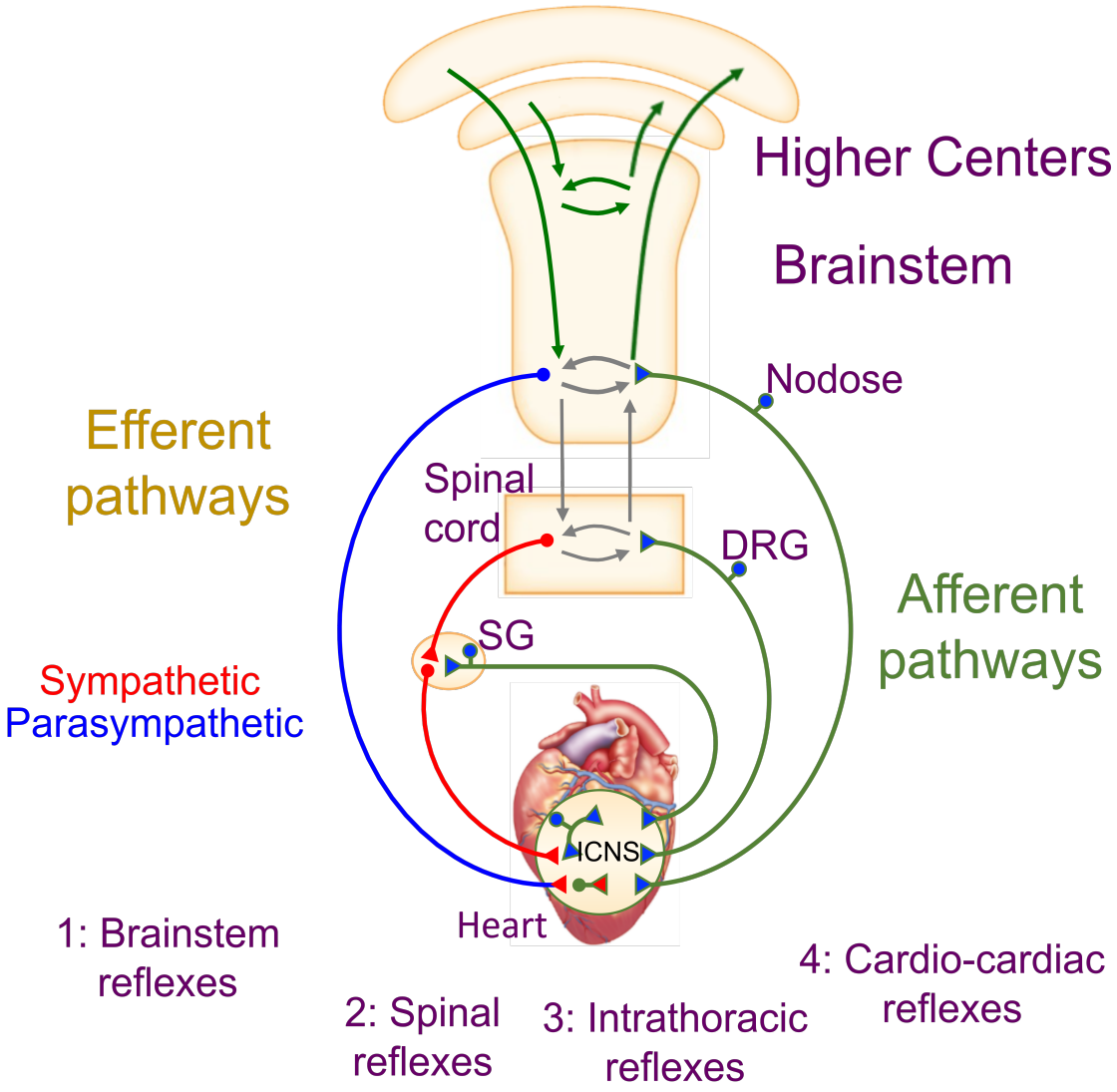

Figure 1.7: Modern view of the cardiac nervous system – The cardiac nervous system contains multiple centers involved in feedback loops for cardiac control. These control centers are present in the central nervous system, the extracardiac intrathoracic ganglia and the intracardiac nervous system. DRG: dorsal root ganglion; SG: stellate ganglion ; ICNS: intracardiac nervous system. Taken from [7].

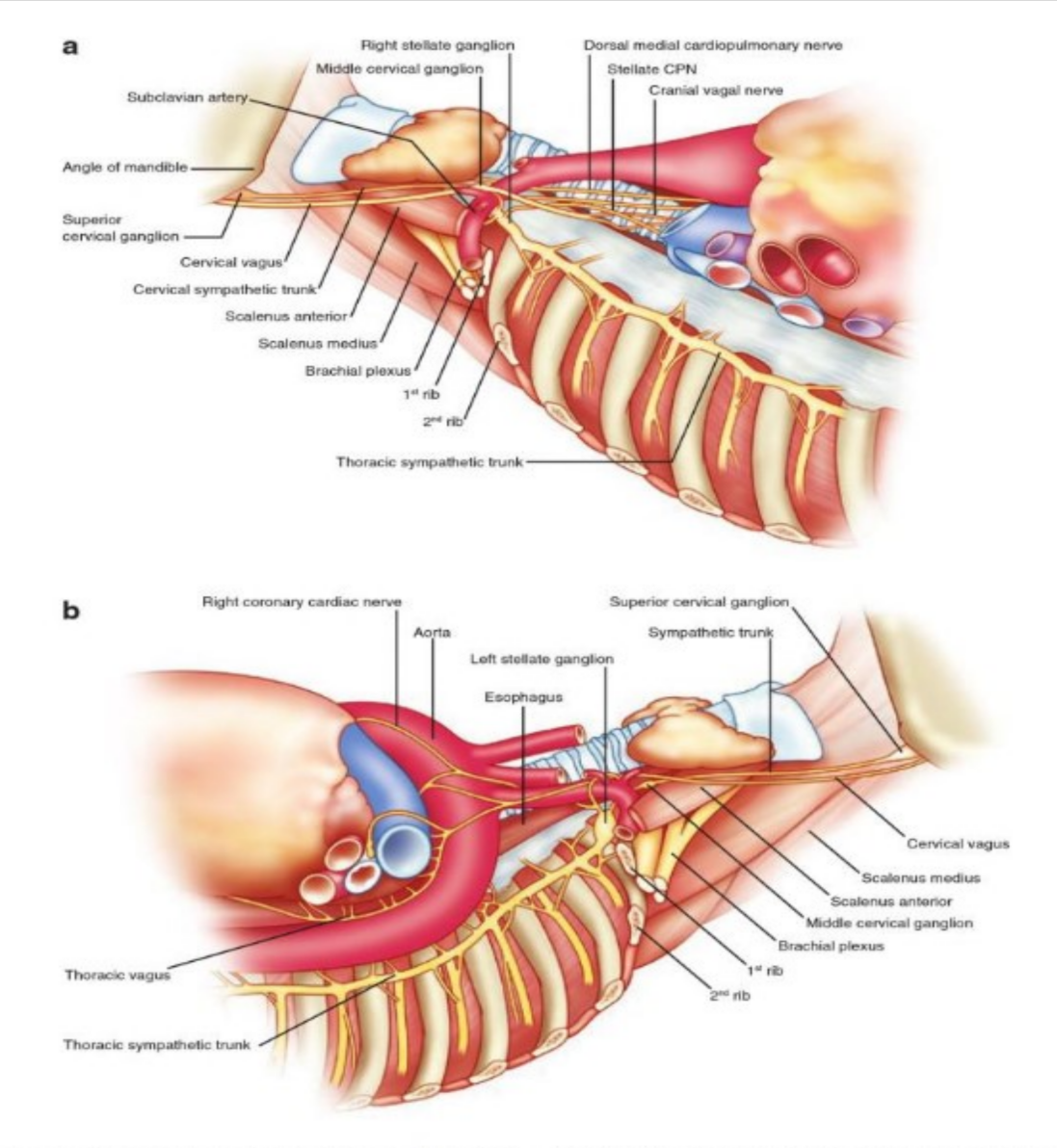

Figure 1.8: Right(a.) and Left(b.) view of cardiac nerves from the neck and the thorax localizing bilateral stellate ganglion. Bilateral stellate and middle cervical ganglion contain most of the cardiopulmonary nerves that make up the sympathetic postganglionic efferent projections to the heart. Non cardiac sympathetic postganglionic efferent projections to the esophagus, trachea and other structures in the head and the neck can also be found in the stellate ganglion. Taken from [8]

force and caused tachycardia [1]. More cardiovascular responses recorded from multiple thoracic autonomic nerve stimulation further localized the efferent sympathetic nerve endings in the dog [43]. Sympathetic efferent nerves are in a small number in the stellate cardiac nerve and increased both rate and force of contraction in the heart. The ventrolateral view of the major cardiac nerves along with the location of the stellate ganglion is shown in fig 1.8. More studies with electrical stimulation of different cardiac nerves shortened the ventricular refractory periods in localized regions of the myocardium of the dog [44]. Further exploration of sympathetic projections involved in chronotropic (rate) and inotropic (force of contraction) responses by ansa subclavia stimulation also revealed distinct sympathetic efferent projections to different types of tissues in the heart [45]. The origin and pathways of various autonomic nerves were also identified using microscopy in human cadavers [46]. These studies provided an anatomical basis for understanding the role of the stellate in cardiac control in normal and stressed conditions. An exhaustive anatomical review containing histological and immunohistochemical techniques in locating neurons in the cardiac neuraxis, sympathetic and parasympathetic projections to the heart and other thoracic structures can be found in the cited review [7].

1.3.2 REMODELING IN THE STELLATE GANGLION IN HEART FAILURE

Abnormal anatomical and electrical remodeling is observed in the sympathetic nervous system in diseased states such as myocardial ischemia (MI) and heart failure. Spontaneous ventricular tachycardia (VT), ventricular fibrillation (VF) and sudden cardiac death (SCD) are recorded in dogs with chronic MI and atrioventricular block induced using coronary artery occlusion and catheter ablation [47]. Mechanistically, remodeling in the form of increased sympathetic nerve density and nerve sprouting is implicated in heart failure [48, 49]. Heart failure models based on increased nerve growth in the stellate induced abnormal electrophysiogical changes in the heart [50, 51, 52]. Mechanisms such as action potential prolongation in the atria and the ventricles, down regulation of K currents, abnormal Ca2+ handling are implicated in lethal cardiac arrhythmias in patients with heart failure [53].These findings represent early works probing into the role of abnormal sympathetic activity in the generation

of ventricular arrhythmia and sudden cardiac death.

Direct electrical and anatomical changes in the stellate neurons are observed in MI models. Acute and chronic MI induced neural, electrical and anatomical modeling in the stellate ganglia in both animals and humans. Acute MI induced electroanatomical remodeling in both the left ventricle and the stellate ganglion neurons in the form of increased synaptic density and increased activity in the dog [54]. This also resulted in neural remodeling of bilateral stellate ganglia in the rabbit in the form of nerve sprouting and increased serum NGF levels [55]. Acute and chronic MI also induced changes in the form of increased neuron size in humans and alterations in peptide immunoreactivity in bilateral stellate ganglia of the pig [56, 57, 58]. A more exhaustive review of neural remodeling in response to heart failure and therapies targeted at different levels of the cardiac neuraxis can be found in the cited review [59].

Due to abnormal sympathetic activation, possibly from such aberrant remodeling occurring at the level of the stellate, heterogeneous electrophysiological responses are observed in the myocardium. Direct and reflex sympathetic activation increased regional differences in ventricular repolarization with the reflex activation showing greater activation recovery interval (ARI) dispersion in humans with cardiomyopathy [60]. Although reflex sympathetic stimulation was perfromed with the help of nitroprusside infusion, there is a possibility of the effect of increased sympathetic drive through the stellate on ventricular repolarization. Directly stimulating the LSG and the RSG shortened the after ARI and increased norepinephrine concentrations in the anterior left ventricle wall of the porcine heart [61]. In an another myocardial ischemia (MI) model, alterations in repolarization dispersion, ARI intervals and activation propagation are observed [62]. Shortening of ARI and increased dispersion of repolarization is also observed in the endocardium and epicardium of the left ventricle following left, right and bilateral stellate stimulation [63]. T peak - T end interval, seen as a marker for sudden cardiac death, is prolonged and associated with dispersion of repolarization in the heart.

1.4 THERAPIES TARGETED AT THE STELLATE GANGLION

Increased sympathetic tone, decreased parasympathetic tone and structural alterations in the heart are known to elicit ventricular arrhythmia leading to sudden

cardiac death [64, 65, 66, 67, 68]. Therapies developed to address such imbalances in sympathetic tone and effects from structural changes in the heart have been explored in more recent studies. Two therapies targeted at the stellate-cardiac pathway - Cardiac sympathetic denervation (CSD) and blockage of abnormal cardiac afferent information in the treatment of ventricular arrhythmia and sudden cardiac death have been reviewed in this section.

CSD has been used as therapy for patients with ventricular tachycardia refractory to other pharmacological treatments. Bilateral cardiac sympathetic denervation was helpful for patients with ventricular arrhythmias [69]. Bilateral cardiac sympathetic denervation was also more beneficial than unilateral CSD for patients with VT storm or recurrent VTs [70]. Cardiac sympathetic denervation decreased sustained VT in patients with refractory ventricular arrhythmia [71].The possibility of reducing increased afferent signalling as part of reducing abnormal sympathetic drive has been explored in more recent studies. A novel therapy involving the epicardal application of resiniferatoxin (RTX) in order to deplete transient receptor potential vanilloid-1 (TRPV1) afferent fibers signalling has been recently studied [72]. Depletion of cardiac TRPV1 afferents reduced ventricular arrhythmias after MI in the porcine heart . TRPV1 depletion also reduced fibrosis and electrical instability in the MI scar border zone. Increased sympathetic tone indicated by stellate ganglion activity is also normalized by the TRPV1 afferent depletion. However, RTX application only helped remove ventricular dysfunction in the form of PVC induced cardiomyopathy in the short term [73]. Application of RTX serves to be a promising therapy technique in treating heart failure.

More therapy techniques used in the treatment of ventricular arrhythmia can be found in the cited reviews [6, 9, 74].

1.5 THESIS GOALS

All the different findings in the above studies point to a clear role played by the stellate in the generation of ventricular arrhythmia leading to potential therapies targeted at the stellate ganglion. While the nature of stellate neurons has been explored extensively, the extent of network processing within the stellate is largely unknown. Previous in vivo extracellular studies probing into stellate ganglion function have

been limited by episodic experiments and elemental spike detection techniques. In this thesis, novel techniques for spike detection, spatial coherence and neural-target bias have been explored with the help of continuous recordings of stellate activity in baseline and during cardiopulmonary stressors both in normal and heart failure pigs.

The following hypotheses have been examined in the thesis

- Stellate ganglion populations exhibit an integration of cardiopulmonary function
- Stellate population activity is biased towards specific phases of the cardiac and respiratory cycle in baseline.
- Heart failure animals exhibit greater temporal events of high spatial coherence in spiking activity across recorded channels in stellate activity compared to normal animals in baseline.
- Heart failure animals exhibit higher entropy representing uncertainty in change in neural specificity with respect to LVP compared to normal animals in baseline

Chapter 2

METHODS

2.1 BACKGROUND

Spike detection from extracellular recordings were traditionally performed with the help of a voltage threshold [75]. A single voltage threshold was used to extract events considered as outliers in an otherwise noise dominated extracellular signal. This is primarily used for the purpose of extracting single units or single neuron activities crossing the chosen threshold closest to recording sites in an experiment. Single neuron activity usually represented with a unique action potential shape presents multiple challenges in the extraction process. The choice of the voltage threshold played an important role in detecting actual spikes as opposed to noisy background events. A very high threshold failed to detect all of the relevant spikes near recording sites and a very low threshold considered noisy data as false positive spikes. With the spikes considered as outliers and the assumption of Gaussian background noise, an optimum threshold is chosen typically to be a multiple of an estimate of the standard deviation of the noise in more recent studies [76, 77, 78]. This is used as the most common way to detect spikes as events closest to the recording sites in most studies involving a spike detection process. Representing all the detected spikes as activity from a single unit presents another major challenge. Spikes containing similar action potential shapes are considered a single unit while those with different amplitudes or superimposed spikes crossing the same threshold lead to a very inaccurate representation of a single neuron. This is also observed in the case of spikes changing the shape of their action potentials in the course of an experiment referred to as drift. These challenges are addressed with the help of a spike sorting procedure following the detection process. Features such as the peak-peak amplitude and width are extracted from the detected spikes and an unsupervised clustering procedure is performed to assign unique labels to each of the detected spikes. Spikes belonging to the same label are considered to represent the activity from a single neuron. Clustering techniques like principal

component analysis, projection on basis functions, density based clustering, wavelet analysis and template matching are used to obtain the labels. A review on all the common spike sorting techniques and the challenges presented in each of them is beyond the scope of this thesis. The reader is referred to [76, 77] for more details on spike sorting techniques.

While effective in extracting single neuron activity, using a single threshold and a subsequent spike sorting process would inaccurately represent the neural population activity. The choice of the threshold would limit the amount of spikes detected to extract population activity. Most studies using extracellular recordings design experiments short in duration and rely on static metrics to draw inferences from the data. While a fully or a semi supervised analysis pipeline was found to be well suited for such experiments, longer and more complex experiments require an unsupervised and dynamic analysis pipeline. In order to address such limitations, a new spike detection algorithm based on iterative thresholds was introduced in the thesis. The new algorithm followed by novel metrics were developed to probe into the spatial and temporal neural population dynamics. The new algorithm referred to as Competitive masking algorithm will be detailed in the following sections.

2.2 COMPETITIVE MASKING ALGORITHM FOR SPIKE DETECTION

The competitive masking algorithm was built to detect peaks in the recorded data in an iterative and unsupervised fashion. This was done with the help of a decreasing amplitude threshold followed by a competition between positive and negative polarity peaks detected at each threshold.

Data acquisition was performed with the help of the CED Spike2 software. The exact acquisition procedure and the instruments used to record extracellular data from the stellate are detailed in the methods sections of Chapters 3 and 4. A screenshot of an example Spike2 recording for a single animal is shown in fig 2.1. Channel-wise neural recordings and target recordings like LVP were manually extracted for each animal in the '.mat' format for the masking algorithm and subsequent metrics pipeline. The neural and target data extracted as a '.mat' files from the Spike2 software were read into the algorithm using the HDF5 format [79]. The HDF5 format

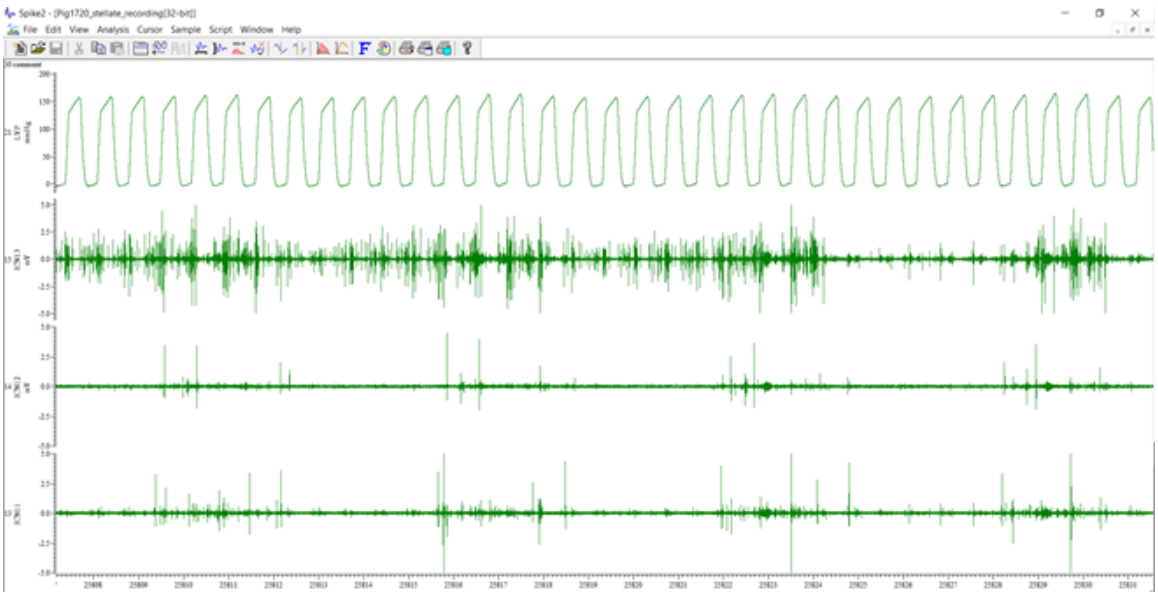

Figure 2.1: Screenshot of the Spike2 software showing three channels and LVP of one animal

is a type of hierarchical file format that aids in quick access of data that are large in size and complex in structure. More details on the HDF5 format could be found in the documentation of the corresponding python library. Once the data was available channel-wise, pre-processing was performed by normalization and smoothing. The data was first normalized to zero mean and unit variance for the purpose of clear thresholds in unsupervised detection. The smoothing process was performed with the help of a four-point Gaussian smoothing function and was repeated three times to make sure the outliers accurately represented the spikes as the algorithm progressed detection to lower levels. This was repeated for every channel of each animal as part of the unsupervised threshold based detection pipeline. The following subsections describe the different steps and functions used in the competitive masking algorithm.

2.2.1 OBTAINING LEVELS

The primary step in the algorithm involved detection of spikes or peaks in the data crossing different amplitude thresholds referred to as levels henceforth from the pre-processed data. These levels were obtained in an iterative manner until a minimum number of spikes was reached for the level or a minimum level was reached for each

channel. Events crossing a threshold will henceforth be referred to as spikes. Variables used in the algorithms will be referred to in round brackets.

The amplitude of the level to detect the locations of spikes in the data (X) was found with the help of the getNewLevel function described in algorithm 1. A New level (Level) was generated by this function by iterating over decreasing levels and stopping at a level that either contains the minimum number of spikes (MinNewSpike) or a minimum level (MinLevel). MinNewSpike and MinLevel are hyper parameters chosen qualitatively with respect to the data being analysed. The locations of the spikes crossing the new level are updated to the location containing the highest value in the 6ms window (SpikeWidth - 120) surrounding the detected spike location. Finally, the updated spike locations were stored (SpikeList) and made available for further analysis along with the level used for detection.

Algorithm 1 GetNewLevel

function GETNEWLEVEL(X, Region, Level, MinNewSpike, MinLevel)

$SpikeWidth \leftarrow 120$ ▷6 ms spike width

$SpikeList \leftarrow []$ ▷initialize list to store spike locations ▷look for new level until minimum spikes found at level or minimum level reached

while Spikes $>$ MinNewSpike $\vee$ Level $<$ MinLevel **do**

$Level \leftarrow level - DeltaLevel$ ▷reduce level by a small amount

$SpikeList \leftarrow (X > Level) \wedge (Region[X > Level] = 0)$ ▷find unmasked spikes above level

for N,L,R in [SpikeIndex, SpikeList, SpikeList + SpikeWidth] **do**

$SpikeList[N] \leftarrow argmax(X[L:R] + SpikeList[N]) \wedge \sum Region[L:R] > 1$ ▷move spike peak index to the maximum value in the 6ms window of detected unmasked spike

end for

$SpikeList \leftarrow SpikeList[Diff(SpikeList) > 100]$ ▷spikes are spaced by at least 5ms

end while

return $Level, SpikeList$

end function

2.2.2 ANALYSIS OF DETECTED SPIKES

Characteristically, since the data contained spikes of both positive and negative polarity, the function getNewlevel was used a second time on the data with the polarity reversed (-1 * data). This ensured two levels were generated containing locations of both positive and negative spikes for each of the polarities. The greater of the magnitude of the two levels (positive and negative) was chosen to proceed for further analysis on the detected spikes. The higher level and its corresponding polarity was described as "winning a competition" between positive and negative spikes for the level used in the iteration. This ensured the spikes detected in the level of the winning polarity were not doubly detected in the other polarity.

After the level were obtained, an analysis involving multiple functions was performed on the spikes detected at this stage before moving onto the next iteration of getNewlevel. This was performed by using the function AnalysisLevelGetSpike as described in algorithm 2.

Algorithm 2 AnalysisLevelGetSpike

function ANALYSISLEVELGETSPIKE(ARGUMENT LIST)

Location, *Region* ← GETSPIKELEVEL(Location, Region, SpikeIndex, Level)

↓

Region ← GETCLEANEDUP(X, Level, Region)

↓

Location, *Region*, *LocationList* ← GETRINGINGCLEANEDUP(X, Location, region, RingCutoff, RingThreshold, RingSecond, RingNumPeriod, Level, NeuralInterval)

↓

Region ← GETRIDOFISLAND(Region)

end function

Algorithm 2 made use of four separate functions on the spikes detected at the winning level. The following section expands on the algorithms for each of the functions used in the algorithm described above.

In the first step, the function getSpikeLevel described in algorithm 3 was used to assign the level of each detected spike to a list that was equal in length to the

length of the data. This collated a list for every single spike detected for current and future levels with the value of the levels at their locations in the data (Location). The function was also used to perform the important step of masking every detected spike to make them unavailable for the next iterations of getNewLevel. The mask applied was 6ms (120 - SpikeWidth) in duration around the spike and spikes masked in previous iterations were ignored as seen in algorithm 1. The masking was performed with the help of a binary variable equal in length to the data called "Region" that stored ones for the duration of the detected spikes and zeros otherwise. The updated list of spikes containing their locations, levels and the masked locations were returned for the next step.

Algorithm 3 getSpikeLevel

```
function GETSPIKELEVEL(Location, Region, SpikeIndex, Level)
    Location[SpikeIndex] ← Level
        ↪                          ▷Store Level of detected spike in the variable Location
    for EachSpike in SpikeIndex do
        Region[EachSpike − 20 : EachSpike + 100] ← 1
            ↪  ▷Mask 6ms around detected spike by setting the variable region to 1
    end for
    return Location, Region
end function
```

The returned list of masked regions was then updated by combining masked regions close to each other and masking any unmasked regions obtained from the previous function. This process was described in algorithm 4.

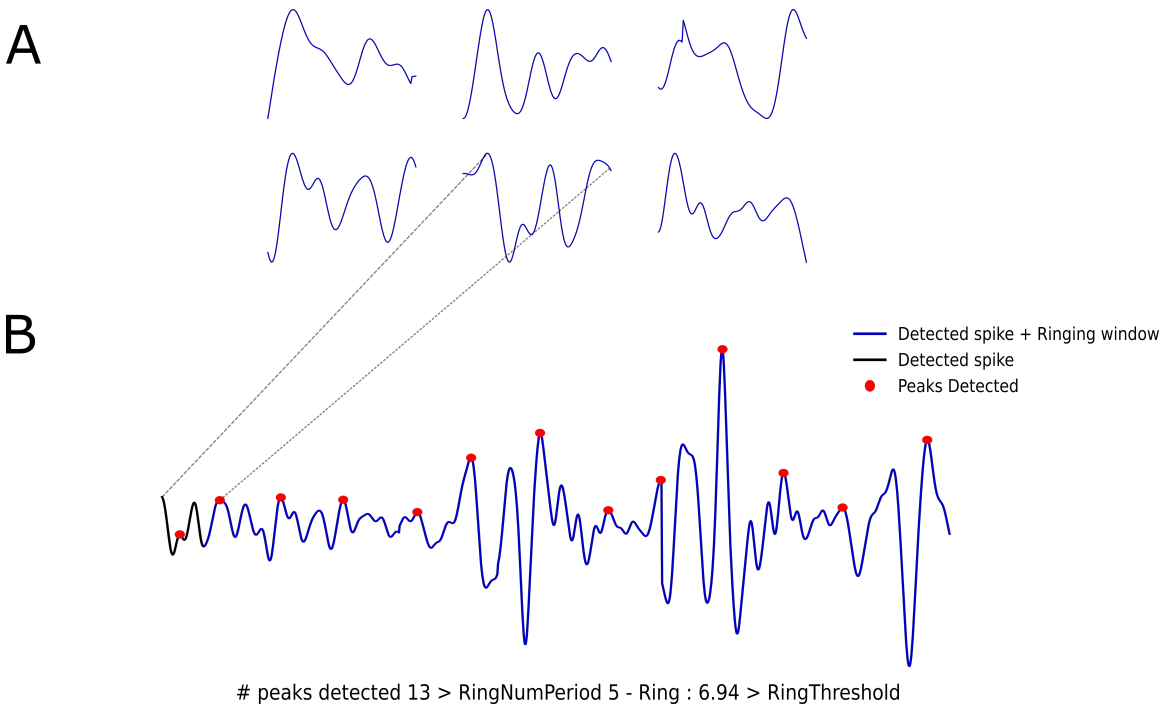

Figure 2.2: A : Six representative spikes with ringing. B : Ringing value calculated for one of the spikes expanded in duration to ringHorizon. Red dots represent the peaks detected. The number of peaks detected in the example (13) is greater than the hyperparameter RingNumPeriod and ringing metric calculated (6.94) exceeds the Ring Threshold to be rejected

Algorithm 4 getCleanedUp

function GETCLEANEDUP(X, Level, Region) ▷Identify close masked regions

$CloseSpikeList \leftarrow (Region[N : -SpikeWidth] \wedge Region[SpikeWidth :]) == 1$

for A, B in [CloseSpikeList, CloseSpikeList + 120] **do**

$Region[A : B] \leftarrow 1$ ▷Combine close masked regions

end for ▷Identify unmasked regions greater than current level

$AboveLevelList \leftarrow X > Level \wedge Region[X > Level] = 0$

for C, D in [AboveLevelList - 60, AbovelevelList + 60] **do**

$Region[C : D] \leftarrow 1$ ▷Extend mask for unmasked regions

end for

return *Region*

end function

Ringing Parameters	Description	Default
RingSecond	Duration in seconds after the detected spike to look for ringing	60ms
RingCutoff	Maximum value set for peaks to be detected in RingHorizon	0.5
RingNumPeriod	Minimum number of peak to calculate the ringing metric	5
RingThreshold	Threshold placed on the ringing metric to reject spikes with ringing	0.5

Table 2.1: Table containing the descriptions and default values of the parameters used in rejecting spikes with ringing

Once the spikes were detected and masked for a particular level, those that exhibited a ringing characteristic were removed from the list of detected spikes. A spike was considered to have ringing if it contained multiple peaks of high amplitude following the detected peak. Examples of ringing in spikes were shown in 2.2A. Each spike detected for a level was checked for ringing using the process detailed in 5. For a detected spike location (N), the spike was expanded to the duration of the ring horizon parameter (60ms default) and scaled to zero mean. The DetectPeaks function was used to find peaks or outliers in the scaled signal and all the peaks with values greater than RingCutoff (0.5 default) were set to a variable called MaxValueSet (shown as red dots in figure 2.2B). The ringing metric was calculated for those spikes that had the number of peaks detected by the function DetectPeaks (MaxValueSet) greater than RingCutoff parameter using the equation described below.

$$Ring = \frac{\sum_{i}^{NumPeaks} Peaks[i]^2}{max(Peaks)}$$

Ring = Ringing metric
Peaks = List of peak values greater than RingCutoff
NumPeaks = Number of peaks in the Peaks list
i = ith peak in the Peaks list

Spikes that exceeded the RingThreshold (0.5 default) were set to zero (rejected) in list of detected spikes and masked for the duration of the RingHorizon to make

them unavailable for the future levels. The descriptions and default values of the parameters used in the rejection of spikes with ringing is shown in table 2.1.

Algorithm 5 getRingingCleanedUp

function GETRINGINGCLEANEDUP(X, Location, region, RingCutoff, RingThreshold, RingSecond, RingNumPeriod, Level, NeuralInterval)

$RingHorizon \leftarrow RingSecond/NeuralInterval$ ▷Number of seconds after detected spike to look for ringing

$LocationList \leftarrow Location == Level$ ▷Get locations of spikes belonging to current level

for N in LocationList **do** ▷For all the spike locations

$X \leftarrow (X[N : N+RingHorizon] - Mean(X[N : N+RingHorizon]))/X[N]$ ▷Scale spike + RingHorizon

$MaxValueSet \leftarrow$ DETECTPEAKS(X) ▷Find peaks in ringing horizon

$MaxValueSet \leftarrow MaxValueSet > RingCutoff$ ▷Select peaks above RingCutOff

if Len(MaxValueSet) > RingNumPeriod **then** ▷Calculate ringing metric only if number of peaks detected > RingNumPeriod Fig2.2

$Ring \leftarrow \sum(MaxValueSet) * MaxValueSet/Len(MaxValueSet))$ ▷Ringing metric

if Ring > RingThreshold **then** ▷Criterion for rejecting and masking spikes

$Location[N : N + RingHorizon] \leftarrow 0$

$Region[N : N + RingHorizon] \leftarrow 1$

end if

end if

end for

$LocationList \leftarrow Location == Level$

for N, XPeak, L, R in [LocationList, X[LocationList], LocationList - 20, LocationList + 100] **do**

if $mean(X[L : R]) > 0.75 * Xpeak \vee Xpeak - mean(X[L : R]) < 1$ **then**

$Location[N] \leftarrow 0$ ▷Reject spikes if mean before peak is too high

end if

end for

$LocationList \leftarrow Location == Level$ ▷Update spike locations

return $Location, Region, LocationList$

end function

Algorithm 6 getRidOfIsland

function GETRIDOFISLAND(Region)

$SpikeWidth \leftarrow 120$ ▷6ms spike width

$DetectIsland \leftarrow Diff(Region)$ ▷First difference in region to isolate start and end of masked regions

$StartOf \leftarrow DetectIsland > 0$ ▷Start points of masked regions

$EndOf \leftarrow DetectIsland < 0$ ▷End points of masked regions

$WidthOfgetsEndOf - StartOf$ ▷Width of masked regions

$SmallIsland = WidthOf < SpikeWidth$ ▷Isolate small masked regions less than 6ms called small islands

$AmountToWiden = SpikeWidth - Widthof[SmallIsland]$ ▷Amount to extend small islands

if Len(SmallIsland) $>$ 0 **then**

for Start, Widen in [StartOf[SmallIsland], AmountToWiden] **do**

$Region[Start - Widen : Start] \leftarrow 1$ ▷Mask extended for extended small islands

end for

end if ▷Update masked regions after small islands are extended

$DetectIsland \leftarrow Diff(Region)$

$StartOf \leftarrow DetectIsland > 0$

$EndOf \leftarrow DetectIsland < 0$

$SpaceBetween = StartOf[1:] - EndOf[:-1]$ ▷Isolate space between masked regions

$CloseIsland = SpaceBetween < SpikeWidth$ ▷Identify spaces with width less than 6ms

if Len(CloseIsland) $>$ 0 **then**

for EndOfPrevious, StartOfNext in [EndOf[CloseIsland], StartOf[CloseIsland]] **do**

$region[EndOfPrevious : StartOfNext] = 1$ ▷Combine regions with spaces less than 6ms

end for

end if

return *Region*

end function

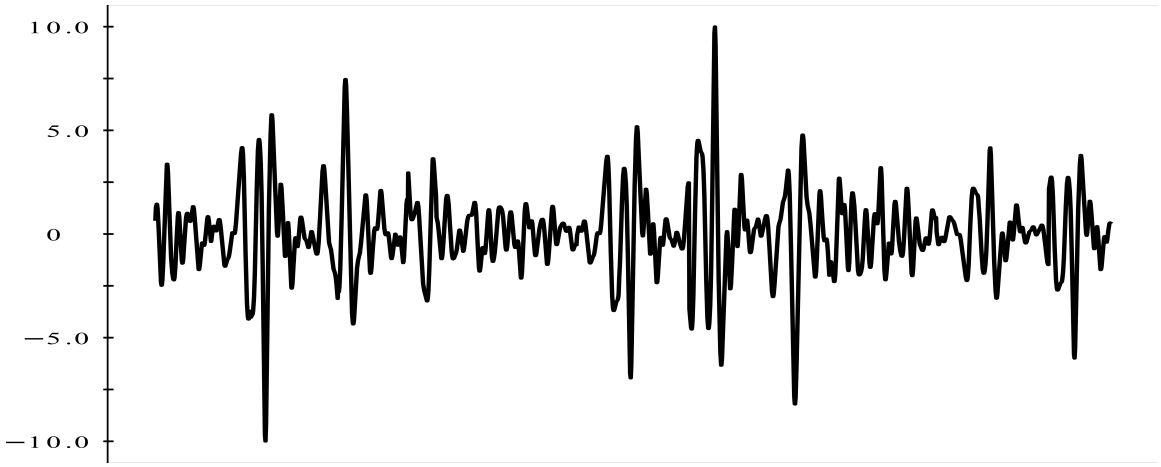

Figure 2.3: Surrogate data used in building three iterations of the MultiLevel algorithm described in algorithm 7

The final step in the analysis of spikes detected for a level was widening the width of masked spikes with duration less than 6ms (120 points). This was followed by combining masked regions separated by less than 6ms. This was performed with the help of the function getRidOfIsland described in algorithm 6.

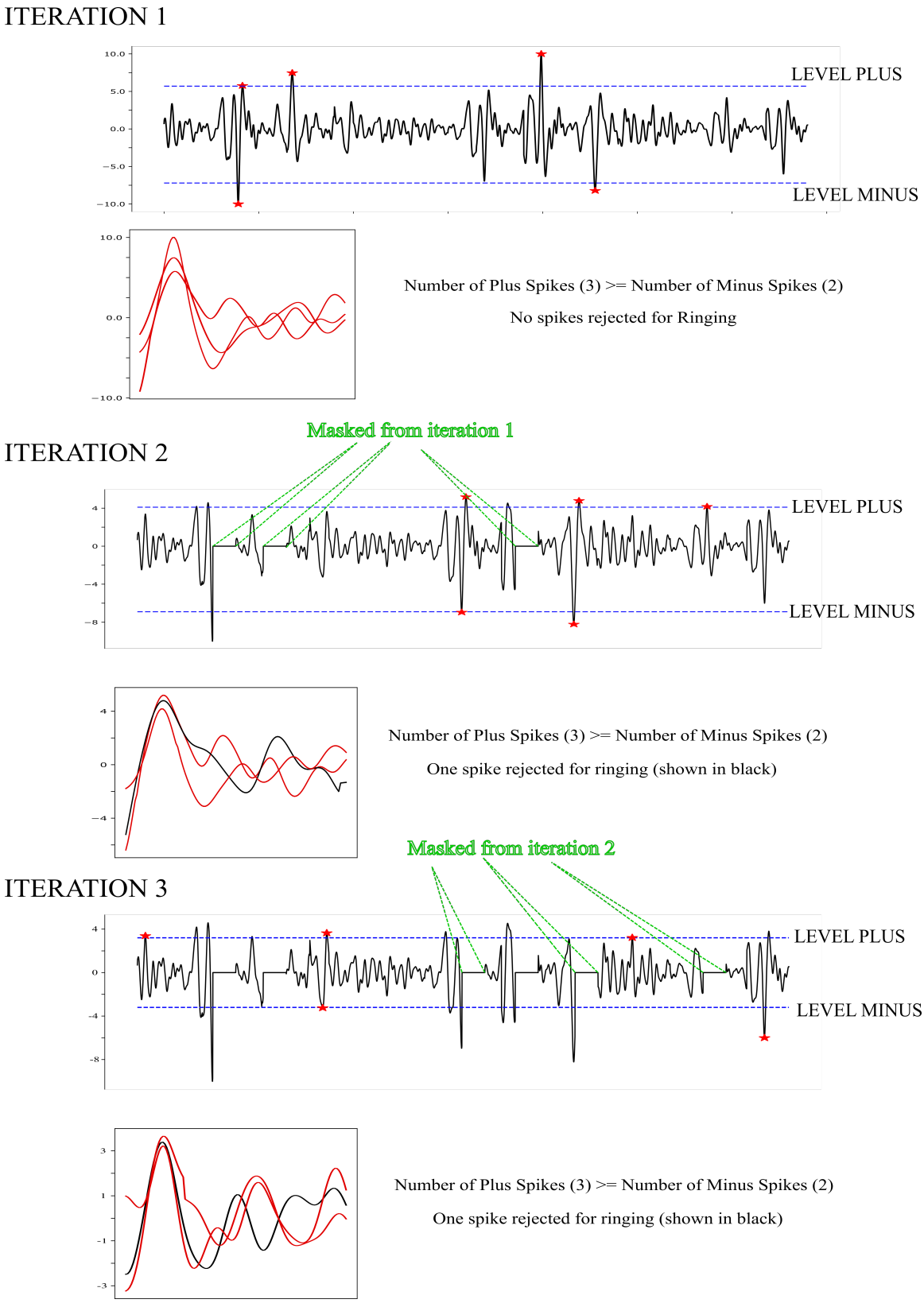

Figure 2.4: Three iterations of Multilevel for the surrogate data in fig 2.3

2.2.3 MULTILEVEL

Algorithm 7 MultiLevel - Part 1

function MULTILEVEL(ARGUMENT LIST)

$[ChannelNumber, X, NeuralStart, NeuralInterval, LVP, LVPStart,$
$\hookrightarrow$ LVPInterval, Resp, RespStart, RespInterval] $\leftarrow$ READDATA(())

$XSmooth \leftarrow GaussianFilter(X, SmoothingWidth)$ ▷Smooth the raw data with a gaussian filter

$NumberNeuralSample \leftarrow len(Xsmooth)$ ▷Number of data points in smoothed data

$Location \leftarrow zeros(NumberNeuralSample)$ ▷Initialize the location variable to zeros to store the value of the level at detected spike locations

$Region \leftarrow zeros(NumberNeuralSample)$ ▷Initialize the region variable to store "1" to mask detected spike locations for 6ms

$LevelPlus \leftarrow LevelPlusFactor * Max(Xsmooth)$ ▷Initialize the level to detect positive spikes

$LevelMinus \leftarrow LevelMinusFactor * LevelPlus$ ▷Initialize the level to detect negative spikes

$NumLevels \leftarrow 0$

▷Iterate until the minimum level parameter

while Levels available **do**

$NumLevels \leftarrow NumLevels + 1$

$[LevelPlus, ProposedPlusIndex] \leftarrow getNewLevel(ArgList,$

$SmoothingWidth,$

$XSmooth,$

$Region,$

$LevelPlus,$

$DeltaLevel,$

$MinNewSpikePlus,$

$MinLevel,$

$Left,$

$Right)$

Algorithm 8 MultiLevel - Part 2

$[LevelMinus, ProposedMinusIndex] \leftarrow getNewLevel(ArgList,$
$SmoothingWidth,$
$XSmooth,$
$Region,$
$LevelMinus,$
$DeltaLevel,$
$MinNewSpikeMinus,$
$MinLevel,$
$Left,$
$Right)$
ArgList
$= NumNeuralSample,$
$Location,$
$Region,$
$RingCutoff,$
$RingThreshold,$
$RingSecond,$
$RingNumPeriod,$
$MeanShift,$
$Left,$
$Right,$
$NeuralInterval$
if LevelPlus >= LevelMinus **then**
$PlusSpikes \leftarrow$ AnalysisLevelGetSpike(Xsmooth, levelPlus, ProposedPlusIndex, ArgList)
else
$MinusSpikes \leftarrow$ AnalysisLevelGetSpike(Xsmooth, levelMinus, ProposedMinusIndex, ArgList)
end if
end while
end function

Parameters	**Description**	**Default**
SmoothingWidth	Number of points to apply the gaussian filter to raw data	4
LevelPlusFactor	Percentage of Max value of raw data used as starting positive level	0.8
LevelMinusFactor	Percentage of LevelPlus used as starting negative level	0.9
DeltaLevel	Decrements in level for iterations of getNewLevel	0.1
MinLevel	Minimum Level to stop future iterations of getNewLevel	0.8
MinNewSpikePlus	Minimum number of positive spikes to proceed to next iteration in getNewLevel	1000
MinNewSpikePlus	Minimum number of negative spikes to proceed to next iteration in getNewLevel	500
Left	Number of points to the left of detected spikes	20
Right	Number of points to the right of detected spikes	100

Table 2.2: Table containing the descriptions and default values of the parameters used in MultiLevel

The four steps described in algorithms 3, 4, 5 and 6 that were used sequentially by the function AnalysisLevelGetSpike in algorithm 2 were used only for future winning levels. The procedure is described in algorithm 7.

The parameters and descriptions used in MultiLevel along with the default values were presented in table 2.2.

In order to further elaborate the multilevel procedure, three iterations of multilevel were described on surrogate data shown in fig 2.3. The surrogate data used to aid in explaining the novel algorithm was constructed by concatenating scaled spikes extracted from the real experimental data. Initial values for LevelPlus (8.0) and LevelMinus (7.2) were selected based on the default values for LevelPlusFactor and LevelMinusFactor in table 2.2. For the purpose of clarity, MinLevel, MinNewPlusSpike and MinNewMinusSpike were chosen at 1.0, 3.0 and 2.0 respectively. Values for DeltaLevel, Left, Right and Ringing parameters were used from defaults in tables 2.1 and 2.2. The steps of choosing the winning level for analysis and eliminating spikes with ringing were shown in three iterations in fig 2.4. Masked spikes from previous iterations were shown using green pointers for each iteration. Spikes with ringing were shown in black for the second and third iteration.

This procedure was extended to multiple channels of multiple animal data to develop an unsupervised algorithm for detecting spikes for multi channel and multi animal extracellular data. Results for each of the multi channel multi animal pipeline can be accessed with the help of the directory tree shown below.

```
/
└── Animals
    └── AnimalData
        └── Animal1
            └── MlOutput
                ├── A1Channel1
                │   ├── diaryMlA1Channel1.txt
                │   ├── metadataMutlilevelA1Channel1.txt
                │   └── outputSpikeA1Channel1.csv
                └── A1Channel2
                    └── diaryMlA1Channel2.txt
```

```
        metadataMutlilevelA1Channel2.txt
        outputSpikeA1Channel2.csv
    NeuralFiles
        A2Channel1.mat
        A2Channel2.mat
    NeuralSpecificity20s6minbuff
    TargetFiles
        A2LVP.mat
        A2Resp.mat
Animal2
    MlOutput
        A1Channel1
            diaryMlA2Channel1.txt
            metadataMutlilevelA2Channel1.txt
            outputSpikeA2Channel1.csv
        A1Channel2
            diaryMlA2Channel2.txt
            metadataMutlilevelA2Channel2.txt
            outputSpikeA2Channel2.csv
    NeuralFiles
        A2Channel1.mat
        A2Channel2.mat
    NeuralSpecificity20s6minbuff
    TargetFiles
        A2LVP.mat
        A2Resp.mat
NeuralSpecificity
```

The directory tree is shown for two animals A1 and A2 consisting of two channels each. The extracted neural recordings of all channels of each animal were stored in a directory called "NeuralFiles" in the .mat format. The first channel of the first animal was shown as A1Channel1.mat and the other channels were represented with a similar terminology. Similarly, the target data for each animal was stored in

File	Description
diaryMLAxChannely.txt	Text file containing the progress of each function called in algorithm 7 for channel y of animal x
metadataMultiLevelAxChannely.txt	Text file containing the values of the hyper parameters shown in table 2.2 for a particular run of multilevel for channel y of animal x
outputSpikeAxChannely.csv	Detected spike locations in channel y and polarity in comma separated values

Table 2.3: Table describing output files generated by algorithm 7 for channel y of animal x

"TargetFiles" (A1LVP.mat). The multilevel algorithm (algorithm 7) was run channel-wise for each animal using data stored in the structure described below. A directory called "MLOutput" was created for each channel of each animal to store the output files generated for a multilevel run. The below table contains descriptions of each output file per channel.

2.3 COFLUCTUATION AND ENTROPY METRICS

2.3.1 COACTIVITY MATRIX, COFLUCTUATION AND EVENT RATE

In order to probe the spatial coherence among neural populations recorded from different regions of the stellate, a coactivity matrix was constructed. The matrix was built to explore the relationship between spiking activities recorded from all channels of a probe used in an experiment. The figure used in Chapter 4 has been reproduced here in fig 2.5 to explain the construction of the coactivity matrix.

A representative four channels, CH1 - CH4 shown in Fig 2.5A was used to explain the construction of a 4 x 4 coactivity matrix. The population activity of each channel was represented as a time series of the mean and standard deviation estimated from rolling windows of spike rate (peaks/sec) for the duration of the channel recording. This yielded two time series' from each channel called $Spike_{rate_{mean}}$ and $Spike_{rate_{std}}$ shown on the y axis of fig 2.5A. A Pearson cross correlation was calculated for rolling windows of $Spike_{rate_{mean/std}}$ for all pairs of channels in the super diagonal of the

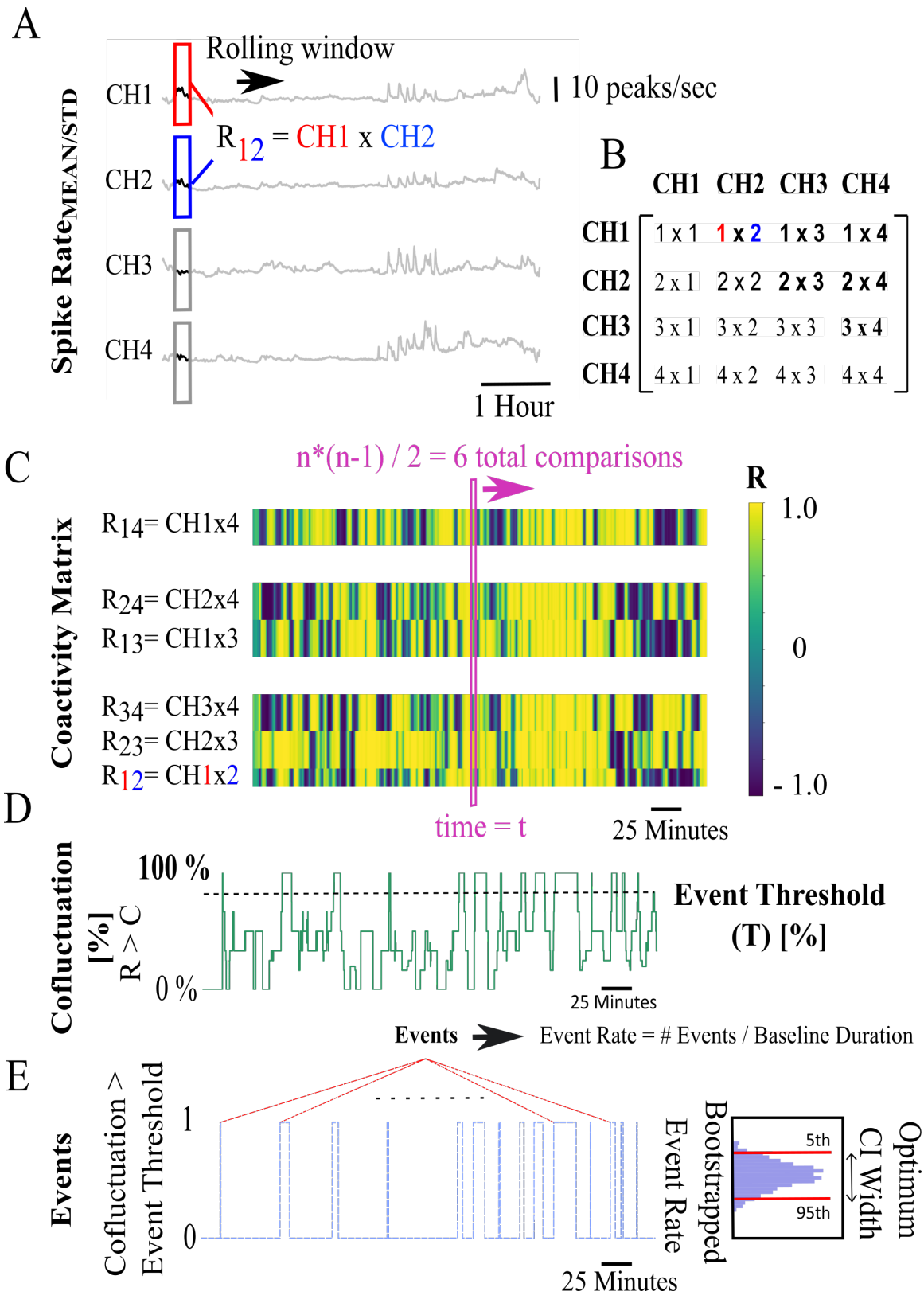

Figure 2.5: Building the coactivity matrix, cofluctuation series and event rate

channel matrix shown in bold in fig 2.5B. Two rolling windows in red and blue for CH1 and CH2 respectively are shown as an example of a single window cross correlation calculation, R_{12} for a pair of channels. The single window calculation was extended to multiple rolling windows considered as timestamps spanning the duration of the channel recordings to obtain a cross correlation time series for all possible channel pairs (R_{ij} shown in the y axis of fig 2.5C). These cross correlation time series' were arranged as rows of the coactivity matrix in increasing order of the distance between the pairs of channels. This arrangement was shown as rows in blocks separated by white spaces in fig 2.5C with each block representing adjacent channels and channels separated by 2 and 3 times the inter channel distance of 500μ m.Typically, for N channels in an experiment, a total of $\frac{N(N-1)}{2}$ cross correlation time series' are used as rows to construct the coactivity matrix. For the 16 channels used in the experiments in this work, 120 rows were used to build the coactivity matrix. A cross correlation value of 1.0 was shown in yellow and of -1.0 shown in purple.

The procedure to construct the coactivity matrix was also described in algorithm 9. The rolling mean and standard deviation of spike rate of all channels of an animal were stored as columns in a Pandas dataframe (DataFrame). The cross correlation time series for each pair of channels in the super diagonal of the channel matrix was computed using the built in correlation function of the pandas dataframe (Values).

The 16 x 16 coactivity matrix was constructed for all the six control animals and heart failure animals to check for regions of high coactivity among neural population activities of all channels. The coactivity matrix constructed for both mean and std of spiking activity for one of the control animals was shown in fig 2.6. A similar coactivity matrix was also shown for one of the heart failure animals in fig 2.7.A rolling window or a timestamp in the coactivity matrix was considered to be a region of high coactivity if a large proportion among all the channel pairs in that timestamp were found to be highly correlated. This was indicated by long columns of yellow with a representative high coactivity region shown in a black dotted box in figs 2.6 and 2.7. It was observed qualitatively that the heart failure animals contained more regions of high coactivity than the control animals.

In order to identify and quantify the number of high coactivity regions of the coactivity matrix in all animals, a cofluctuation time series, events and event rate

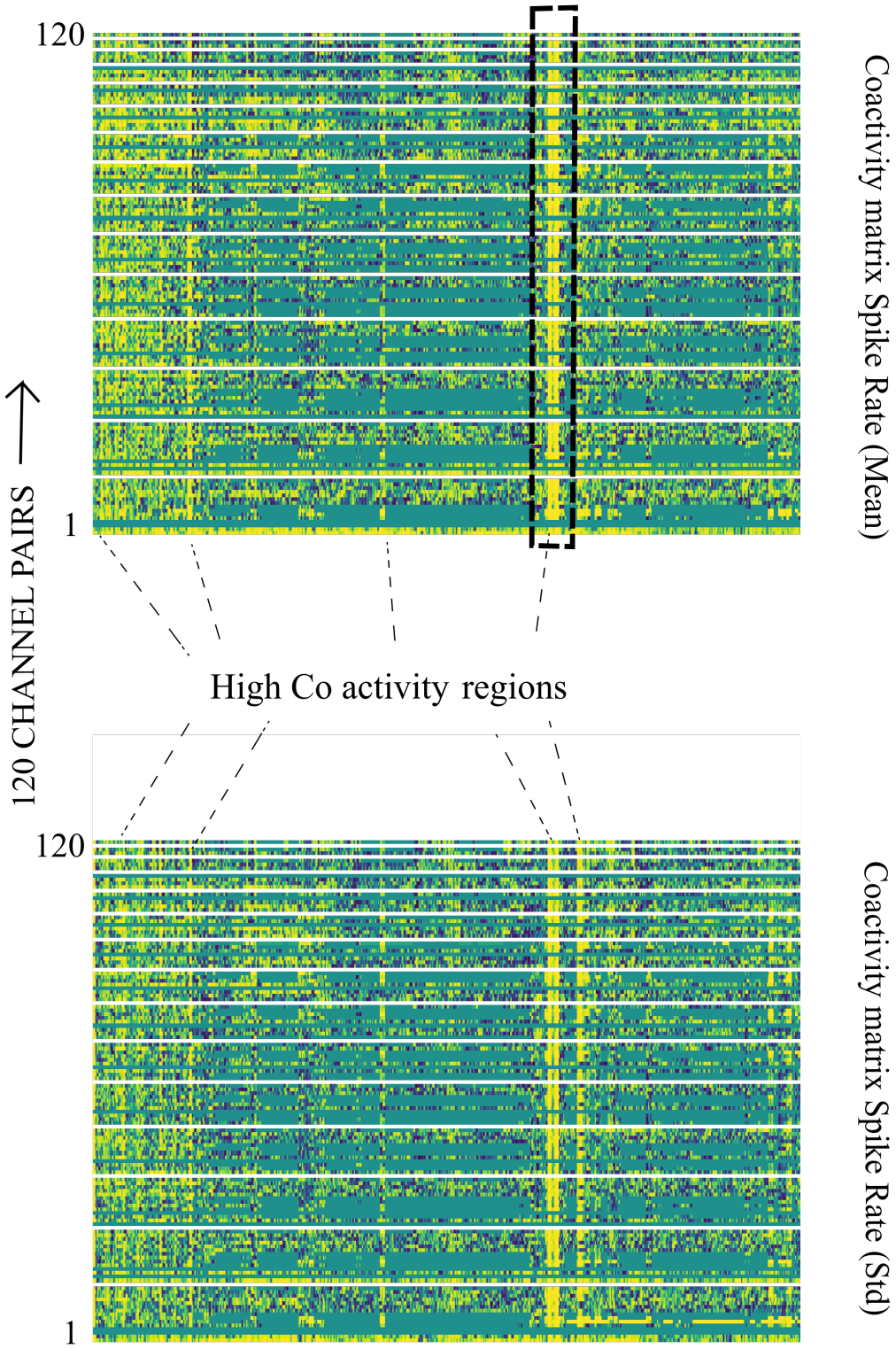

Figure 2.6: Control animal - 16 x 16 Coactivity matrix constructed for both $Spike_{rate_{mean}}$ and $Spike_{rate_{std}}$ with regions of high coactivity shown in black dotted boxes

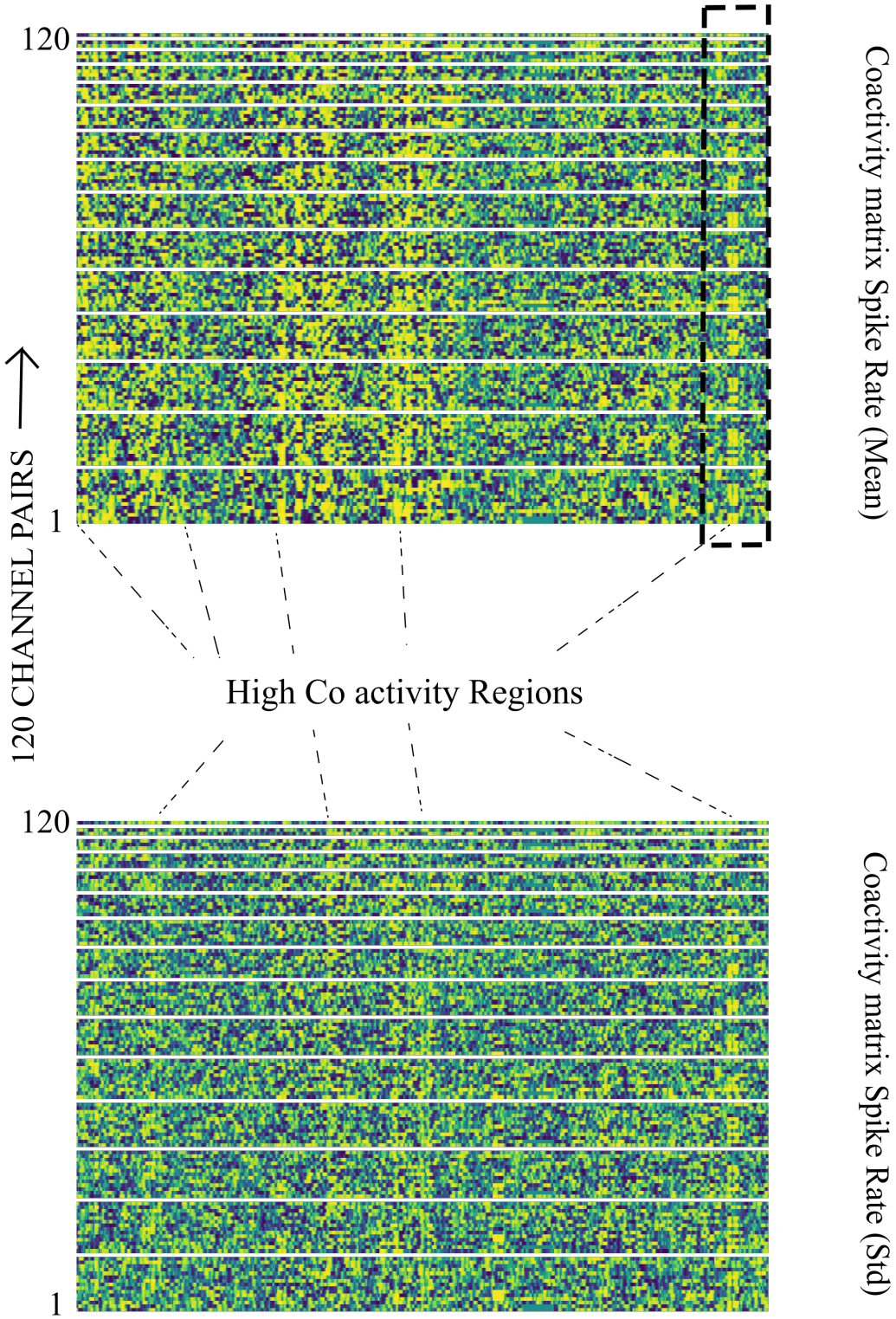

Figure 2.7: Heart Failure(HF) animal - 16 x 16 Coactivity matrix constructed for both $Spike_{rate_{mean}}$ and $Spike_{rate_{std}}$ with regions of high coactivity shown in black dotted boxes

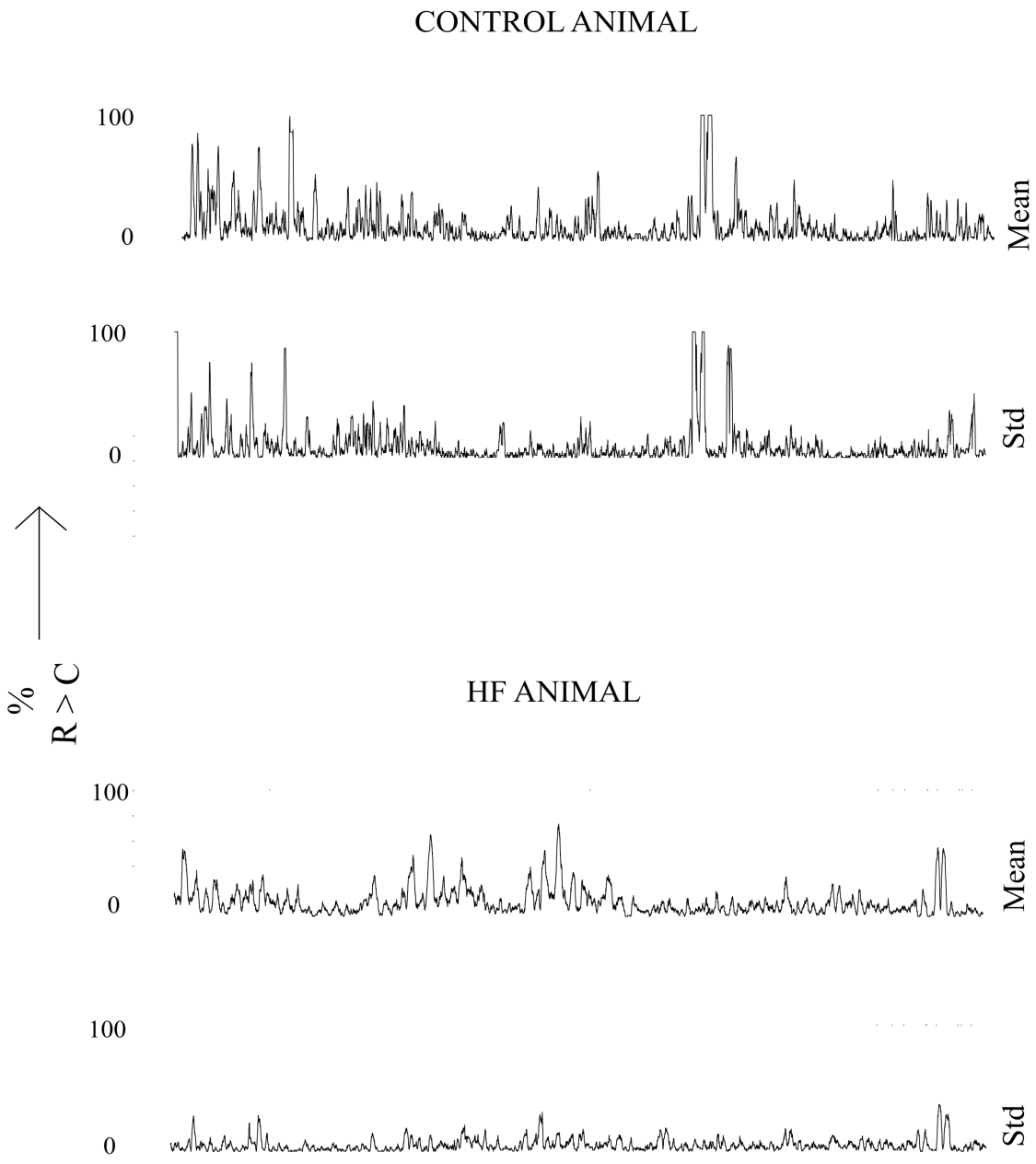

Figure 2.8: cofluctuation time series for control and HF animal shown in figs 2.6 and 2.7

Figure 2.9: Surrogate data for constructing the neural specificity metric with respect to LVP

were defined. The cofluctuation time series was defined as the percentage of channel pairs that exceeded a threshold C shown as R > C in fig2.5D. Cofluctuation series calculated for both mean and std of the control and the HF animals shown in figs 2.6 and 2.7 are shown in fig 2.8. Following the construction of cofluctuation series' for all animals, an event was defined as a timestamp of up crossing cofluctuation through another threshold called the event threshold shown as T in fig 2.5D and E. These events represent timestamps in an experiment with high spatial coherence among neural populations from different regions of the stellate. In order to compare the number of events between different groups of animals, an event rate (ER) for the cofluctuation series of mean and std was defined with respect to the duration of the experiment as seen below.

$$ER_{mean/std} = \frac{Number\ of\ Events}{Duration\ of\ experiment}$$

Characteristics of the cofluctuation series and a hypothesis based on number of events between animal groups is elaborated in Chapter 5 as part of the paper titled "Metrics of High Cofluctuation and Entropy to Describe Control of Cardiac Function in the Stellate Ganglion" by Gurel & Sudarshan et al.

2.3.2 NEURAL SPECIFICITY

The neural specificity metric was constructed in order to probe into the bias of neural populations towards a particular phase or value of a target signal for the duration of an experiment. LVP and respiratory pressure are two examples of such target signals

Algorithm 9 Coactivity Part 1

$NumChan = rows(ChNumbers)$

$CoactivityVals \leftarrow []$ ▷Initialize empty list to store coactivity between channels

for SuperDiagonal in Range(NumChan) **do**

for Index in Range(NumChan - SuperDiagonal) **do**

$PhysName0 \leftarrow ChNumbers[Index]$

$\hookrightarrow$ ▷First Channel in pair

$PhysName1 = ChNumbers[Index + SuperDiagonal]$

$\hookrightarrow$ ▷Second channel in pair

▷Names of channels as header in data frames to access their spike rates

$Name0 = "XIcn" + str(PhysName0)$

$Name1 = "XIcn" + str(PhysName1)$

for Name0 in Cols(DataFrame) and Name1 in Cols(DataFrame) **do**

$Values \leftarrow$

$\hookrightarrow$

$RollingWindows(Correlate(DataFrame[Name0], DataFrame[Name1]), Window)]$

▷Correlate pairs of channels in superdiagonal in rolling windows

$CoactivityVals.append(values)$ ▷Store rolling window correlated series of channel pair in a separate list

end for

$Rows \leftarrow rows(transpose((CoactivityVals)))$ ▷Number of rows in transpose of CoactivityVals

$CoactivityStats \leftarrow zeros(Rows)$ ▷Initialize empty list to store Coactivity stats

▷Looping through all the channel pairs

for Row in Range(Rows) **do**

$Ind \leftarrow NonZeros(CoactivityVals[row])$ ▷Isolate indices of non zero rolling windows channel correlation pairs

$FilterRow \leftarrow CoactivityVals[Row][Ind]$ ▷Non zero rolling windows

Algorithm 10 Coactivity - Part 2

$CoactivityStats[Row] \leftarrow len(NonZeros(Abs(FilterRow) > CorrThreshold))$
▷Store the number of Channel pairs that exceed the CorrThreshold parameter for a rolling window as a series
$CoactivityStats[Row] \leftarrow CoactivityStats[Row] * 100.0/len(FilterRow)$
▷Percentage of number of channel pairs exceeding the CorrThreshold parameter as a series
end for
end for
end for
$StateArray \leftarrow zeros(len(CoactivityStats))$ ▷Initialize empty list to store State changes in CoactivityStats
for i in range(len(CoactivityStats)) **do**
if CoactivityStats[i] > StateThreshold **then**
$StateArray[i] \leftarrow 1$ ▷A "1" is stored where percentage of channel pairs ↪ exceeds the StateThreshold parameter
end if
end for
$TransitionTimestamp \leftarrow []$ ▷Initialize an empty list to store State Transition indices
for i in Range(len(StateArray) - 1) **do**
if StateArray[i] - StateArray[i + 1] == -1 **then**
$TransitionTimestamp \leftarrow append([i + 1])$ ▷Store the indices where StateArray moves from 0 to 1 to indicate an event
end if
end for
$EventRate \leftarrow len(TransitionTimestamp)/ExptTime$ ▷Calculate event rate for the Coactivity matrix

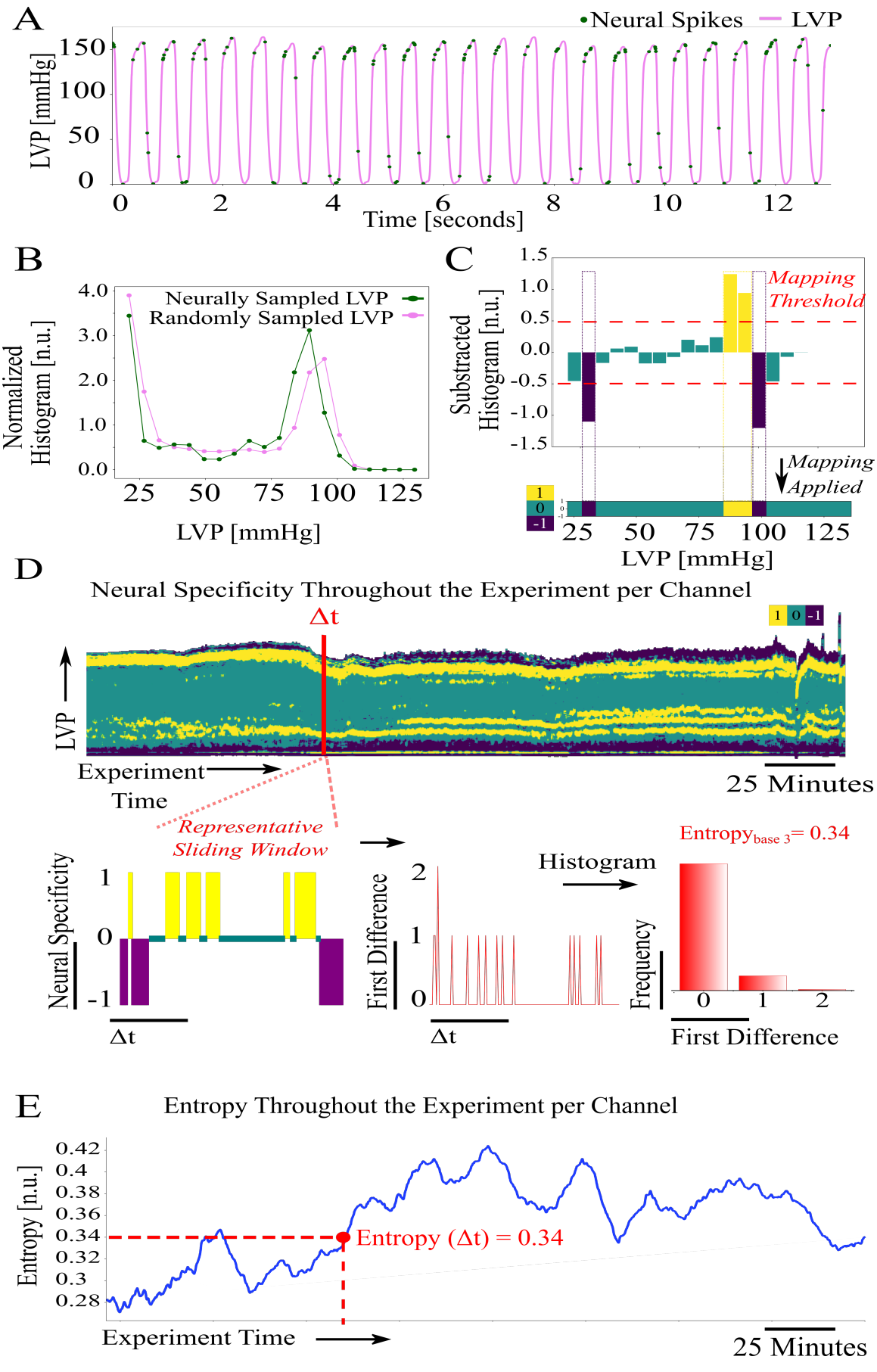
A
Neural Spikes
LVP
LVP [mmHg]
150
100
50
0
0
2
4
6
8
10
12
Time [seconds]
B
Normalized Histogram [n.u.]
Neurally Sampled LVP
Randomly Sampled LVP
4.0
3.0
2.0
1.0
0.0
25
50
75
100
125
LVP [mmHg]
C
Substracted Histogram [n.u.]
1.5
1.0
0.5
0.0
-0.5
-1.0
-1.5
Mapping Threshold
Mapping Applied
1
0
-1
25
50
75
100
125
LVP [mmHg]
D
Neural Specificity Throughout the Experiment per Channel
Δt
1 0 -1
LVP
Experiment Time
25 Minutes
Representative Sliding Window
Neural Specificity
1
0
-1
Δt
First Difference
2
1
0
Δt
Histogram
Frequency
Entropy$_{base\ 3}$= 0.34
0
1
2
First Difference
E
Entropy Throughout the Experiment per Channel
Entropy [n.u.]
0.42
0.4
0.38
0.36
0.34
0.32
0.3
0.28
Entropy (Δt) = 0.34
Experiment Time
25 Minutes

used in the thesis. The metric was constructed by subtracting a normalized histogram of the target signal computed at random spike times from that of the target computed at actual spike times in moving windows for the course of the experiment. The width of the moving windows was chosen to contain sufficient target data for computing the normalized histograms. In the case of the neural specificity metric for LVP , the moving window width was chosen to contain many cycles of LVP.

The procedure used in constructing the metric for any target was elaborated in algorithm 11. Information from the output of Multilevel (algorithm 7) such as spike time (SpikeTime), target value computed at spike times (Tar) and list of channels (ChannelList) were used to represent population activity. The target information was primarily represented using the raw target signal (TarRaw). Spikes detected at the same time across a fixed number of channels in an animal were considered as artifact and an artifact removal operation was performed. This artifact removal was performed with the number of channels set as a hyper parameter (NumArtCompare). Since the spike detection process extracted spikes up to the minimum level hyper parameter in Multilevel, those detected at the lowest levels might represent the putative noise floor falsely being considered as spikes. In order to avoid this problem, another level threshold was qualitatively chosen to accurately represent population activity. Positive and negative spikes above this level (LevelPlus and LevelMinus) were used to represent population activity for further steps in the construction of the metric. A list of all the parameters and descriptions used in the construction of the metric was detailed in table 2.4. This was followed by creating moving windows for the duration of the experiment with the width chosen as a hyper parameter. The window width was chosen qualitatively at 10 minutes for experiments conducted for 6-8 hours to include sufficient target and spike data. For each of the moving windows, two normalized histograms were computed as described below,

- A normalized histogram for the k_{th} bin of the target T_j at a randomized spike time t_j over M bins referred to as randomly sampled target was defined as,

$$H(T_j)_k = \frac{h(T_j)_k}{\sum_{k=1}^{k=M} h(T_j)_k}$$

- Another normalized histogram for the k_{th} bin of the target ST_j computed at an actual spike time t_j over M bins referred to as neurally sampled target was

Algorithm 11 NeuralSpecificityMetric Part 1

$TarRaw, TarStart, TarInterval \leftarrow readTarget()$

$ChannelList, DataChannel, SpikeTime, Tar \leftarrow readMultilevel2Spike()$

$Index \leftarrow RemoveArtifact(NumArtCompare, ChannelList, DataChannel,$
$\hookrightarrow$
$SpikeTime)$ ▷remove artifact

$SpikeTime, SpikeLevel, DataChannel, Tar \leftarrow SpikeTime[Index],$
$\hookrightarrow$
$SpikeLevel[Index], DataChannel[Index], Tar[Index]$ ▷extract spike data after artifact removal

$BinWidth \leftarrow 0.0025$ ▷isolate positive and negative spikes

$PlusSpikes \leftarrow SpikeLevel[SpikeLevel>0]$

$MinusSpikes \leftarrow SpikeLevel[SpikeLevel<0]$

$BinEdges \leftarrow linspace(0, 5, 5/BinWidth)$

▷isolate spikes based on predetermined levels

$Index \leftarrow (SpikeLevel>LevelPlus) \vee (SpikeLevel<-LevelMinus)$

$SpikeTime, SpikeLevel, DataChannel, Tar \leftarrow$
$\hookrightarrow$
$SpikeTime[Index], SpikeLevel[Index], DataChannel[Index], Tar[Index]$

$SpikeTimes \leftarrow SpikeTime + Window$ ▷create sliding windows based on a window width

for Spike in SpikeTimes **do**

$EndIndex[N] \leftarrow argmax(SpikeTime > Spike)$

$N \leftarrow N + 1$

end for

$StartIndex \leftarrow 1 : len(EndIndex)$

$Specificity \leftarrow Zeros[len(StartIndex), NumBin]$ ▷Initialize neural specificity metric matrix for storing the histograms of target computed at spike times

Algorithm 12 NeuralSpecificityMetric Part 2

$SpecificityNotSet \leftarrow Zeros(len(StartIndex))$ ▷Track neural specificity bins

for (Start, End) in (StartIndex, EndIndex) **do**

$Specificity[Start, :] \leftarrow histogram(tar[Start : End], NumBin)$ ▷Histogram of the target at spike times

$Specificity[Start, :] \leftarrow SavGolFilter(Specificity[Start, :])$ ↪ ▷Smoothed Histogram using the Savistky-Golay filter

$SpecificityNotSet[Start] \leftarrow 1$ ▷moving window histogram calculated

end for

$RawStartIndex \leftarrow (SpikeTime[StartIndex] - TarStart)/TarInterval$ ▷Start times of moving windows for raw target

$RawEndIndex \leftarrow RawStartIndex + (Window/TarInterval)$ ▷End times of moving windows for raw target

$SpecificityRandom \leftarrow Zeros[len(StartIndex), NumBin]$ ▷Initialize neural specificity metric matrix for storing the histograms of target computed at random spike times

$SpecificityRandomNotSet \leftarrow Zeros(len(StartIndex))$ ▷Track random neural specificity bins

for [I, Start, End, TarStart, TarEnd] in ↪ [(1 : len(StartIndex)), StartIndex, EndIndex, RawStartIndex, RawEndIndex] **do**

$SpecificityRandom[Start, :] \leftarrow histogram(TarRaw(random([TarStart : TarEnd])), NumBin)$ ↪ ▷Histogram of the target at random spike times

$SpecificityRandomNotSet[Start] \leftarrow 1$ ▷moving window histogram calculated

end for

$Specificity \leftarrow Specificity - SpecificityRandom$ ▷Subtract to obtain neural specificity metric

$Specificity \leftarrow Specificity/std(Specificity)$

Algorithm 13 NeuralSpecificityMetric Part 3

▷Apply hard threshold to the metric

$Specificity > HardThreshold \leftarrow 1$

$Specificity < HardThreshold \leftarrow 0$

$Specificity < -HardThreshold \leftarrow -1$

▷Entropy computation

$NumWindows \leftarrow len(StartIndex)$

$ShannonEntropy \leftarrow Ones(NumWindows)$

for Row in range(len(StartIndex)) **do**

$Diff = Diff(Row)$

$P = histogram(Diff, 3)$

$ShannonEntropy[Row] \leftarrow entropy(p, base = 3)$

end for

$PlotResults(Specificity, SpecificityRandom, HardThreshold)$

defined as

$$H(ST_j)_k = \frac{h(ST_j)_k}{\sum_{k=1}^{k=M} h(ST_j)_k}$$

A small segment of LVP shown in blue tracings in fig 2.10 A was used to graphically describe the steps in the construction of the metric. The two normalized histograms described above were shown in fig 2.10 B for a single moving window.

The neural specificity A_{jk} for the k_{th} bin was obtained by performing a bin-wise subtraction of the two histograms described above.

$$A_{jk} = H(T_j)_k - H(ST_j)_k$$

This operation was shown for a single moving window in fig 2.10 C. The subtracted histogram was color coded to clearly represent the neural population bias. The color codes for the k_{th} bin were chosen as,

- yellow for $A_{jk} = 1$ to represent a higher bias to the target bin compared to random target sampling.
- purple for $A_{jk} = -1$ to represent a lower bias to the target bin compared to random target sampling.

Parameters	Description	Default
LevelPlus	Minimum level used for the choice of detected positive spikes	1.5
LevelMinus	Minimum level used for the choice of detected negative spikes	1.5
HardThreshold	Threshold used to color code each of the normalized histograms of the metric	0.5
Window	Duration of the moving windows in seconds	20
NumArtCompare	Number of channel to look for artifact	5

Table 2.4: Table containing the descriptions and default values of the parameters used in Neural Specificity

- teal for $A_{jk} = 0$ to represent no change in bias to the target bin compared to random target sampling.

This color code was also shown in fig 2.10 C. The above steps were repeated for multiple moving windows spanning the course of the experiment to build the neural specificity metric for a specific target. For the case of LVP, the metric was shown for a single channel in fig 2.10 D.

In order to extract information from the metric, Shannon entropy was calculated for each of the moving windows. A first difference in neural specificity, ΔA_{t_j} for a time window t_j, was calculated prior to the entropy calculation (first difference in fig 2.10 C). Change in neural specificity takes on values 0, 1 and 2 to represent the magnitude of changes in neural specificity. The entropy was calculated as,

$$E = \sum_{\Delta A_{t_j}=0}^{\Delta A_{t_j}=2} p(\Delta A_{t_j}) log_3(p(\Delta A_{t_j}))$$

A uni variate time series was obtained by repeating the entropy calculation for all of the moving windows as shown in 2.10 E. Mean and standard deviation of the entropy time series was used to develop and test hypotheses between different animal groups further elaborated in Chapter 5 as part of the paper titled "Metrics of High Cofluctuation and Entropy to Describe Control of Cardiac Function in the Stellate Ganglion" by Gurel et al.

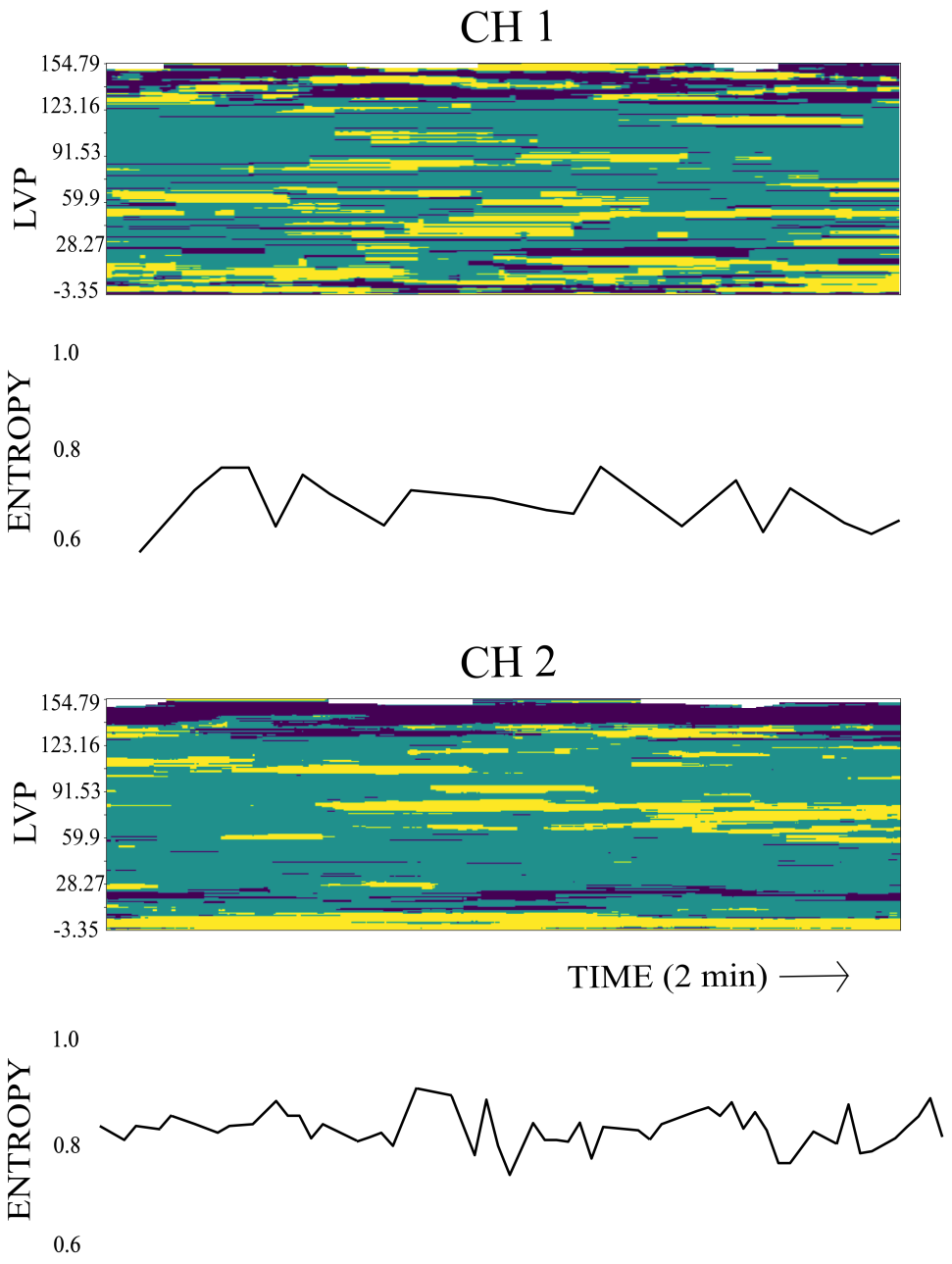

Figure 2.11: LVP - neural specificity metric for 2 mins and entropy shown for two channels of one animal

File	Description
diaryAxChannely.txt	Text file to track the progress of algorithm 11 for channel y of animal x
metadataNeuralSpecificityAxChannely.txt	Text file containing the values of the hyper parameters shown in table ? for a particular run of neural specificity for channel y of animal x
NeuralSpecificityMetricLVP,pdf	Plot of LVP-neural specificity for channel y
ShannonEntropy.csv	Shannon entropy time series computed from the metric for channel y stored as comma separated values

Table 2.5: Table describing output files generated by algorithm 11 for channel y of animal x

The directory structure for an example two channel two animal surrogate data can be found in the repository : GitHub Repo Link

```
/
└── Animals
    └── AnimalData
        └── Animal1
            ├── MlOutput
            ├── NeuralFiles
            ├── NeuralSpecificity20s6minbuff
            │   ├── A1Channel1
            │   │   ├── ShannonEntropy.csv
            │   │   ├── diaryA1Channel1.txt
            │   │   ├── imageA1Channel1NeuralSpecificityMetricLVP.pdf
            │   │   └── metadataNeuralSpecificityA1Channel1.txt
            │   └── A1Channel2
            │       ├── ShannonEntropy.csv
            │       ├── diaryA1Channel2.txt
            │       ├── imageA1Channel2NeuralSpecificityMetricLVP.pdf
            │       └── metadataNeuralSpecificityA1Channel2.txt
            └── TargetFiles
```

The same two channel two animal directory structure was used to describe the output files generated for a multi channel neural specificity metric case. The output files and the metric figures were stored channel-wise in a directory called "NeuralSpecificity" that was created for each animal. The neural specificity algorithm (algorithm 11) was run sequentially for all channels of an animal and the output files were stored in individualized channel directories. These channel directories, shown as A1Channel1 and A1Channel2 for animal 1 for instance, stored four files to represent the output files detailed in table 2.5. The neural specificity metric plots and the corresponding entropy plots was also shown for the two channels of one animal in fig 2.11.

Characteristics of the neural specificity metric and a hypothesis based on entropy calculated from the metric between animal groups are elaborated in Chapters 4 as part of the paper titled "A novel metric linking stellate ganglion neuronal physiology to cardiopulmonary dynamics" by Sudarshan et al and 5 as part of the paper titled

"Metrics of High Cofluctuation and Entropy to Describe Control of Cardiac Function in the Stellate Ganglion" by Gurel & Sudarshan et al.

Chapter 3

ANALYSIS OF STELLATE GANGLION POPULATIONS IN HEALTHY ANIMALS

Contribution of the student :

The candidate was a primary contributor to the competitive masking algorithm, neural specificity metric, data analysis, interpretation of experimental results, figure preparation, drafting, editing and manuscript revision.

AMERICAN JOURNAL OF PHYSIOLOGY
HEART AND CIRCULATORY PHYSIOLOGY

Am J Physiol Heart Circ Physiol 321: H369–H381, 2021.
First published July 2, 2021; doi:10.1152/ajpheart.00138.2021

INNOVATIVE METHODOLOGY

Integrative Cardiovascular Physiology and Pathophysiology

A novel metric linking stellate ganglion neuronal population dynamics to cardiopulmonary physiology

Koustubh B. Sudarshan,[1] Yuichi Hori,[2] M. Amer Swid,[2] Alexander C. Karavos,[1] Christian Wooten,[2] J. Andrew Armour,[2] Guy Kember,[1] and Olujimi A. Ajijola[2,3]

[1]*Department of Engineering Mathematics and Internetworking, Dalhousie University, Halifax, Nova Scotia, Canada;* [2]*Cardiac Arrhythmia Center and Neurocardiology Research Program, University of California, Los Angeles, California; and* [3]*Molecular, Cellular, and Integrative Physiology Interdepartmental Program, University of California, Los Angeles, California*

Abstract

Cardiopulmonary sympathetic control is exerted via stellate ganglia (SG); however, little is known about how neuronal firing patterns in the stellate ganglion relate to dynamic physiological function in the heart and lungs. We performed continuous extracellular recordings from SG neurons using multielectrode arrays in chloralose-anesthetized pigs (n = 6) for 8–9 h. Respiratory and left ventricular pressures (RP and LVP, respectively) and the electrocardiogram (ECG) were recorded concomitantly. Linkages between sampled spikes and LVP or RP were determined using a novel metric to evaluate specificity in neural activity for phases of the cardiac and pulmonary cycles during resting conditions and under various cardiopulmonary stressors. Firing frequency (mean 4.6 ± 1.2 Hz) varied spatially across the stellate ganglion, suggesting regional processing. The firing pattern of most neurons was synchronized with both cardiac (LVP) and pulmonary (RP) activity indicative of cardiopulmonary integration. Using the novel metric to determine cardiac phase specificity of neuronal activity, we found that spike density was highest during diastole and near-peak systole. This specificity was independent of the actual LVP or population firing frequency as revealed by perturbations to the LVP. The observed specificity was weaker for RP. Stellate ganglion neuronal populations exhibit cardiopulmonary integration and profound specificity toward the near-peak systolic phase of the cardiac cycle. This novel approach provides practically deployable tools to probe stellate ganglion function and its relationship to cardiopulmonary pathophysiology.

NEW & NOTEWORTHY Activity of stellate ganglion neurons is often linking indirectly to cardiac function. Using novel approaches coupled with extended period of recordings in large animals, we link neuronal population dynamics to mechanical events occurring at near-peak systole. This metric can be deployed to probe stellate ganglion neuronal control of cardiopulmonary function in normal and disease states.

cardiopulmonary; hemodynamics; neural recordings; spike activity; stellate ganglion

INTRODUCTION

Populations of neurons within stellate ganglia (SG) are involved in closed loop hierarchical control of cardiac function (1). Existing studies show that the SG integrates afferent input from multiple sites and processes them via local circuit neurons (2–4). Cardiomotor responses resulting from SG processing are mediated via postganglionic neurons that project to the heart (5).

Structural and neurochemical remodeling of SG neurons have been observed in pathological states, and are accepted to have a major impact on cardiac function in animals (6–8) and in humans (9, 10). Interventions targeting the stellate ganglion are used to treat various cardiovascular diseases including cardiac arrhythmias (11–13). However, network processing in normal states within SGs is not understood. Furthermore, the mechanisms through which cardiac disease alters SG network or processing function remains unknown. Knowledge of these processes is needed to fundamentally understand the onset and evolution of pathology, mediated by the SG, for therapeutic purposes.

Prior in vivo extracellular recording studies of SG neuronal function have been limited by relatively low spike detection and associated spike counts, such that spike sorting of specific neurons has been limited to episodic recordings (3, 14–17). Such features lack the space and time resolution required to examine SG-networked processing of neural populations within intrathoracic extracardiac sympathetic ganglia that coordinate cardio-respiratory function.

Correspondence: O. A. Ajijola (oajijola@mednet.ucla.edu).
Submitted 17 March 2021 / Revised 23 June 2021 / Accepted 23 June 2021

The purpose of this study is to explore neural processing of cardiopulmonary transduction by SG neuronal populations during baseline states and in response to specific cardiovascular and pulmonary stressors. To accomplish this, we performed continuous recordings of the activity generated by populations of SG neurons for several hours, with ongoing cardiopulmonary dynamics. To gain sufficient resolution of neural population activity to evaluate any specificity in firing patterns, we coupled prolonged recording periods (8–9 h/animal subject) with a spike detection approach to detect neural activity close to the noise threshold. The evolution of specificity in neural population activity relative to unbiased random sampling exposed dynamic features of network processing of physiological function such as cardiac and pulmonary variables over multiple time scales.

METHODS

Animal Model and Protocols

This study was approved by the University of California, Los Angeles (UCLA) Animal Research Committee. Male Yorkshire pigs (n = 6) weighing 43.8 ± 4.2 kg were studied. Studies were performed consistent with the UCLA Institutional Animal Care and Use Committee (IACUC) guidelines and the National Institutes of Health's *Guide for the Care and Use of Laboratory Animals*. Each porcine subject was sedated with terconazole (4–8 mg/kg im), intubated, and maintained under general anesthesia with inhaled isoflurane (2%). After median sternotomy, animals were transitioned to chloralose anesthesia with supplemental oxygen (2 L/min) during the experimental study. Surface electrocardiogram (ECG) and hemodynamic measures were continuously monitored.

Experimental Studies

Sedation and intubation were performed as described previously (17). Arterial blood pressure was monitored continuously from the left femoral artery using a pressure catheter (SPR350, Millar Inc., Houston, TX). ECGs were also continuously recorded during the experimental protocol, and arterial blood gas was evaluated hourly. Fentanyl citrate (20 μg/kg) was administered intravenously before sternotomy. The pericardium was opened to expose the heart and both stellate ganglia. Following completion of surgical procedures, isoflurane was gradually tapered off and switched to α-chloralose (6.25 mg/125 mL; 1 mL/kg for bolus, 20–35 mL/kg or titrated to effect for maintenance) for in vivo neural recordings from the left stellate ganglion. The left carotid artery was exposed, and a pressure catheter (SPR350, Millar Inc., Houston, TX) was inserted to continuously monitor left ventricular pressure. Animal subjects were kept covered and heated using water blankets (37°C–38°C), and a saline drip (8–10 mL/kg/h) was continuously given intravenously. Arterial blood gas was sampled hourly or more frequently (RoVent Jr., Kent Scientific Corporation, Torrington, CT) during respiratory stressors such as apnea. At the end of the study, subjects were euthanized under deep sedation of isoflurane and cardiac fibrillation was induced.

Extracellular Stellate Ganglion Neuronal Recordings

A linear microelectrode array (LMA, 16 channels, Microprobes, Gaithersburg, MD) was inserted into the craniomedial pole of the left stellate ganglion. The platinum-iridium electrodes consisted of 25-μm surface area, 500-μm interelectrode spacing, and 0.2–0.5-MΩ impedance. A microelectrode amplifier (Model 3600, A-M Systems, Inc., Carlsborg, WA) was used to acquire amplified signals. These electrode characteristics enable recordings of soma action potentials, not axons of passage in the stellate ganglion. Neuronal recording signals were filtered at 300 Hz to 3 kHz, with a gain of 1,000–2,500 and transferred into a data acquisition platform (Power1401, Cambridge Electronic Design, Cambridge, UK) and recorded using Spike2 software (Cambridge Electronic Design).

Spike Detection

A schematic summary for spike detection is shown in Supplemental Fig. S1; all Supplemental material is available at https://doi.org/10.6084/m9.figshare.14347061.v2. Surrogate neural data are normalized to zero mean and unit variance. The competition algorithm is initialized by placing plus/minus barriers and then scanning for crossings above the plus barrier and below the minus barrier. The plus/minus barrier levels are brought closer to zero until a minimal number of crossings occur. Plus or minus spikes "win" upon: *1*) first reaching a minimal number of crossings, or *2*) both sides reaching the minimal number and the side with most crossings wins. The regions at, and beyond, the plus/minus barriers ±9 are highlighted in gray. We refer to the gray regions, at and beyond the barriers, as "barriers" for simplicity in what remains. All spike peaks beyond the barriers are annotated with green (plus) and red (minus) stars. Below the figure containing surrogate data, the plus spikes (*below left*) and minus spikes (*below right*) that were found are shown.

Two plus spikes are found along with one minus spike in the first iteration (*Iter 1*). Given a minimum of two spikes required, plus meets the criterion and wins the first iteration and, therefore, the plus spikes are retained. After winning the first iteration, all neural activity associated with plus spikes from *Iter 1* are masked (black bar with zero signal). The barriers are further reduced, and the search region is noted as a darker gray bar. The algorithm is iterated and plus and minus peaks are found. Note that the minus spike found earlier in *Iter 1* is found again and the minus count has a competitive advantage in this iteration. In *Iter 2*, there are more minus than plus spikes with minus satisfying the criterion of at least two spikes and minus wins the second iteration. The competition algorithm is repeated and shown for a third iteration. Note that previous iteration plus spikes have been subsumed into the minus population. The algorithm is continued until the barrier passes a minimum level for plus and minus.

Stressors

After the experimental preparation described above, a 20-min waiting period was allowed for stabilization. Various stressors [inferior vena cava (IVC) occlusion, aortic occlusion, and right ventricular endocardial pacing] were performed in a random order. Decremental right ventricular pacing (RVP) was performed with a cycle length (CL) of 450 ms (133 beats/min) to 250 ms (240 beats/min) down by

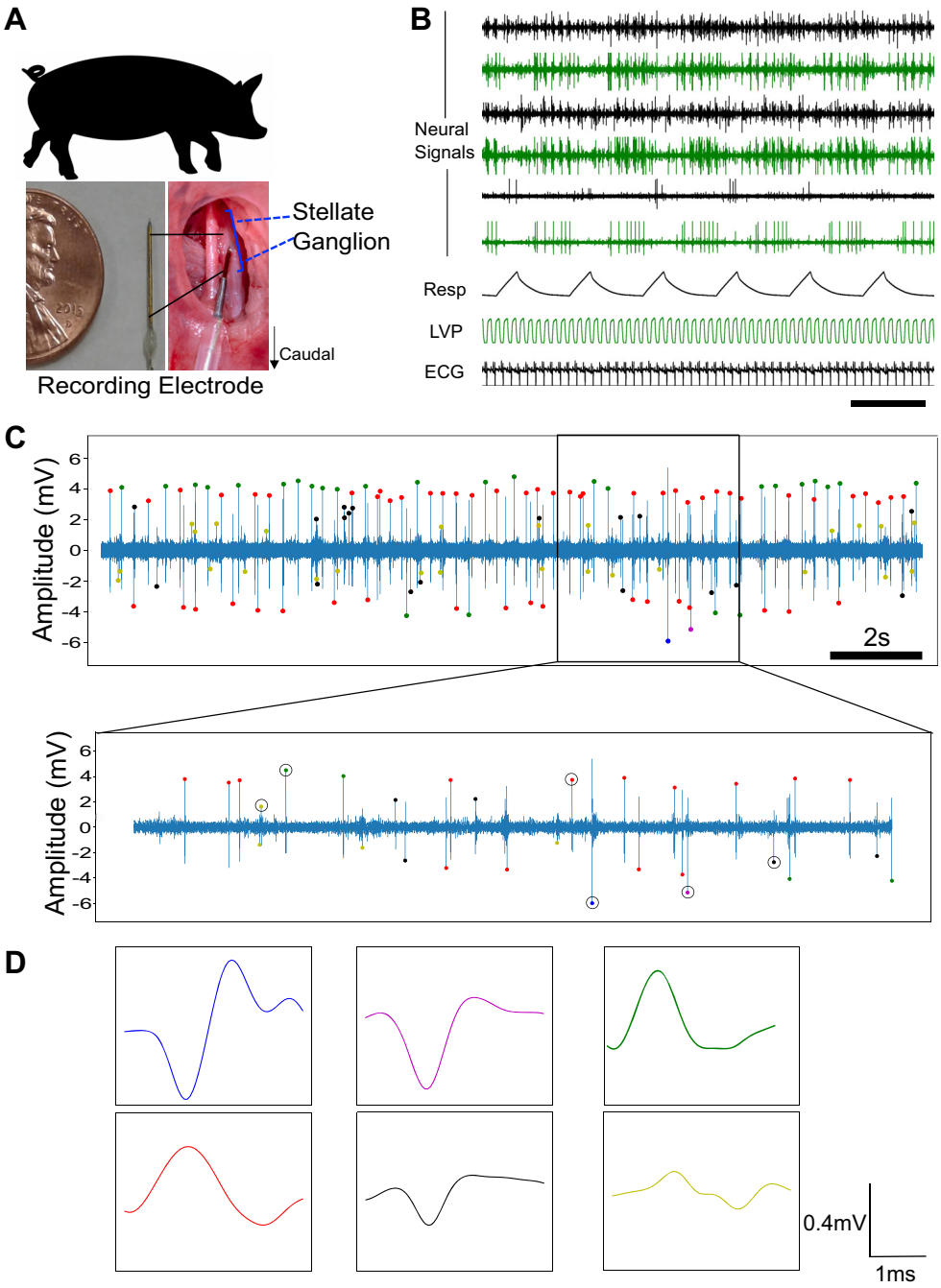

Figure 1. Experimental workflow. *A:* representative image of the recording linear microelectrode array in the pig left stellate ganglion. *B:* example of recordings of neural activity, respiratory pressure, left ventricular pressure, and electrocardiogram. *C*: the approach to spike sorting. *D*: examples of identified spikes. ECG, electrocardiogram; LVP, left ventricular pressure.

50 ms steps over 100 s using the Micropace (EP320) and Prucka CardioLab System (GE Healthcare). Bradykinin (20 μg/mL) applied epicardially to the ventricles were used to activate TRPV1 afferents. The heart was washed with warm saline 10 min after application and a 30-min waiting period was allowed for recovery of the baseline hemodynamic function.

Sliding Autocorrelation Definition

The spiking rate x_j, $1 \leq j \leq N_{\max}$ is found over a sliding window of fixed width time τ. Because the spikes occur at unequally spaced times, the equally sampled spiking rate computed at equally spaced times over a window of fixed width has a varying number of spikes per window. Therefore, the window width is chosen such that the mean spiking rate can be computed to a desired degree of accuracy.

The sliding autocorrelation of the spiking rate, found at equally spaced times t_j, $1 \leq j \leq N_{\max} - N$, where $N_{\max}$ is the total number of samples of x_j, $1 \leq j \leq N_{\max}$ and N is the number of samples in the j_{th} overlapping window, is

$$\rho_j(m) = \frac{E\left\{\left[x_{n(j)+m} - \mu_x\right]\right\}^2}{\sigma_x^2},$$

with shift $0 \leq m \leq N$. The sample times ranging over $j \leq n(j) \leq j + N$ have N windowed values and the upper limit on j

ensures that samples accessed within the last window do not exceed the index N_{max}. In this work, the autocorrelation is also centered by using N odd, and assigning j to $j + N/2$.

Neural Specificity Rationale and Definition

To evaluate this neural activity bias, a randomized spike histogram of left ventricular pressure (LVP) was computed over many cardiac cycles and subtracted from the neurally sampled LVP histogram (the LVP histogram computed from LVP evaluated at the time of spike occurrences).The randomized sampling of LVP follows the simple inverse proportionality to LVP slope previously described and provides a benchmark to evaluate neural activity bias. If there is no neural activity bias toward LVP, then the neurally sampled and randomly sampled histograms of LVP will be the same. Where the neurally sampled LVP histogram exceeds or goes below the randomly sampled LVP histogram, there is a respective positive or negative bias toward or away from that part of the LVP cycle. This neural activity bias was computed over a sliding window of fixed width of many cardiac cycles to also show its evolution. The results demonstrated that relative to random sampling of LVP, neuronal populations showed a strong positive and persistent bias toward near-peak systole and an equally persistent negative bias toward systole. The voltage level cutoff for the neurally sampled LVP was qualitatively chosen by identifying convergence of the metric for different lower limits.

The metric for specificity in neural activity is based on a normalized sliding histogram of a generic variable z_j, $1 \le j \le N_{max}$ at time t_j computed over a set of M bins and defined for the k_{th} bin as:

$$H(z_j)_k = \frac{h(z_j)_k}{\sum_{k=1}^{M} h(z_j)_k}.$$

Since the samples z_j occur at unequally spaced times, t_j, the sliding histogram assigned to time t_j is computed with reference to all z_j falling within a window of width τ at and beyond the sample time, t_j. As such, each histogram is based on a variable number of samples and the value of τ should be chosen to provide a desired degree of accuracy. In this work: *1*) the histogram is centered by using samples falling within $\tau/2$ before and after time t_j and *2*) the notation $H(z_j)_k$ is equivalent to the more convenient notation $Hz_{j,k}$ used below.

The steps below outline the method used to compute the neural specificity.

1) The sampled value of a physiological variable (e.g., LVP) at the time of each spike t_j, $1 \le j \le N_{max}$ such as neurally sampled LVP, defined as SLVPj, $1 \le j \le N_{max}$, is found and its normalized form $HSLVP_{j,k}$ is constructed.

2) The normalized histogram of equally spaced sampling of left ventricular pressure $LVP_{j,k}$ over the same epoch as in step *1*) is found and based on the same bins as those used for $HSLVP_{j,k}$. This normalized histogram approximates the same found by random sampling.

3) The neural specificity follows from considering step *2* relative to step *1* as $\alpha_{j,k} = HSLVP_{j,k} = LVP_{j,k}$ and to enable a consistent comparison through time, space, and across data sets, the neural specificity is "normalized" by scaling $\alpha_{j,k}$ to zero mean and unit variance with respect to $\alpha_{j,k} > 0$ and labeled as $A_{j,k}$.

There are three cases of interest:

1) $A_{j,k} > 0$: Greater bias toward the value of the physiological variable at the k_{th} bin than that due to random sampling.
2) $A_{j,k} < 0$: Lesser bias toward the value of the physiological variable at the k_{th} bin than that due to random sampling.
3) $A_{j,k} \approx 0$: Near-zero bias toward the k_{th} bin value of the physiological variable and this approximates random sampling.

For ease of visualization and qualitative interpretation, the sliding window histogram of neural specificity is mapped to the discrete set -1, 0, 1 and, respectively, colored as blue, teal, and yellow. All values of the bias histogram at or exceeding a threshold of α are set to 1, all values between $-\alpha$ and $+\alpha$ are set to 0, and all values at or below $-\alpha$ are set to -1. Specifically, the colors blue, teal, and yellow, respectively, imply a qualitative tendency toward less, the same, and greater degree of bias in neural activity than that expected from random sampling.

Statistical Analysis

Variables are presented as means ± SE. The Shapiro–Wilk test was used for assessing distribution. A two-tailed Student's t test and ANOVA test were used for data that were normally distributed, and the Mann–Whitney test and Kruskal–Wallis test were used for data that were not normally distributed. Statistical significance were indicated at P values of <0.05, <0.01, <0.001, and <0.0001. Analysis was performed using Microsoft Excel (Redmond, WA) and GraphPad Prism (La Jolla, CA).

RESULTS

The experimental and data workflows are shown in Fig. 1. Linear microelectrode arrays (16-channel) were impaled into SGs, as shown in Fig. 1*A*, to record neural activity. Simultaneously, left ventricular pressure (LVP), respiratory pressure (RP), and electrocardiogram (ECG) were recorded (Fig. 1*B*). Raw tracings (example shown in Fig. 1*C*) were subjected to artifact removal and spike detection as shown in Fig. 1*D*. Representative examples of detected spikes are shown in Supplemental Fig. S2. Spike detection was optimized to yield significantly more than would be obtained by a single positive or negative threshold. By iteratively detecting and masking spikes as described, we obtained ~400,000 spikes (Supplemental Fig. S3) from a single channel during 8 h of continuous experimental recordings.

Spatiotemporal Dynamics of Stellate Ganglion Neuronal Populations Reflects Regional Processing

An immunofluorescent image of a porcine left SG with a schematic of the recording array is shown in Fig. 2*A* (see Table 1 for antibodies). Recorded activity showed spatiotemporal differences across the ganglion. Initially, there was a robust activity recorded upon insertion of the electrode that abated after ~2 h (Fig. 2*B*). When this activity became less pronounced, a steady state was reached (Fig. 2*C*). Mean firing frequency across electrodes in the entire cohort was 4.6 ± 1.2

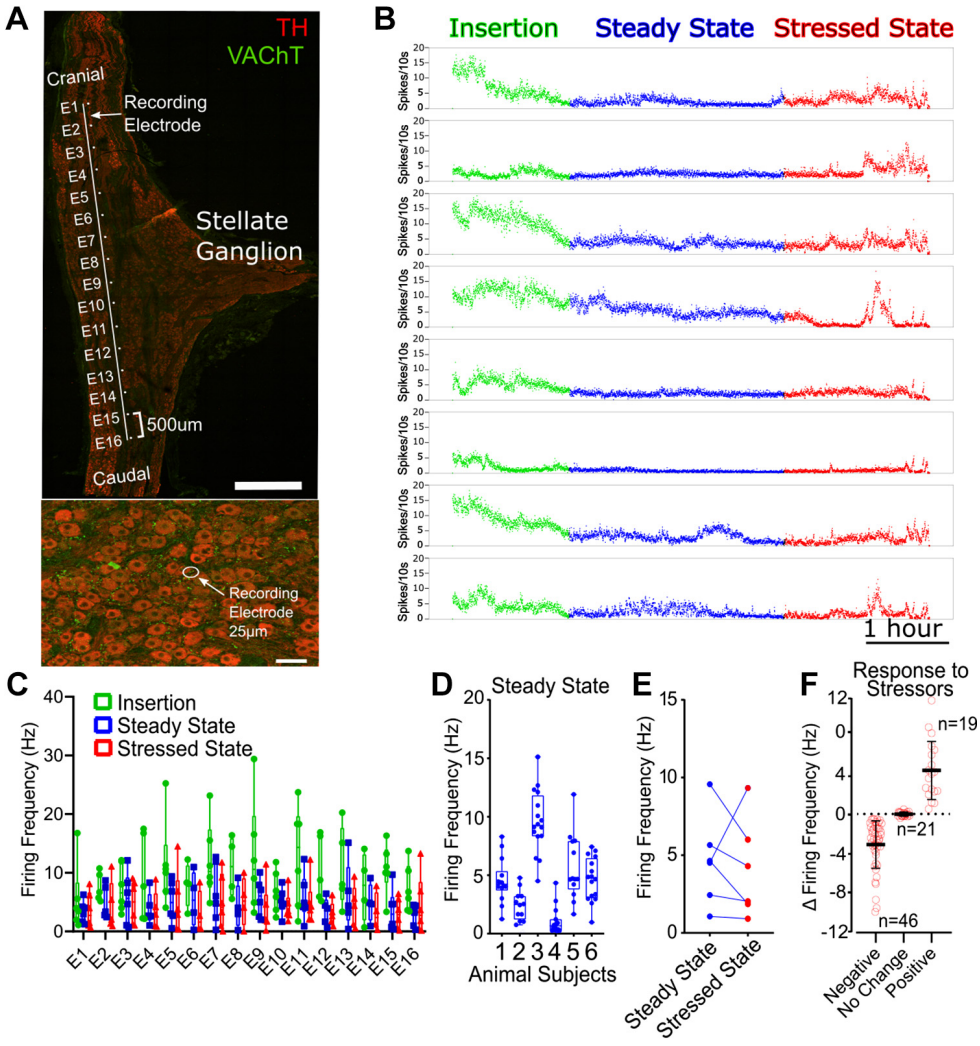

Figure 2. Spatiotemporal dynamics of stellate ganglion neuronal populations. *A*: schematic of the 16-electrode array inserted into the ganglion (*upper*) and actual size of recording electrode relative to neurons (*lower*). Spike dynamics over 8 h in eight channels spanning the stellate ganglion (*B*); plot of firing frequencies across all 16 electrodes (E1–E16) in six male study animals upon insertion of the probe, during steady state, and during cardiopulmonary stressors (*C*); mean firing frequencies across the ganglion in study animals (*D*); mean firing frequencies across the ganglion in the study animals (*E*); distribution of responses to several cardiovascular stressors including aorta occlusion, rapid ventricular pacing, ischemia, apnea plotted as differences in mean firing between steady and stressed states (*F*).

Hz (intersubject range 1.1–9.6 Hz; Fig. 2*D*). Firing frequency was nonuniform across ganglia in all animals, suggesting regional processing within the ganglion. The difference across ganglia in each subject ranged from 4.1 Hz to 10.6 Hz.

Similarly, introduction of cardiovascular (i.e., great vessel occlusion, cardiac ischemia, and rapid ventricular pacing) and pulmonary stressors (i.e., apnea, hypopnea, and tachypnea) resulted in varied responses across the ganglion (Fig. 2, *B, E,* and *F*) with some regions responding minimally. The extent of variation in responses from steady to stressed states did not yield significant results using a paired *t* test (not shown). Interestingly, although sympathoexcitatory reflex response to stressors is thought to be reflected by increased SG neuronal firing, we observed a reduction in neural activity across most electrodes (Fig. 2*F*). This pattern is indicative of processing within the ganglion, as reflex inhibition of neural activity was associated with sympathoexcitation.

Temporal Local Dynamics

We next examined local spike dynamics in the context of cardiac and pulmonary activity, that is, LVP and RP, respectively. Representative tracings of spike activity, RP, LVP, and ECG are shown in Fig. 3*A*. Modulation of spike activity by the respiratory cycle (yellow highlight, inspiration and

Table 1. *List of antibodies used*

	Concentration	Source
Primary antibody		
Vesicular acetylcholine transporter	1:200	Polyclonal rabbit antibody. Synaptic Systems, Goettingen, Germany. #139-103.
Tyrosine hydroxylase	1:200	Polyclonal sheep antibody. EMD Millipore. Darmstadt, Germany. ab1542.
Secondary antibody		
Cy3 AffiniPure aonkey anti-rabbit IgG	1:400	Polyclonal rabbit antibody. Jackson Immunoresearch Laboratories, Inc., West Grove PA. 711-165-152.
Alexa flour 488 AffiniPure donkey anti-sheep IgG	1:400	Polyclonal sheep antibody. Jackson Immunoresearch Laboratories, Inc., West Grove PA. 713-545-003.

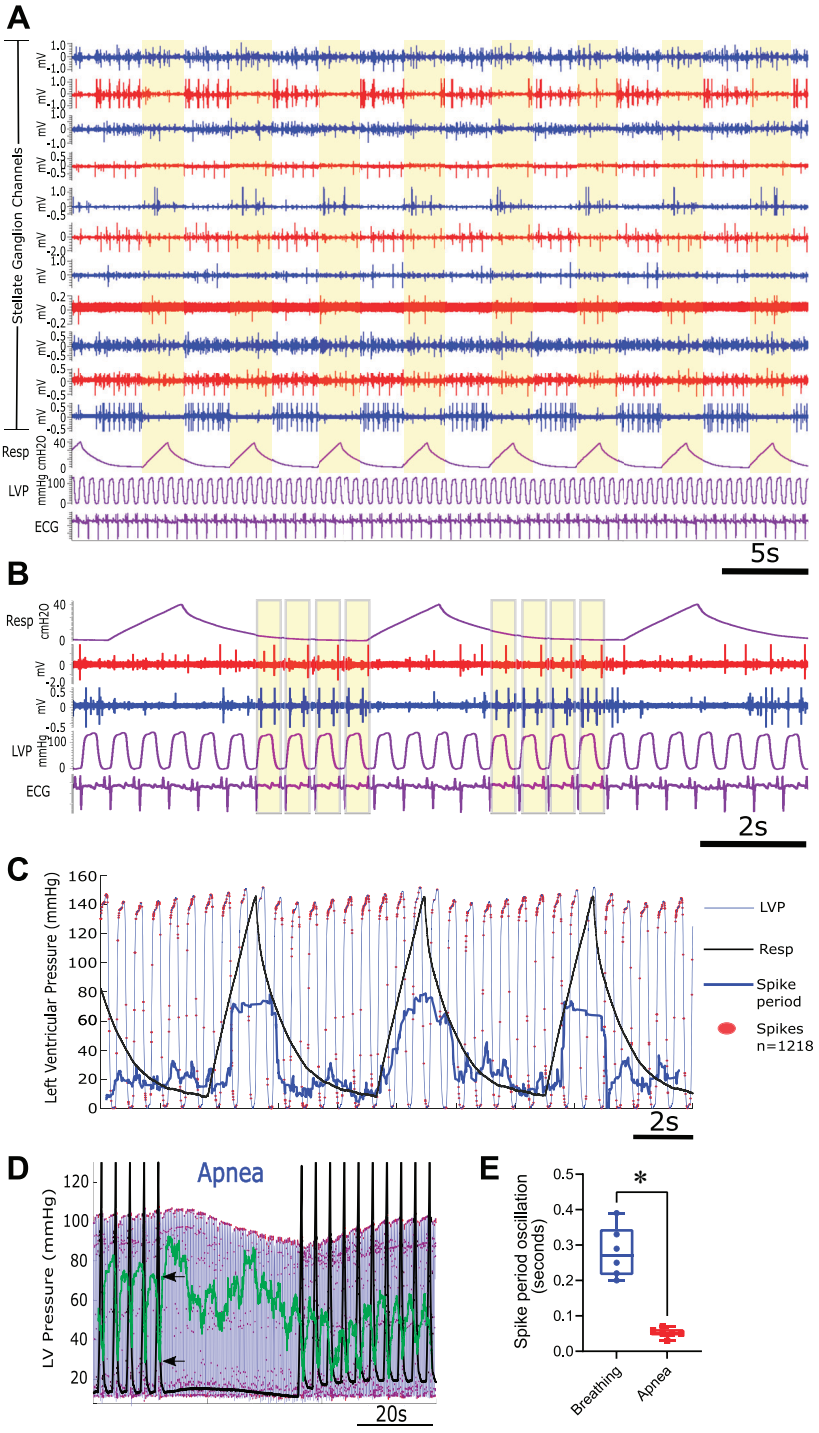

Figure 3. Cardiopulmonary integration is reflected in stellate ganglion neural activity. *A* and *B*: representative recordings from several electrodes (blue and red tracings) using the 16-channel linear array, along with respiration (Resp), left ventricular pressure (LVP), and the electrocardiogram (ECG) in purple tracings. Yellow bars highlight respiration (*A*) and the cardiac cycle (*B*). Activity in the blue and red channels are locked to cardiac and/or pulmonary. *C*: stellate ganglion (SG) neuron activity (red dots are individual spikes) shows increased firing rate at peak and near-peak LV pressures; however, firing is inhibited during respiration, as reflected by increased spike period (heavy blue line) mirroring inspiration and expiration. *D*: representative response of SG neural activity to apnea (60 s). Black trace is scaled up respiratory activity, and black arrows identify baseline peak and trough of the spike period (green trace). *E*: spike period oscillation (peak-trough values) while breathing at baseline, and over the same period in apnea. n = 6 animals; $*P$ = 0.016, two-tailed Wilcoxon rank-sum test.

expiration) can be readily identified. Spike activity was inhibited during the respiratory cycle when lung pressure was >0 cmH_2O (Fig. 3, *A* and *B*). This resulted in a cyclic pattern where spike period, the interval between successive spikes, increased and decreased in tandem with respiratory pressure during the respiratory cycle (Fig. 3*C*).

A subset of channels showed 1:1 phase locking to the cardiac cycle; two such channels are shown in Fig. 3*B*. The cardiac cycle, highlighted in yellow, is associated with phase-locked spikes in the red and blue channels and this was only present for respiratory pressures at or near 0 cmH_2O. Such association with cardiac and pulmonary activity is reflective of integrated cardiopulmonary processing. This observation is further illustrated (Fig. 3*C*) by the timing of neural activity, where individual spikes are shown as red dots relative to LVP and RP. Most spikes are clustered at peak, or near-peak, LV pressure, and are relatively inhibited during inspiration (arrows). This cyclic inhibition is illustrated by the evolution of spike period (blue line) in Fig. 3*C*. To verify the influence of breathing on spike dynamics, we instituted apnea by

transiently stopping the ventilator (30–60 s). Interestingly, we found that the oscillations in spiking activity entrained by breathing were abolished (Fig. 3, *D* and *E*). Next, we sought to assess whether the oscillations could be completely delinked from cardiac dynamics. In a subset of animals, we induced ventricular fibrillation by applying an electrical pulse to the heart. In this setting (data not shown), transiently stopping and resuming respiration via the ventilator also attenuated and reestablished the oscillations in firing. Taken together, these data demonstrate the contribution of both cardiac and respiratory function to SG neuronal population dynamics.

Transduction of Cardiopulmonary Function

To determine whether heart rate and respiratory rate are reflected in spike population dynamics over long-time scales, we used a sliding window autocorrelation to look for the presence of periodicities in spike density linked to changes in heart rate and respiratory rate. The autocorrelation analysis is shown at baseline and during cardiovascular and pulmonary stressors (Fig. 4, *A*–*D*). The analysis revealed weak correlation with heart rate but a near-perfect correlation with respiratory rate. With respect to respiratory rate, the strong correlation is consistent with local activity previously described (Fig. 3) over a duration of several hours.

To extract aspects of cardiopulmonary function present in neurotransmission, we examined bias of neural activity regarding LVP and RP. We specifically sought to determine whether the relationship between spike timing and LVP (or RP) as shown in Fig. 4, *A* and *B*, is merely proportional to the inverse slope of LVP or RP (e.g., systole vs. diastole and inspiration vs. expiration). In other words, if there were no specific relationship between spike timing and cardiac, or respiratory, phase, then spike timing would mirror the duration of each LVP (or RP) phase as occurs in random firing.

To do this, we devised the metric to evaluate bias in neural activity (Supplemental Fig. S4) to determine whether spikes were over- or underrepresented at each LVP (or RP) phase relative to random association, that is, we established whether or not neurons were biased toward a specific phase of the cardiopulmonary cycle as compared with random sampling. We draw on a similar work that explores associations of neural populations with external stimuli in the visual cortex of the mice for the neural specificity metric (18). A sliding window comparison was made between the LVP at the time of recorded spikes, and the distribution of recorded LVP over the same epoch, which represented random sampling. The results showed that spiking activity, relative to random sampling, was overrepresented at near-peak LVP (Supplemental Fig. S4*C*, yellow bars) and underrepresented at peak systole and diastole (dark blue bars). When examined

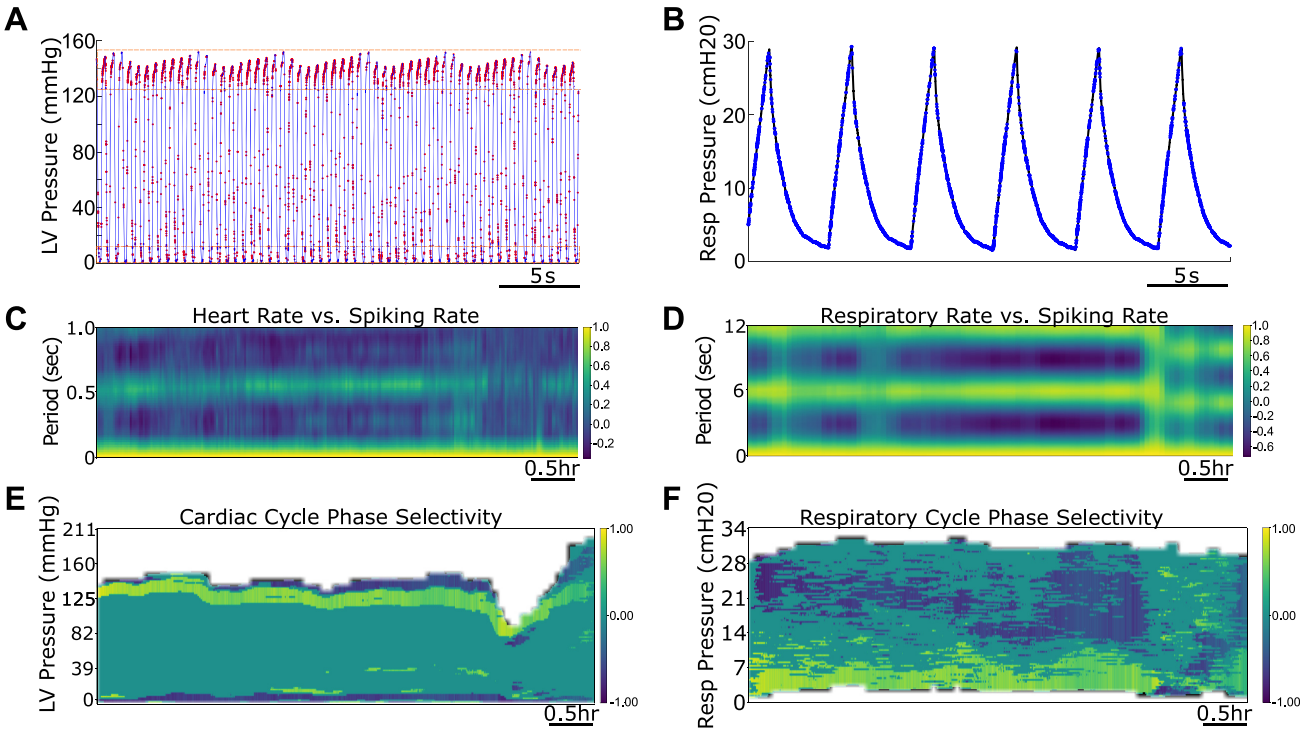

Figure 4. Periodicity in spiking activity reflects specificity for a narrow range of LVP and respiratory rate. *A*: left ventricular pressure (LVP) is plotted in blue tracings along with individual spikes as red dots. *B*: respiratory pressure is plotted in black tracings with individual spikes superimposed as blue dots. *C* and *D*: autocorrelation of spiking activity calculated for equally spaced windows for different lags over the course of an experiment. The autocorrelation value (between −1 and 1) is represented by the color scheme shown in *C* and *D*. Maximum autocorrelation (one) of the spiking activity in a window for a particular lag represents periodicity in the spiking activity for that lag. The plot of the sliding autocorrelation reveals the heart rate and the respiration rate with the spiking activity being highly correlated for the respiratory period (5 s) and the heart period (0.5 s). The respiration rate (*D*) is revealed more clearly than the heart rate (*C*). *E* and *F:* the neural bias toward LVP and respiratory pressure for the duration of the experiment (near-zero bias is teal, positive bias is yellow, and negative bias is blue). *E*: the degree of bias in neural activity toward specific LVP over the course of the experiment. *F:* the same with respect to the respiratory pressure.

over longer periods (Supplemental Fig. S4, *D–F* and Fig. 4*E*), this relationship remained stable, as was the case across study animals (not shown). With regard to respiratory pressure, evaluation of neural specificity yielded a less specific airway pressure ranged at which spikes were over- or underrepresented (Fig. 4*F*).

To investigate the spatial coherence of neural specificity, we applied it to individual electrodes spatially distributed across the SG (Fig. 5). Across the ganglion, the rising phase of the LVP tracing had a higher degree of specificity in neural activity. However, the blood pressure range to which spikes were related, varied geographically across the ganglion. In some channels, bias in neural activity also appeared to be transient. Collectively, these behaviors likely reflect the spatiotemporal structure of network function throughout the ganglion.

The totality of these observations indicate that richly organized neural networks are present in the stellate ganglion. Some of this organization is reflected in relatively different stellate ganglion spike dynamics in relation to the cardiac and pulmonary cycles. Although spike density was weakly correlated to heart rate, it was strongly associated with a specific range of LVP. On the other hand, whereas respiratory rate was strongly correlated with spike dynamics and reflected in respiratory modulation of neural activity, a weaker association was present between spike activity and RP.

Spike rate does not predict the degree of neural specificity.

We sought to determine whether neural specificity conveyed information that is independent of spike frequency dynamics. We plotted the mean and standard deviation of firing frequency from multiple channels with the associated neural bias (Fig. 6). Data from three animal subjects are shown. The bias remained stable over several hours in each animal subject and was independent of swings in mean firing frequency and standard deviation. This suggests that the neural bias conveys information regarding the relationship between neural activity and cardiopulmonary indices that is independent of the frequency of neural activity in the ganglion.

Specificity in Neural Activity toward near Systole is Independent of Blood Pressure

Next, we sought to determine whether the specificity in neural activity toward the near-peak systolic phase of the cardiac cycle observed in Figs. 4 and 5 reflected neuronal tracking of LVP or a cardiac mechanical event, such as isovolumetric contraction or opening of the aortic valve. Specifically, we aimed to determine whether raising or lowering LVP abolished any specificity in neural activity, as cardiac mechanical events occur despite hypotension, normotension, or hypertension. To examine this, we performed stressors to perturb LVP [specifically occlusion of the aorta and inferior vena cava (IVC)] and compared the spiking probability at different phases of the LVP before, during, and after the cardiac stressors. Lowered LVP induced by transiently reducing preload (IVC occlusion) did not impact spike probability in the near-peak systolic phase (Fig. 7, *A–C*). Similarly, increased LVP elicited by rapidly increasing blood pressure in the aortic arch by thoracic aortic occlusion did not change spiking probability in the systolic phase. Although these interventions did not alter spiking probability in the near-peak systolic range, it increased the spike period (i.e., reduced firing frequency) across all subjects.

Next, we assessed whether neural specificity for near-peak systole was modulated by cardiac chemo-afferent input, by applying bradykinin (40 μg/mL) to the epicardium for 60 s. The application of bradykinin caused an immediate increase in spiking activity as shown in representative recordings (Supplemental Fig. S5*A*) and a decrease in spike period (i.e., increased firing frequency) (Supplemental Fig. S5, *A* and *B*). This decrease was found to occur following a sharp increase in the spike period (Supplemental Fig. S5*B*). This could be due to an ancillary response to the application of bradykinin. [However, chemical activation of cardiac afferents did not impact the neural bias toward spiking at near-peak systolic (Supplemental Fig. S5, *C* and *D*)].

These results suggest that the selectivity of neuronal activity for the near-peak systolic phase likely reflects cardiac mechanics not LVP or chemo-afferent function, and indicate that SG neurons closely track cardiac mechanical indices.

DISCUSSION

Using a novel approach to link neuronal population dynamics in SG to cardiopulmonary physiology, our major findings indicate that: *1*) SG neurons exhibit dynamic spatiotemporal activity reflective of network processing of afferent inputs; *2*) the activity of neuronal populations exhibits a high degree of cardiopulmonary integration; and *3*) cardiac dynamics are transduced by SG neurons as reflected by a specificity in neural activity for spiking near-peak systole. These findings represent the first demonstration of the complex-integrated cardiopulmonary regulation inherent in sympathetic ganglia.

The Stellate Ganglion as an Integrator of Cardiopulmonary Function

To date, neural recordings derived from intrathoracic extracardiac ganglionic neurons in situ have not involved any description of networking within such populations in the context of the cardiopulmonary control hierarchy (3, 14, 17, 19) as considered here. Although data from existing literature has separately considered cardiac and pulmonary regulation, we determined that many of the neurons located in intrathoracic extracardiac ganglia transduce both cardiac and pulmonary dynamics. This indicates that considering one index without the other may be an artificial representation of local neural control.

There is strong rationale for cardiopulmonary integration, for example, the heart rate response to deep breathing, which strongly links cardiac and pulmonary function to maintain cardiac output. The finding of neural activity responding to both cardiac and pulmonary inputs identifies a neural signature for integrated cardiopulmonary function in the stellate ganglion. The anatomic basis for this finding may be related to local processing within the stellate ganglion and/or from projections into the ganglion from arterial baroreceptors (19). Specifically, efferent postganglionic

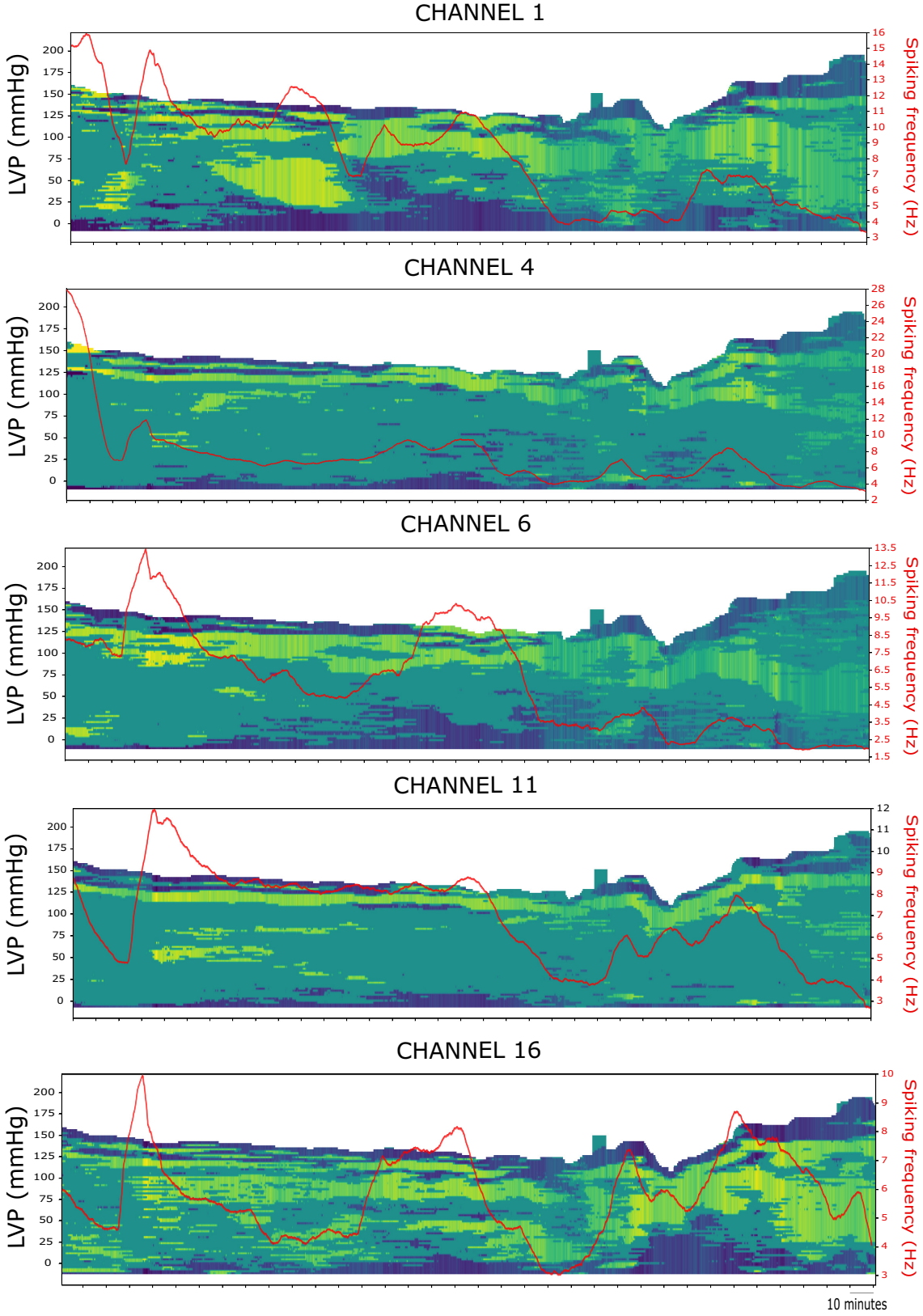

Figure 5. Regionality of cardiac cycle specificity in neural activity. Bias in neural activity plotted for the duration of the experiment across five channels in one animal subject, with the spike rate superimposed as a red line. The five channels plotted are arranged according to the spatial arrangement of the electrodes across the ganglion. This plot indicates that within each channel the bias in neural activity is relatively consistent over time while spike is highly variable. On the other hand, spike rate across channels shows some degree of consistency, whereas the bias in neural activity is relatively more variable.

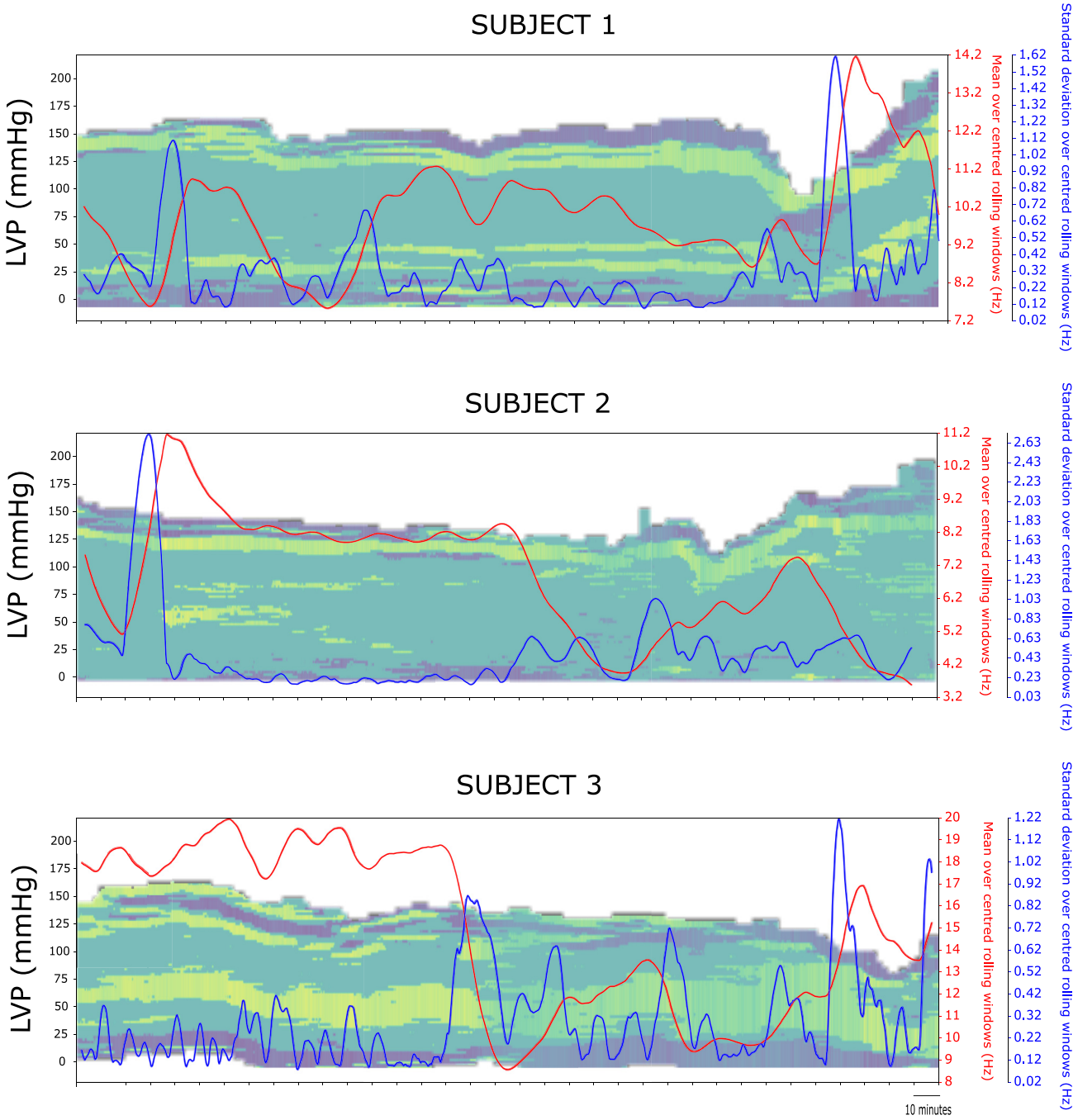

Figure 6. Dynamic changes in neuronal spiking density does not impact cardiac cycle phase specificity. The number of spikes (red line) and associated variation (blue line) are computed from the mean and standard deviation of spiking frequency calculated from sliding windows of 10-min width. These are superimposed over the remaining phase selectivity image. Changes in the number of spikes and their variation are not uniquely associated with the phase selectivity or changes in systolic pressure. Changes in the same computation across different animals show little consistency within, or among, animals of the spiking activity and its variation with respect to LVP. The degree of phase selectivity to LVP just below the systolic pressure is consistent across animals despite wide variations in systolic pressure. LVP, left ventricular pressure.

neurons to the heart and lungs are predominantly localized to the cranio-medial pole of the mammalian stellate ganglia (19–21). As such, our recordings across the stellate ganglion likely captured the activity of local circuit neurons (LCNs) predominantly. LCNs have been functionally demonstrated in the stellate ganglion (14), and are the likely population integrating cardiopulmonary function as identified in this work.

Spatiotemporal Population Dynamics is Context Dependent

Our findings demonstrate that the activities generated by neurons distributed throughout stellate ganglia demonstrate temporal dynamics and variations in regional coherence of network processing. Specifically, we found that activities generated by neurons located throughout stellate ganglia are

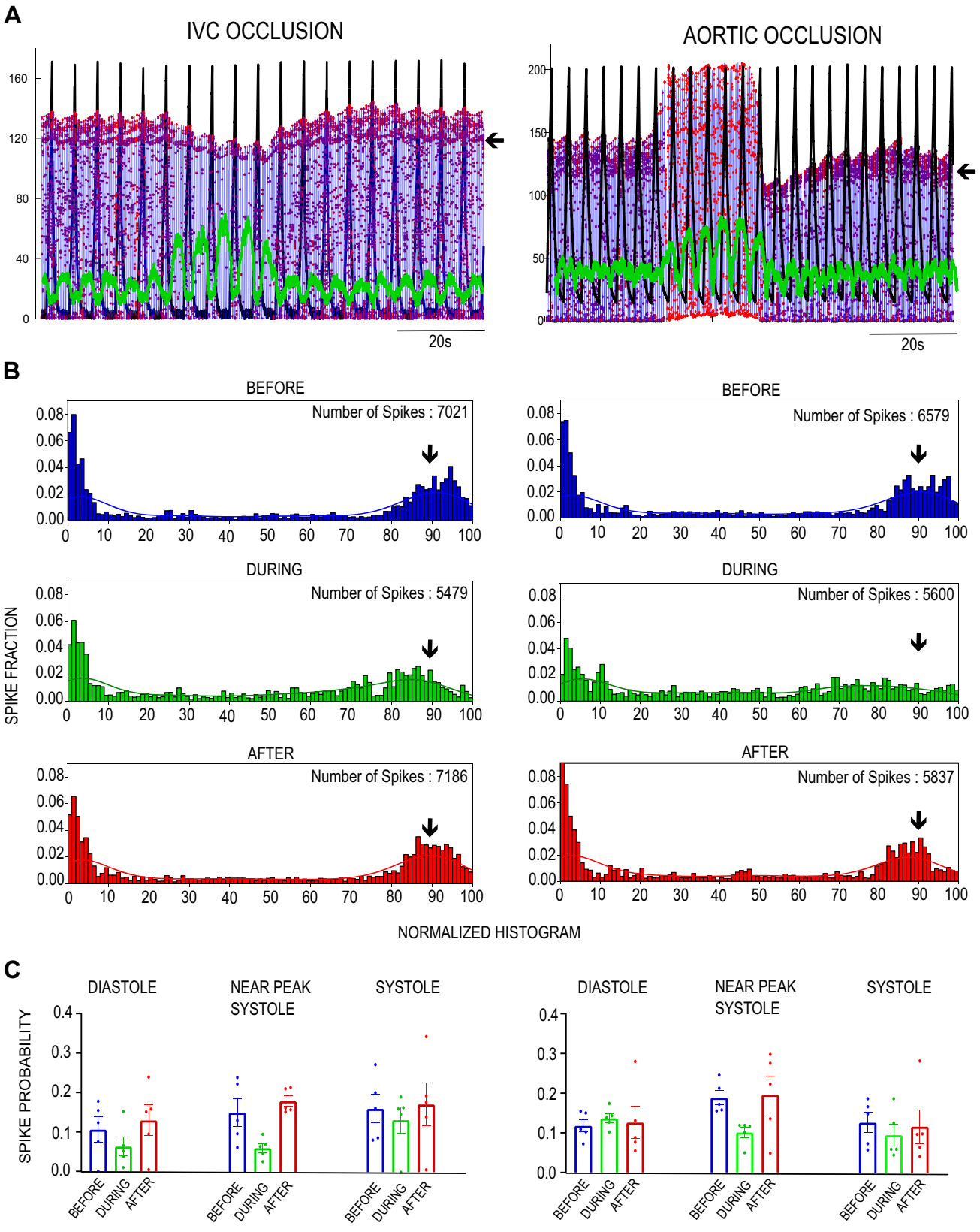

Figure 7. Near-peak systolic phase selectivity is independent of blood pressure. *A*: spike periodicity (green tracings) plotted along with the left ventricular pressure (LVP) in blue tracings and respiration in black tracings for two stressors—inferior vena cava (IVC) and aortic occlusion use to lower and raise LVP, respectively. Stellate ganglion neuron activity (individual spikes plotted as red dots) is shown in response to IVC and aortic occlusion. Near-peak systolic phase selectivity is indicated by the arrows. *B*: spike fraction is plotted as a histogram and a distribution for normalized LVP before (blue tracings), during (green tracing) and after (red tracings) for the interventions plotted in *A*. *C*: spike probability (area under the curve of spike fraction distribution) is plotted for systole (*left*) and diastole (*right*) for before (blue), during (green) and after (red) the two interventions. $n = 5$ animals/condition, two-tailed analysis of variance for all comparisons were not statistically significant.

not only selective to cardiac and respiratory control, but also that such activities are dynamic over time. This is reflected by spiking-density variations during basal resting states as well as following the introduction of various cardiopulmonary stressors. Even within the resting state, differences in the activity generated by neurons in some regions was dynamic, likely suggesting ongoing adaptations to cardiopulmonary sensory inputs over time in basal states.

Differential Reflection of Cardiac and Pulmonary Inputs in Stellate Ganglion Spatiotemporal Processing

Autocorrelation of the neural activities generated by populations of neurons throughout individual stellate ganglia indicates a strong periodicity of their activities associated with respiratory rate—with relatively less associations with heart rate. This may be explained by the periodic inhibition of neural activity that occurs during respiration inflation (Fig. 3*C*) such that the relationship of their activities to heart rate is not as strong. This may be partly due to the fact that compared with respiration, an order of magnitude reduction in the number of spikes available to resolve the heart rate was evident (i.e., spikes available in 0.5-s interval for heart rate vs. 6 s for respiratory dynamics). Although this observation implies that the periodicity of stellate ganglion neuronal activity is very much linked to respiratory dynamics, it does not describe how cardiac and respiratory function are linked neuronally within stellate ganglia, particularly during control states.

Furthermore, we examined interactive control between the LVP and RP cycles and neuronal activity. We found that although neuronal activity is strongly modulated by specific phases of LVP, it is less so for respiratory dynamics. This is shown in Fig. 5, *E* and F, where a strong link to a narrow range of LVP (yellow band) is readily observed, but such linkage to RP mechanics is less precise. The degree of bias in neural activity to specific ranges of LVP is maximal near-peak systole (possibly reflecting aortic valve opening, maximal LV papillary muscle contraction, and/or other critical events in the cardiac cycle). This illustrates the very selective nature of neural activity generated with respect to LVP when it occurred during each cardiac cycle. Such bias in neural activity toward cardiac and pulmonary function reflect the differential transduction of cardiac and pulmonary mechanics by SG.

LIMITATIONS

The neural specificity metric explored in this study dynamically looks at the association of population dynamics with a target index such as LVP or respiratory pressure. Although it is effective in giving an insight into the dynamics of transduction of such afferent inputs, it does not provide a basis to infer about the source or the causality of such inputs. The SG neural populations receive direct afferent input due to a small fraction of afferent soma present in the ganglion. The stellate also receives indirect afferent input from the intermediolateral regions for processing along with efferent outflow. The neural specificity metric does not have a way of resolving the source or cause of such activity. This would restrict addressing specific questions such as direct or indirect respiratory feedback, activation of baroreflex from aortic occlusion, or effects of a decreased preload to only the dynamic transduction of their final target indices. Future experiments can be designed to include experimental protocols to address such questions with the metric.

Another limitation of the study lies in classifying detected action potentials based on region and function. The competitive masking algorithm was aimed at detecting action potentials at multiple voltage levels. Although effective at obtaining the population activity, the algorithm does not classify the detected neurons based on function such as afferent, efferent, or local circuit neurons or features of the detected neurons such as the shape of the action potential. Addressing these limitations would be the subject of future experiments with spike sorting as an additional pipeline to the algorithm.

Differences in population response during individual stressors compared with steady state around the intervention did not yield significant results owing to a small sample of data during the stressor (30–60 s). In the future, experiments will be designed to include longer interventions to include a larger sample of data in order to explore this question.

Conclusions

In summary, the activity generated by SG neurons shows that their different populations receive differential cardiac and pulmonary inputs that influence dominant populations of neurons (3). These populations track, via the ganglion's respiratory and cardiac afferent inputs (likely mechanosensory), cardiopulmonary dynamics to generate integrative control. Furthermore, these data demonstrate the extent and manner with which SG act as a primary peripheral integrative source for continuous cardiopulmonary functional integration. These findings have important implications for pathological states, where a reduction in spatial coherence of control across the ganglion may reflect deranged cardiac-pulmonary integrative control. Whether such derangements can serve as a biomarker of risk or can be targeted therapeutically remains to be determined and should be the focus of future studies on cardiopulmonary neuromodulation.

SUPPLEMENTAL DATA

Supplemental Figs. S1–S5: https://doi.org/10.6084/m9.figshare.14347061.v2.

ACKNOWLEDGMENTS

We thank Gohar Mirhanian, William Narinyan, and Amiksha Gandhi for excellent technical assistance and Drs. Jeffrey Ardell and Kalyanam Shivkumar for comments on the manuscript.

GRANTS

This study was supported by National Institutes of Health Grants HL125730, OT2OD023848, and DP2HL142045 (to O.A.A.).

DISCLOSURES

O.A.A. reports having equity in NeuCures. None of the other authors has any conflicts of interest, financial or otherwise, to disclose.

AUTHOR CONTRIBUTIONS

J.A.A., G.K., and O.A.A. conceived and designed research; Y.H., M.A.S., C.W., J.A.A., G.K., and O.A.A. performed experiments; K.B.S., Y.H., M.A.S., A.C.K., C.W., G.K., and O.A.A. analyzed data; K.B.S., Y.H., A.C.K., C.W., J.A.A., G.K., and O.A.A. interpreted results of experiments; K.B.S., A.C.K., G.K., and O.A.A. prepared figures; K.B.S., A.C.K., J.A.A., G.K., and O.A.A. drafted manuscript; K.B.S., Y.H., M.A.S., A.C.K., C.W., J.A.A., G.K., and O.A.A. edited and revised manuscript; K.B.S., Y.H., M.A.S., A.C.K., C.W., J.A.A., G.K., and O.A.A. approved final version of manuscript

REFERENCES

1. **Ardell JL**, **Andresen MC**, **Armour JA**, **Billman GE**, **Chen P-S**, **Foreman RD**, **Herring N**, **O'Leary DS**, **Sabbah HN**, **Schultz HD**, **Sunagawa K**, **Zucker IH.** Translational neurocardiology: preclinical models and cardioneural integrative aspects. *J Physiol* 594: 3877–3909, 2016. doi:10.1113/JP271869.
2. **Armour AJ**, **Ardell , JL.** *Basic and Clinical Neurocardiology*. New York: Oxford University Press, 2004.
3. **Armour JA.** Activity of in situ stellate ganglion neurons of dogs recorded extracellularly. *Can J Physiol Pharmacol* 64: 101–111, 1986. doi:10.1139/y86-016.
4. **Bosnjak ZJ**, **Kampine JP.** Cardiac sympathetic afferent cell bodies are located in the peripheral nervous system of the cat. *Circ Res* 64: 554–562, 1989. doi:10.1161/01.res.64.3.554.
5. **Randall WC**, **Szentivanyi M**, **Pace JB**, **Wechsler JS**, **Kaye MP.** Patterns of sympathetic nerve projections onto the canine heart. *Circ Res* 22: 315–323, 1968. doi:10.1161/01.res.22.3.315.
6. **Ajijola OA**, **Yagishita D**, **Reddy NK**, **Yamakawa K**, **Vaseghi M**, **Downs AM**, **Hoover DB**, **Ardell JL**, **Shivkumar K.** Remodeling of stellate ganglion neurons after spatially targeted myocardial infarction: neuropeptide and morphologic changes. *Heart Rhythm* 12: 1027–1035, 2015. doi:10.1016/j.hrthm.2015.01.045.
7. **Han S**, **Kobayashi K**, **Joung B**, **Piccirillo G**, **Maruyama M**, **Vinters HV**, **March K**, **Lin S-F**, **Shen C**, **Fishbein MC**, **Chen P-S**, **Chen LS.** Electroanatomic remodeling of the left stellate ganglion after myocardial infarction. *J Am Coll Cardiol* 59: 954–961, 2012. doi:10.1016/j.jacc.2011.11.030.
8. **Nakamura K**, **Ajijola OA**, **Aliotta E**, **Armour JA**, **Ardell JL**, **Shivkumar K.** Pathological effects of chronic myocardial infarction on peripheral neurons mediating cardiac neurotransmission. *Auton Neurosci* 197: 34–40, 2016. doi:10.1016/j.autneu.2016.05.001.
9. **Ajijola OA**, **Chatterjee NA**, **Gonzales MJ**, **Gornbein J**, **Liu K**, **Li D**, **Paterson DJ**, **Shivkumar K**, **Singh JP**, **Herring N.** Coronary sinus neuropeptide Y levels and adverse outcomes in patients with stable chronic heart failure. *JAMA Cardiol* 5: 318–325, 2020. doi:10.1001/jamacardio.2019.4717.
10. **Ajijola OA**, **Wisco JJ**, **Lambert HW**, **Stark EM**, **Mahajan A**, **FIshbein MC**, **Shivkumar K.** Extra-cardiac neural remodeling in humans with cardiomyopathy and arrhythmias. *Auton Neurosci* 177: 1–65, 2013. doi:10.1016/j.autneu.2013.05.030.
11. **Ajijola OA**, **Lellouche N**, **Bourke T**, **Tung R**, **Ahn S**, **Mahajan A**, **Shivkumar K.** Bilateral cardiac sympathetic denervation for the management of electrical storm. *J Am Coll Cardiol* 59: 91–92, 2012. doi:10.1016/j.jacc.2011.09.043.
12. **Vaseghi M**, **Barwad P**, **Malavassi Corrales FJ**, **Tandri H**, **Mathuria N**, **Shah R**, **Sorg JM**, **Gima J**, **Mandal K**, **Sàenz Morales LC**, **Lokhandwala Y**, **Shivkumar K.** Cardiac sympathetic denervation for refractory ventricular arrhythmias. *J Am Coll Cardiol* 69: 3070–3080, 2017 [Erratum in *J Am Coll Cardiol* 70: 811, 2017]. doi:10.1016/j.jacc.2017.04.035.
13. **Vaseghi M**, **Zhou W**, **Shi J**, **Ajijola OA**, **Hadaya J**, **Shivkumar K**, **Mahajan A.** Sympathetic innervation of the anterior left ventricular wall by the right and left stellate ganglia. *Heart Rhythm* 9: 1303–1309, 2012. doi:10.1016/j.hrthm.2012.03.052.
14. **Armour JA.** Synaptic transmission in the chronically decentralized middle cervical and stellate ganglia of the dog. *Can J Physiol Pharmacol* 61: 1149–1155, 1983. doi:10.1139/y83-171.
15. **Armour JA**, **Collier K**, **Kember G**, **Ardell JL.** Differential selectivity of cardiac neurons in separate intrathoracic autonomic ganglia. *Am J Physiol Regul Integr Comp Physiol* 274: R939–R949, 1998. doi:10.1152/ajpregu.1998.274.4.R939.
16. **Yoshie K**, **Rajendran PS**, **Massoud L**, **Kwon O**, **Tadimeti V**, **Salavatian S**, **Ardell JL**, **Shivkumar K**, **Ajijola OA.** Cardiac vanilloid receptor-1 afferent depletion enhances stellate ganglion neuronal activity and efferent sympathetic response to cardiac stress. *Am J Physiol Heart Circ Physiol* 314: H954–H966, 2018. doi:10.1152/ajpheart.00593.2017.
17. **Yoshie K**, **Rajendran PS**, **Massoud L**, **Mistry J**, **Amer Swid M**, **Wu X**, **Sallam T**, **Zhang R**, **Goldhaber JI**, **Salavatian S**, **Ajijola OA.** Cardiac TRPV1 afferent signaling promotes arrhythmogenic ventricular remodeling after myocardial infarction. *JCI Insight* 5: e124477, 2020. doi:10.1172/jci.insight.124477.
18. **Miller JE**, **Ayzenshtat I**, **Carrillo-Reid L**, **Yuste R.** Visual stimuli recruit intrinsically generated cortical ensembles. *Proc Natl Acad Sci USA* 111: E4053–E4061, 2014. doi:10.1073/pnas.1406077111.
19. **Hopkins DA**, **Armour JA.** Localization of sympathetic postganglionic and parasympathetic preganglionic neurons which innervate different regions of the dog heart. *J Comp Neurol* 229: 186–198, 1984. doi:10.1002/cne.902290205.
20. **Armour JA**, **Hopkins DA.** Localization of sympathetic postganglionic neurons of physiologically identified cardiac nerves in the dog. *J Comp Neurol* 202: 169–184, 1981. doi:10.1002/cne.902020204.
21. **Rajendran PS**, **Challis RC**, **Fowlkes CC**, **Hanna P**, **Tompkins JD**, **Jordan MC**, **Hiyari S**, **Gabris-Weber BA**, **Greenbaum A**, **Chan KY**, **Deverman BE**, **Münzberg H**, **Ardell JL**, **Salama G**, **Gradinaru V**, **Shivkumar K.** Identification of peripheral neural circuits that regulate heart rate using optogenetic and viral vector strategies. *Nat Commun* 10: 1944, 2019. doi:10.1038/s41467-019-09770-1.

SUPPLEMENTAL FIGURES

A Novel Metric Linking Stellate Ganglion Neuronal Population Dynamics to Cardiopulmonary Physiology

Koustubh B. Sudarshan[1], Yuichi Hori[2], M. Amer Swid[2], Alexander C. Karavos[1], Christian Wooten[2], J. Andrew Armour[2], Guy Kember[1], and Olujimi A. Ajijola[2,3].

[1]Department of Engineering Mathematics and Internetworking, Dalhousie University, Halifax, Nova Scotia, Canada.

[2]Cardiac Arrhythmia Center and Neurocardiology Research Program, University of California - Los Angeles (UCLA), Los Angeles, CA, USA.

[3]Molecular, Cellular, and Integrative Physiology Interdepartmental Program, University of California - Los Angeles (UCLA), Los Angeles, CA, USA.

Running Head: Cardiopulmonary transduction in stellate ganglia

Word Count:
Disclosures: None

Address for correspondence:

Olujimi A. Ajijola MD PhD
UCLA Cardiac Arrhythmia Center
UCLA Neurocardiology Research Center
David Geffen School of Medicine at UCLA.
100 Medical Plaza, Suite 660, Westwood Blvd
Los Angeles CA 90095-1679
Phone: 310 206 6433 ; Fax: 310 825 2092
e-mail: oajijola@mednet.ucla.edu

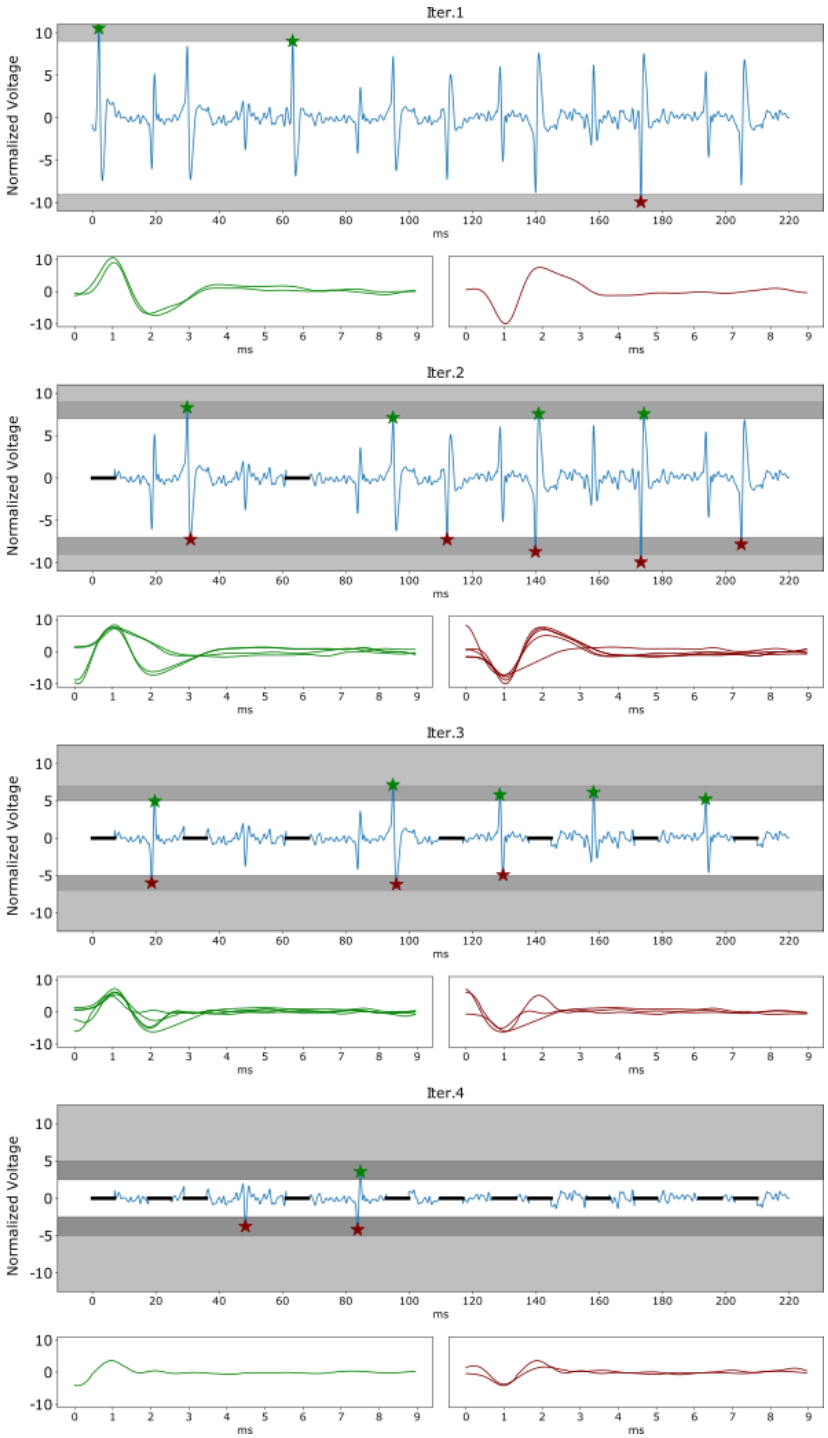

Supplemental Figure 1. Spike Detection Algorithm.
Schematic summary to demonstrating spike identification from extracellular stellate ganglion neural recordings. Iter = Iteration

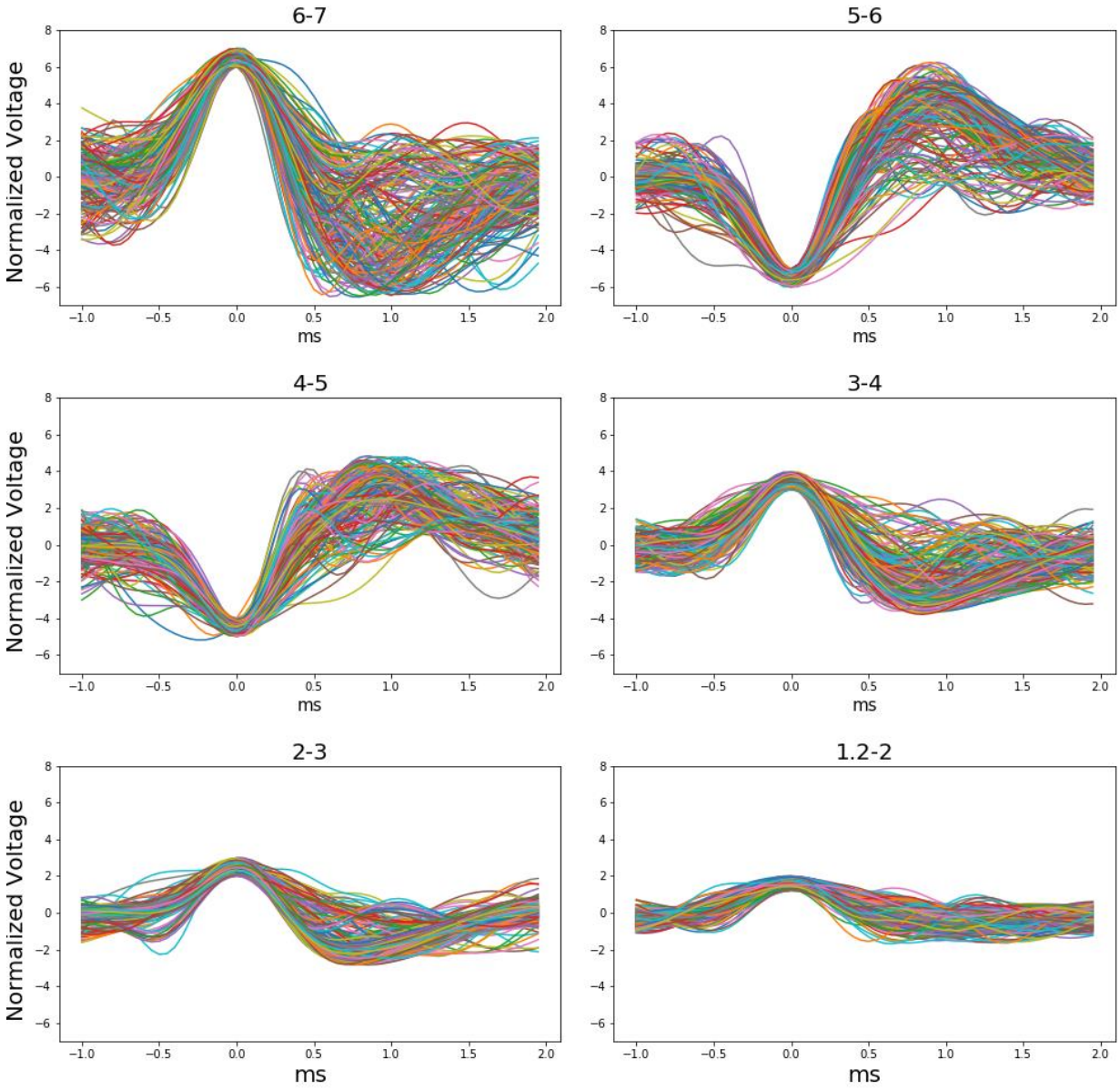

Supplemental Figure 2. Examples of Superimposed Spikes.
Various magnitudes of two hundred spikes with similar peaks superimposed - one millisecond prior and two milliseconds post. All spikes are taken from a single channel demonstrating the softwares spike detection capability.

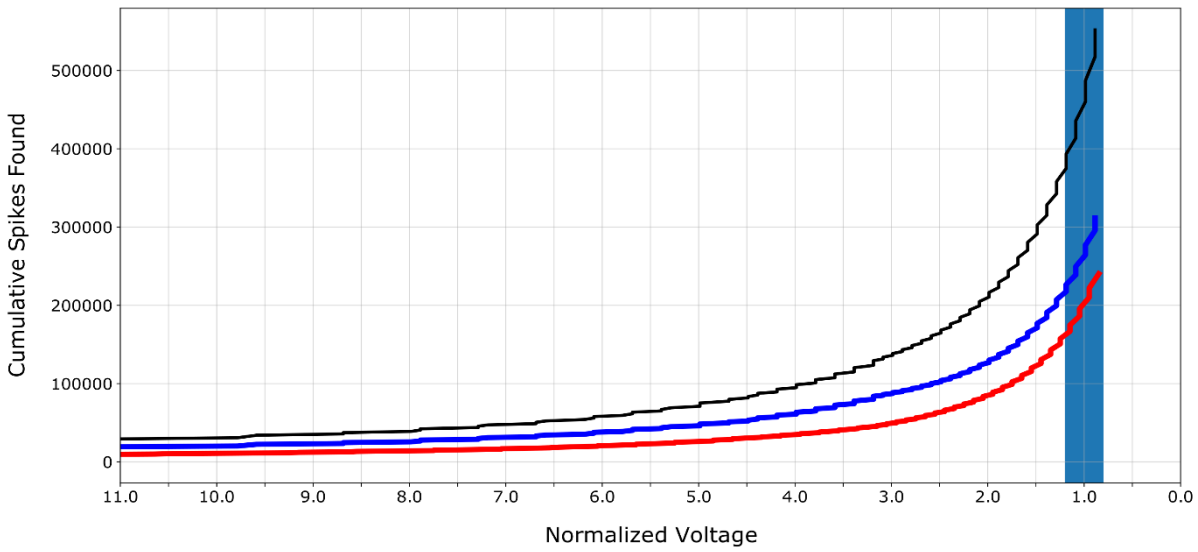

Supplemental Figure 3. Spike Detection as Minimum Level Decreases.
Cumulative positive, negative and total (blue,red,black) spikes found in a channel as the amplitude threshold is lowered. The normalized voltage range 1.2-0.8 is highlighted to show where the noise floor was set. Total spikes found is inversely related to normalized voltage floor, delineated by total spikes found approximately doubling as normalized voltage goes from 4.0 to 2.0

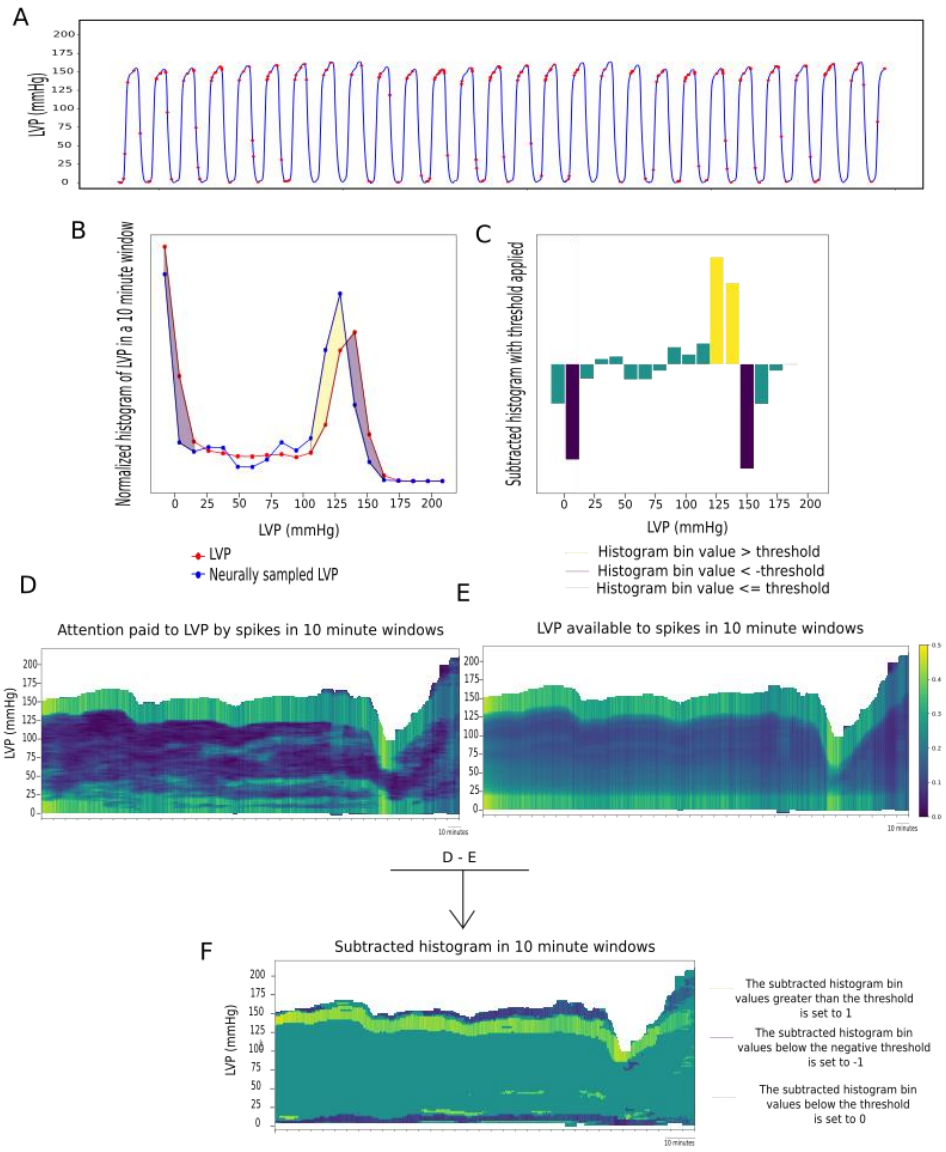

Supplemental Figure 4. Schematic explanation of the phase selectivity metric. A. Left ventricular pressure (LVP) shown over 15 seconds (blue tracings) and neural samples of LVP (red dots). B. Normalized histograms of equally-spaced sampling of LVP (red line), taken from a 10 minute sample, and neural samples of LVP from the same time frame (blue line). C. The two histograms in panel B are subtracted to form a comparison between equally-spaced and neurally-sampled LVP. The subtracted histogram bins exceeding the plus saturation threshold (chosen as >=0.5 here) are colored yellow, those bins exceeding the minus saturation threshold (chosen as <=-0.5 here) are coloured purple, and the balance within the saturation threshold (between -0.5 and 0.5) are colored teal. D. Normalized histogram of neurally-sampled LVP arranged as vertical strips and computed over a 10 minute sliding window for the duration of the experiment. E. Same as Panel D but applied to equally-spaced sampling of LVP. In panels D and E, individual histogram bin values are colored by saturating at an upper threshold of 0.5. E. Subtracted histogram of panels D and E and colored as in C. The colors yellow, teal, and purple qualitatively represent the degree of 'phase selectivity' of neural sampling to LVP relative to a benchmark, the degree of 'phase selectivity' through equally-spaced of LVP. Yellow regions

indicate a relative increase in phase selectivity, the purple regions indicate a relative decrease in phase selectivity, and the teal regions indicate relatively similar phase selectivity.

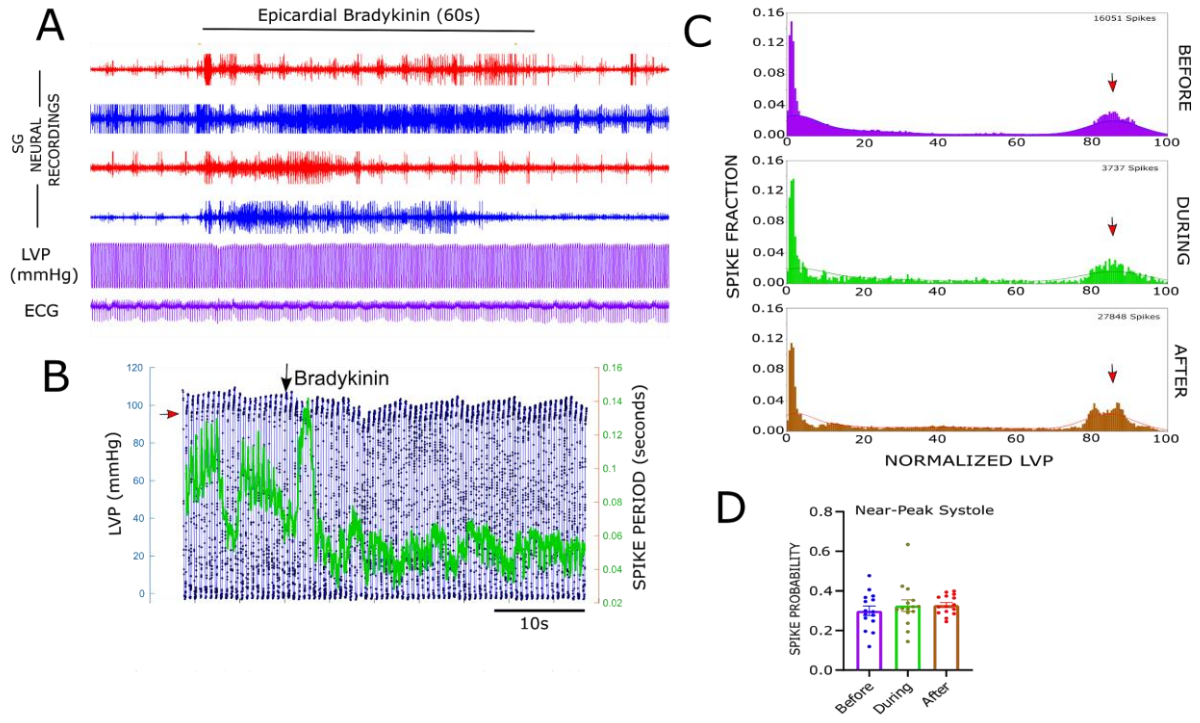

Supplemental figure 5. Chemo-afferent activation does not impact near-peak systolic phase-selectivity.

A. Representative recordings (blue and red tracings) before, during (the 60s period noted in the figure), and after the epicardial application of bradykinin (40ug/ml) along with LVP and ECG tracings. B. Spike periodicity (green tracings) plotted along with LVP(blue tracings) with individual spikes represented as black dots. Bradykinin increased spiking activity (and decreased spike period). C. Spike fraction is plotted for normalized LVP 5 minutes before (blue), during (green) and after (red) the application of bradykinin with the kd-kernel estimated spike fraction distribution superimposed This shows no difference in the near-peak systolic phase selectivity (red arrow) of spikes before, during, or after bradykinin application. D. Mean and standard error plot of the spiking probability for 16 channels in a subject.

Chapter 4

ANALYSIS OF STELLATE POPULATIONS IN HEART FAILURE ANIMALS

Contribution of the student :

The candidate was a primary contributor to the coactivity matrix, entropy metric, hypothesis formation based on developed metrics, data analysis, interpreted results of experiments, figure preparation, manuscript drafting, editing and revision of manuscript along with Dr. Nil Gurel.

Metrics of High Cofluctuation and Entropy to Describe Control of Cardiac Function in the Stellate Ganglion

Nil Z. Gurel[1*,†], Koustubh B. Sudarshan[3,†], Joseph Hadaya[1,2], Alex Karavos[3], Taro Temma[1], Yuichi Hori[1], J. Andrew Armour[1], Guy Kember[3], Olujimi A. Ajijola[1,2]

***For correspondence:** nil@ucla.edu (FMS)

[†]These authors contributed equally to this work

[1] UCLA Cardiac Arrhythmia Center and UCLA Neurocardiology Research Program of Excellence, Los Angeles, CA; [2]UCLA Molecular, Cellular, and Integrative Physiology Program, Los Angeles, CA; [3]Department of Engineering Mathematics and Internetworking, Dalhousie University, Nova Scotia, Canada

Abstract Stellate ganglia within the intrathoracic cardiac control system receive and integrate central, peripheral, and cardiopulmonary information to produce postganglionic cardiac sympathetic inputs. Pathological anatomical and structural remodeling occurs within the neurons of the stellate ganglion (SG) in the setting of heart failure. A large proportion of SG neurons function as interneurons whose networking capabilities are largely unknown. Current therapies are limited to targeting sympathetic activity at the cardiac level or surgical interventions such as stellectomy, to treat heart failure. Future therapies that target the stellate ganglion will require understanding of their networking capabilities to modify any pathological remodeling. We observe SG networking by examining cofluctuation and specificity of SG networked activity to cardiac cycle phases. We investigate network processing of cardiopulmonary transduction by SG neuronal populations in porcine with chronic pacing-induced heart failure and control subjects during extended in-vivo extracellular microelectrode recordings. We find that information processing and cardiac control in chronic heart failure by the SG, relative to controls, exhibits: i) more frequent, short-lived, high magnitude cofluctuations, ii) greater variation in neural specificity to cardiac cycles, and iii) neural network activity and cardiac control linkage that depends on disease state and cofluctuation magnitude.

Introduction

Neural control of cardiac function involves adaptive adjustment of mechanical and electrical activity to meet the organism's demand for blood flow. This cardioneural control scheme consists of neural populations in the central, peripheral, and intrinsic cardiac nervous systems. Interactions among components of the cardiac nervous system highlight that these neural populations work in concert, rather than as independent, singular processing units (***Ardell et al., 2016***). From an information processing standpoint, the operation of these interconnected neural networks has evolved to coordinate cardiac function on a beat-by-beat basis, producing the "functional" outputs of this control scheme such as blood pressure, heart rate, or respiratory pressure and rate. Localized adaptations in the cardioneural network in response to pathology can cause an evolution of global network properties with heightened risk of poor outcomes without measurable evidence

from these functional outputs (***Deyell et al., 2015***; ***Kember et al., 2013***).

There is a current focus on understanding cardioneural network processing within the stellate ganglion (SG), a collection of nerves serving as the major source of sympathetic input to the heart(***Mehra et al., 2022***). The SG (located in either side of the neck) operates as an integrative layer within the control hierarchy where it processes central cardiac inputs to the heart, receives cardiac feedback, and projects efferent control outputs to the heart. In pathological states such as heart failure (HF), morphological and neurochemical remodeling of SG neurons has been reported in both animal models (***Ajijola et al., 2013***; ***Han et al., 2012***; ***Ajijola et al., 2015***; ***Nakamura et al., 2016***) and in humans (***Ajijola et al., 2020***, ***2012b***). Due to its key role in proarrhythmic neural signaling and convenience in surgical accessibility, clinical interventions targeting SG are used to treat various cardiovascular conditions (***Vaseghi et al., 2012***, ***2017***; ***Ajijola et al., 2012a***). It has also been established that an enhanced cardiac sympathetic afferent reflex contributes to sympathoexcitation and pathogenesis of heart failure (***Wang and Zucker, 1996***; ***Ma et al., 1997***; ***Chen et al., 2015***; ***Wang et al., 2017***, ***2008***, ***2014***; ***Gao et al., 2005***, ***2007***). Despite these novel interventions and general understanding, SG clinical therapy will remain largely unexplored without greatly improved understanding of SG neuronal information processing in healthy versus pathological states. Prior studies examining the SG neural activity have been limited to in vivo extracellular recordings (***Armour, 1983***, ***1986***; ***Armour et al., 1998***; ***Yoshie et al., 2020***, ***2018***).

Recently, we explored network processing of cardiopulmonary transduction by SG neuronal populations in healthy porcine, defining a novel metric 'neural specificity' that measures specificity of neural firing patterns to cardiopulmonary signals (***Sudarshan et al., 2021***). This metric is contrastive and a measure of the difference between the probability density function (PDF) of neural 'sampling' of a control target relative to the same in the random sampling limit. While the target, left ventricular pressure (LVP) considered here is periodic this is not a necessary condition for use of the specificity metric; it is also applicable to aperiodic signals in an event-based fashion.

In the current work, we investigate differences in information transfer between control and heart failure porcine models with multi-channel electrode arrays. We first uncover network-level spatiotemporal dynamic signatures by quantifying short-lived high cofluctuation events in neural activity. Second, we study coherence and consistency in the evolution of neural specificity with respect to the control target. Third, we expose differences in neural specificity and its coherence and consistency, via entropy, inside and outside cofluctuation events. These differences are considered for control and heart failure models and quantify differences in the maintenance of function between these groups.

Methods

Animal Experiments

Fig. 1 presents the conceptual overview and study design. The study was performed under a protocol approved by the University of California Los Angeles (UCLA) Animal Research Committee (ARC), in compliance with the UCLA Institutional Animal Care and Use Committee (IACUC) guidelines and the National Institutes of Health (NIH) Guide for the Care and Use of Laboratory Animals. Fig. 1D-E summarizes the studied animal groups and experimental pipeline. Male Yorkshire pigs $(n = 17)$ weighing $57.5 \pm 12kg$ $(mean \pm SD)$ were studied as control $(n = 6)$ and HF model $(n = 11)$ groups. For SG neural data collection, the animals were sedated with tiletamine and zolazepam (Telazol, 4-8mg/kg) intramuscularly, intubated, and maintained under general anesthesia with inhaled isoflurane (2%). Continuous intravenous saline $(8 - 10ml/kg/h)$ was infused throughout the protocol and animals were temperature maintained using heated water blankets $(37^oC - 38^oC)$.

Median sternotomy by an incision down the midline of the entire sternum was performed to have a wide view of the thoracic region (Fig. 1A). The pericardium was opened to expose the heart and both stellate ganglia. After surgical procedures, animals were transitioned to alpha-chloralose anesthesia ($6.25mg/125mL$; $1mL/kg$ for bolus, $20 - 35mL/kg$ or titrated to effect for maintenance)

with supplemental oxygen ($2L/minute$) for in vivo neural recordings from the left stellate ganglion. The left carotid artery was exposed, and a pressure catheter (SPR350, Millar Inc., Houston, TX) was inserted to continuously monitor left ventricular pressure (LVP). Additionally, three-lead surface electrocardiogram (ECG) and respiratory pressure (RP) were monitored continuously, and sampled at $1kHz$. Arterial blood gas contents were monitored at least hourly to ensure appropriate experimental conditions. At the end of the protocol, animals were euthanized under deep sedation of isoflurane and cardiac fibrillation was induced.

The heart failure model was created with implanted pacemakers (Viva Cardiac Resynchronization Therapy–Pacemaker, Biotronik, Lake Oswego, OR), as previously described (***Hori et al., 2021***), and summarized in Fig. 1D. After implantation, animals had a recovery period of 48 hours and chronic bigeminy pacing was initiated from the right ventricle. This process produces premature ventricular contractions (PVCs) which lead to cardiomyopathy, also known as PVC-induced cardiomyopathy (***Blaye-Felice et al., 2016***). To confirm the progression of cardiomyopathy, echocardiography was performed, before and after implantation. After the animals have been confirmed to have cardiomyopathy (referred as HF animals) at eight weeks after implantation, surgical procedures described in Fig. 1E were performed, and extracellular recordings were obtained from the left stellate ganglion, shown in Fig. 1A. It should be noted that a subset of HF animals ($n = 6$) underwent an intervention, epicardial application of resiniferatoxin (RTX) to study its effects on the progression of cardiomyopathy as a separate study. However no significant effect of RTX was noted in any of the echocardiographic, serum, physiological, and autonomic tests (***Hori et al., 2021***). Hence, in this work, we combined RTX-treated HF animals with untreated HF animals.

We confirmed the RTX depleted the afferents by analyzing both structural and functional data. Structural depletion was proven with immunohistochemistry studies of the left ventricle (LV) and T1 dorsal root ganglion (DRG). Calcitonin gene-related peptide (CGRP)-immunoreactive fibers, a marker of sensory afferent nerves, was significantly reduced within the nerve bundles located in the LV for the RTX-treated group. Furthermore, the depletion of cardiac transient receptor potential vanilloid-1(TRPV1) afferents was confirmed by the significant reduction of CGRP-expressing neurons in DRG. Functional depletion was proven by the response to the agonist of TRPV1 channel bradykinin and capsaicin. The RTX-treated group had a significantly lower LV pressure (LVP) response in the application of bradykinin and capsaicin, indicating that elimination of cardiac sympathetic afferent reflex was accomplished by RTX application in each case.

SG Neural Recordings and Experimental Protocol

For each animal, a 16-channel, linear, single shank microelectrode array (LMA, Microprobes, Gaithersburg, MD) was inserted in the craniomedial pole of the left stellate ganglion (Fig. 1A). The LMA consisted of a polyimide tube of $0mm$ that contains recording sites, and a stainless steel tip of $1mm$ (Fig. 1B). Polyimide tube hosted a total of 16 platinum-iridium recording sites with $25\mu m$ radius, separated by $500\mu m$ intra-electrode spacing. A microelectrode amplifier (Model 3600, A-M Systems, Carlsborg, WA) was used to amplify (gain of $1000 - 2500$) and filter ($300Hz - 3kHz$ band-pass filter) the acquired signals. The signals were transferred to a data acquisition platform (Power 1401, Cambridge Electronic Design, Cambridge, UK) and recorded using Spike2 software (Cambridge Electronic Design, Cambridge, UK). All data were processed in Python and MATLAB. Increases in spike rate occur within 90-minutes of electrode insertion, hence a stabilization time of approximately three hours is required after the insertion takes place (***Sudarshan et al., 2021***).

It should be noted that our study deals with multi-electrode recordings of the closest neural populations to the electrode array. The earliest fundamental studies probing into cardiac nervous system used single-unit recordings, for which the target neurons should be isolated and appropriate low-impedance conductors should be used for obtaining high quality neural signals. Unlike these early studies, we used multi-unit (16-channel) electrode arrays to monitor the ensemble behaviors of SG neural populations. This experimental shift from single-unit to multi-unit recording has gained interest in the recent years in neurocardiology and neuroscience communities, offering

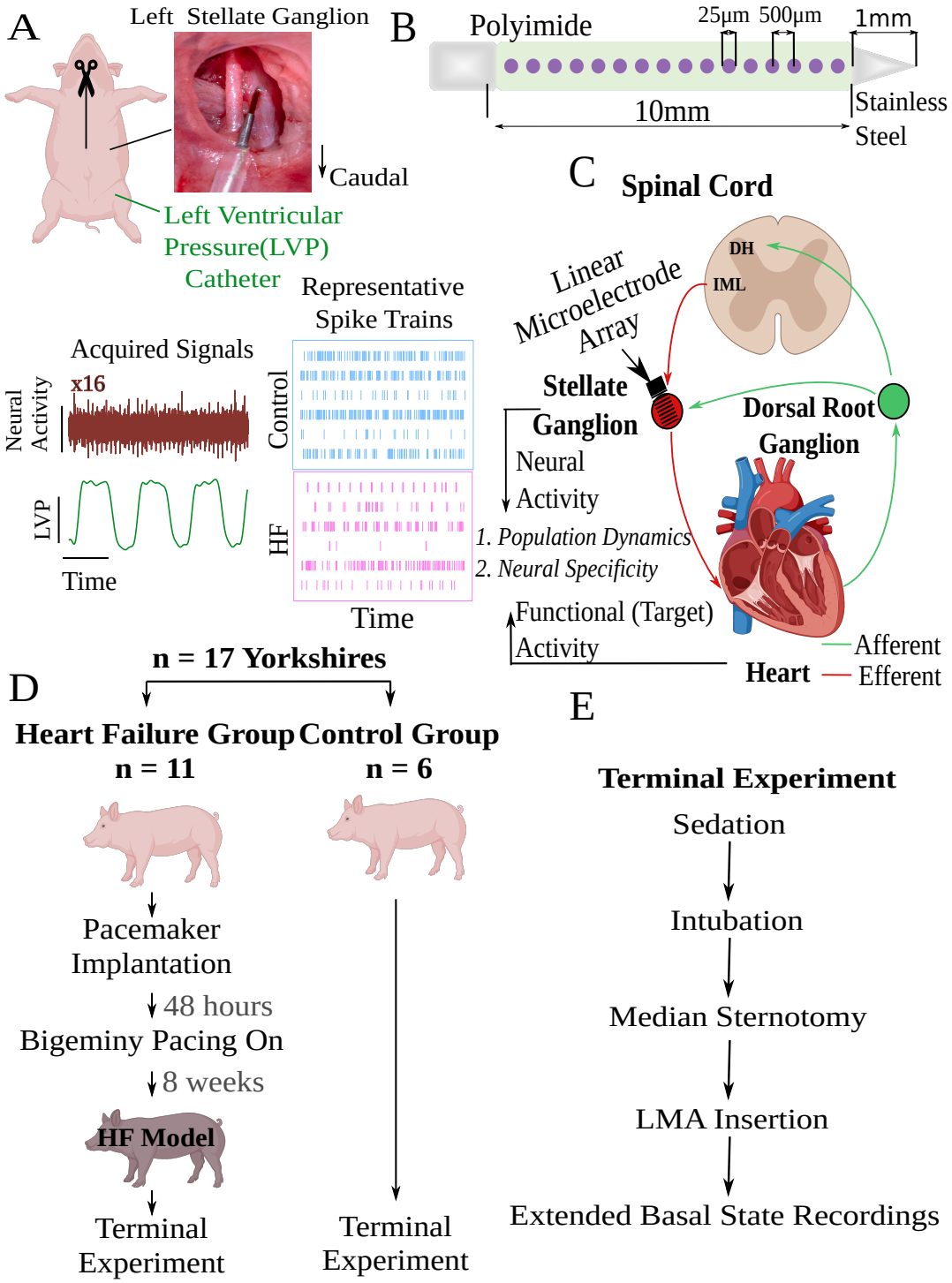

Figure 1. Experimental workflow and overall concept. A) A linear microelectrode array (LMA) was inserted to the left stellate ganglion (SG) for each animal. A total of 16 channels of neural activity were collected along with simultaneous left ventricular pressure (LVP). Representative spike trains are displayed for each animal group. B) Specifications of the LMA. C) Conceptual representation of this work. SG receives efferent and afferent information from the spinal cord's intermediolateral complex (IML) and dorsal root ganglion, respectively, and transmits efferent information to the heart. In this work, we investigate neural activity and its relationship to cardiac function as represented by a control target such as LVP. D) Among 17 Yorkshire pigs, 11 had heart failure induced by ventricular pacing, and 6 were in control group. SG recordings were collected at terminal experiments for both groups. E) Experimental flow descripting the surgical preparation for the recordings. DH: Dorsal horn.

an experimental view to the ensemble behaviors of neural populations (***Gurel et al., 2022***).

Data Availability

Data is available in the Dryad repository
https://datadryad.org/stash/share/nEzGj21D1bUvrBYEtSNATZSAYTW39cBjjmV5RuVveLY

Signal Processing and Time Series Analysis

Signal Processing Pipeline

A high-level description of the signal processing pipeline is in Fig. 2. In summary, Pearson's cross correlation is used to construct the coactivity matrix as the collection of cross correlations between all possible channel pairs. The coactivity matrix is computed at each timestamp and associated with a window of past neural activity (Fig. 2, 'Coactivity' block). This computation yields a causal sliding window of coactivity matrices referred to as the 'coactivity time series'.

Discrete events of high cofluctuation occurring in the coactivity time series are defined using two thresholds: (i) the coactivity time series is mapped to a univariate 'cofluctuation time series' where, at each timestamp, the percentage of coactivity matrix members exceeding a threshold C is found, and (ii) discrete 'events' are defined as those timestamps when up-crossings of the cofluctuation time series through a second threshold T occur. The method used to choose the (C, T) pair, detailed in this section, generates discrete event timestamps and allows for the computation of the event rate (ER) mean and standard deviation (STD) statistics, which are used later in the statistical analyses. These cofluctuation events are regions that expose shifts in neural processing within the SG. These events are linked to function through the consideration of how neural specificity differs inside and outside cofluctuation events in control and heart failure animals.

The relationship between a control target such as LVP and neural activity at each channel is quantified via a continuously varying neural specificity (***Sudarshan et al., 2021***) (Fig. 2, 'Neural Specificity' block). The neural specificity is contrastive since it is the difference between the PDF of neural sampling of a target and the same found from random sampling. The neural activity in the SG is known to be a mixture of afferent, efferent, and local circuit activity derived from local circuit neurons with inputs from multiple sources. It in this sense that we define neural computation; when we observe the specificity to the target operating above or below the random sampling limit. Neural specificity is a multivariate signal measured across multiple target states at each channel as a function of time. This is reduced, for each channel, to a univariate time series by constructing its coherence in terms of entropy. The evolution of coherence in time provides access to the dynamics or consistency of neural computation. Detailed information about each signal processing step is provided in this section. The supplementary section contains material detailing the mathematical aspects of the analysis. As stated in the signal processing block diagram, our outcome measures are event rate, entropy, event entropy. These metrics are developed in the Supplementary Material 1.

Unsupervised Spike Detection

We use a competitive, adaptive threshold, unsupervised approach for neural spike detection (***Sudarshan et al., 2021***). The algorithm initializes plus and minus barriers at the plus or minus signal maximum amplitude. The barriers are respectively lowered or raised until the plus or minus barrier 'wins the competition' and is the first to yield a minimal number of crossings. Detected spike regions are masked as a zero signal and the process repeated with barrier sizes further reduced in subsequent iterations. The competition is halted when one barrier is first to reach a minimal barrier height.

Code Availability

Supporting Apache License codes are at GitHub (https://github.com/Koustubh2111/Cofluctuation-and-Entropy-Code-Data).

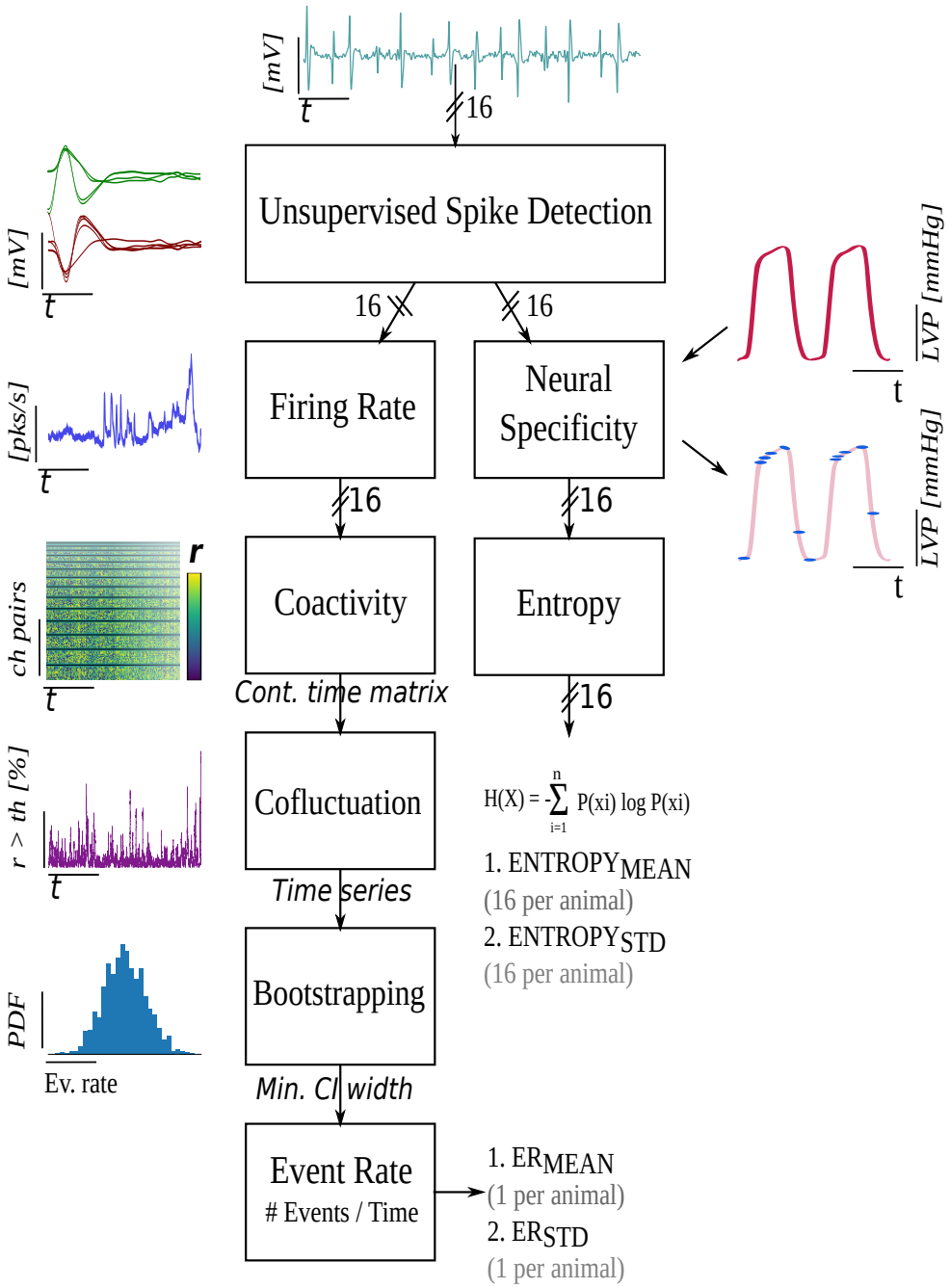

Figure 2. Signal Processing Block Diagram.

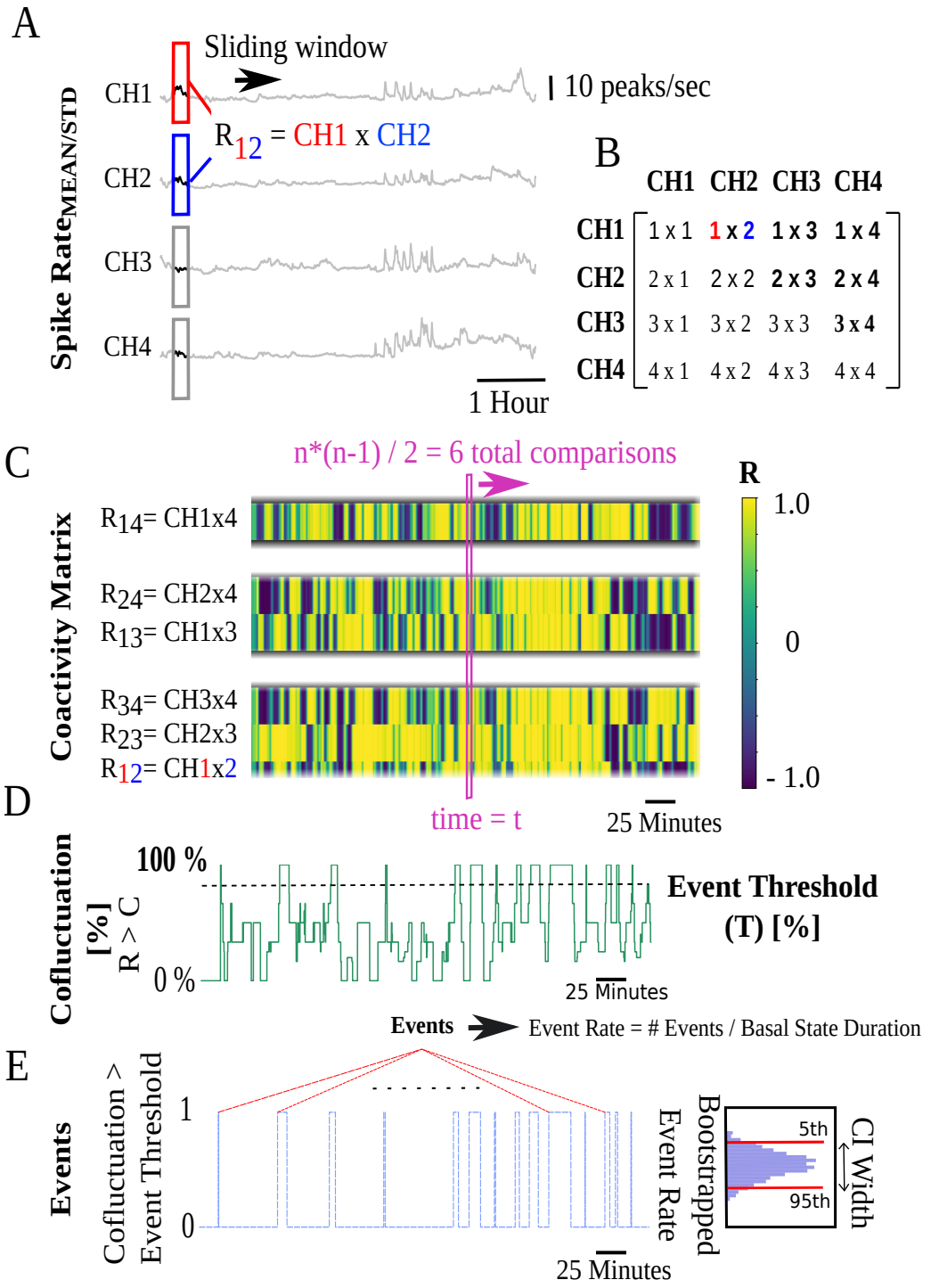

Figure 3. Coactivity matrix and event rate (ER) computation pipeline illustrated for 4-channels. A) Pearson's cross correlation coefficients (R) of pairwise sliding spike rate windows for 4 channels. B) R values for cross correlation of 'i' and 'j' channels are stored in the 'i' and 'j' positions of a $4x4$ matrix at each timestamp. C) Coactivity matrix super-diagonals at each timestamp are vertically stacked. At each timestamp t, $n(n-1)/2 = 6$ unique cross-correlations are possible corresponding to super-diagonals with 3, 2, and 1 members. The y-axis begins at the bottom with the 3 members of the first super-diagonal followed by subsequent super-diagonals. Colors represent the R value. D) Cofluctuation time series are the percentage of Pearson's R values at each timestamp that exceed a cofluctuation threshold (C). E) Discrete events correspond to time intervals when cofluctuations show an up/down crossing through an event threshold (T).

Dataset and Statistical Analysis

Statistical analyses are performed in MATLAB Statistics & Machine Learning Toolbox (version R2021a) and Python SciPy Library (version 3.8.5).

Sample Size Breakdown

Two channels were excluded from two animals due to insufficient signal quality. Within event rate analyses, all animals had sufficient neural data ($n = 17$ animals, 6 control, 11 HF). Entropy analyses for 3 HF animals were excluded due to insufficient LVP quality resulting in $n = 14$ animals (6 control, 8 HF).

Outcome Measures

Within the signal processing pipeline described in Fig. 3, the event rate measures, ER_{MEAN} and ER_{STD}, are used to summarize the cofluctuation time series for each animal. A mean and standard deviation of the 16 channel-wise entropy time series results in 32 measures of entropy per animal (16 for $Entropy_{MEAN}$ and 16 for $Entropy_{STD}$ per animal).

Statistical Analysis

For variables that result in a single number per animal (such as ER_{MEAN} and ER_{STD}, Fig. 4A-B), independent samples t-tests or Wilcoxon rank-sum tests are respectively used for normal or non-normal data (normality assessed by Shapiro-Wilk) to quantify differences between animal groups.

For variables that have multiple variates per animal (such as $Entropy_{MEAN}$ calculated from multiple channels, Fig. 4C-D), mixed effects models are constructed in the MATLAB Statistics and Machine Learning Toolbox (***Pinheiro and Bates, 1996***; ***MATLAB, 2021***). $Entropy_{MEAN}$ and similarly $Entropy_{STD}$ (not shown) and $Entropy_{MEAN,EVENT}$ and similarly $Entropy_{STD,EVENT}$ (not shown) are modelled via mixed effects as, $1|$ indicates random effects,

$$Entropy_{MEAN} = Animal\ Type + (1|channel) + (1|animal\ ID) \quad (1)$$

$$Entropy_{MEAN,EVENT} = Event\ Type + Animal\ Type + CoactivityType + (1|channel) + (1|animal\ ID) + (1|Entropy_{MEAN}) \quad (2)$$

In Eq. (2), and depicted in Fig. 4C-D, the computed metric $Entropy_{MEAN}$ is the outcome variable; the animal type $(control/HF)$ a fixed effect; and the channel number $(1-16)$ and the $animal\ ID$ random effects. The analysis of $Entropy_{STD}$ follows by replacing 'MEAN' with 'STD'.

In Eq. (2) the model $Entropy_{MEAN,EVENT}$ is shown and refers to entropy mean data within event regions where the model for mean entropy data outside event regions is $Entropy_{MEAN,NON-EVENT}$. In this way, models are constructed for event / non-event, mean / std entropy as the outcome variable; the event type (event / non-event), the animal type (control / HF), and coactivity computation type (mean / std) are fixed effects; and channel number, animal ID, and entropy (type matching the outcome entropy's type, mean or std) are random effects.

For all analyses using mixed effects modeling, the β coefficients (fixed effects estimates), p-values, effect sizes (d_{RM} based on repeated measures Cohen's d_{RM}, (***Lakens, 2013***)), 95% confidence intervals (CI) of β coefficients (lower, upper bounds) are reported in results in (β, $\pm CI$, d_{RM}, p) format. The β coefficients indicate the adjusted differences (units matching the outcome variable's unit) in one group compared to the other. For analyses with independent samples, p-values and independent samples effect sizes (d, based on Cohen's d) are reported in (p, d) format. For all analyses, a two-sided $p < 0.05$ denoted statistical significance.

Results

Neural activity was measured over 16 channels along with simultaneous left ventricular pressure (LVP) for approximately six hours of continuous recordings per animal. Representative neural activity recording for a single channel, LVP, and representative spike trains are displayed for control

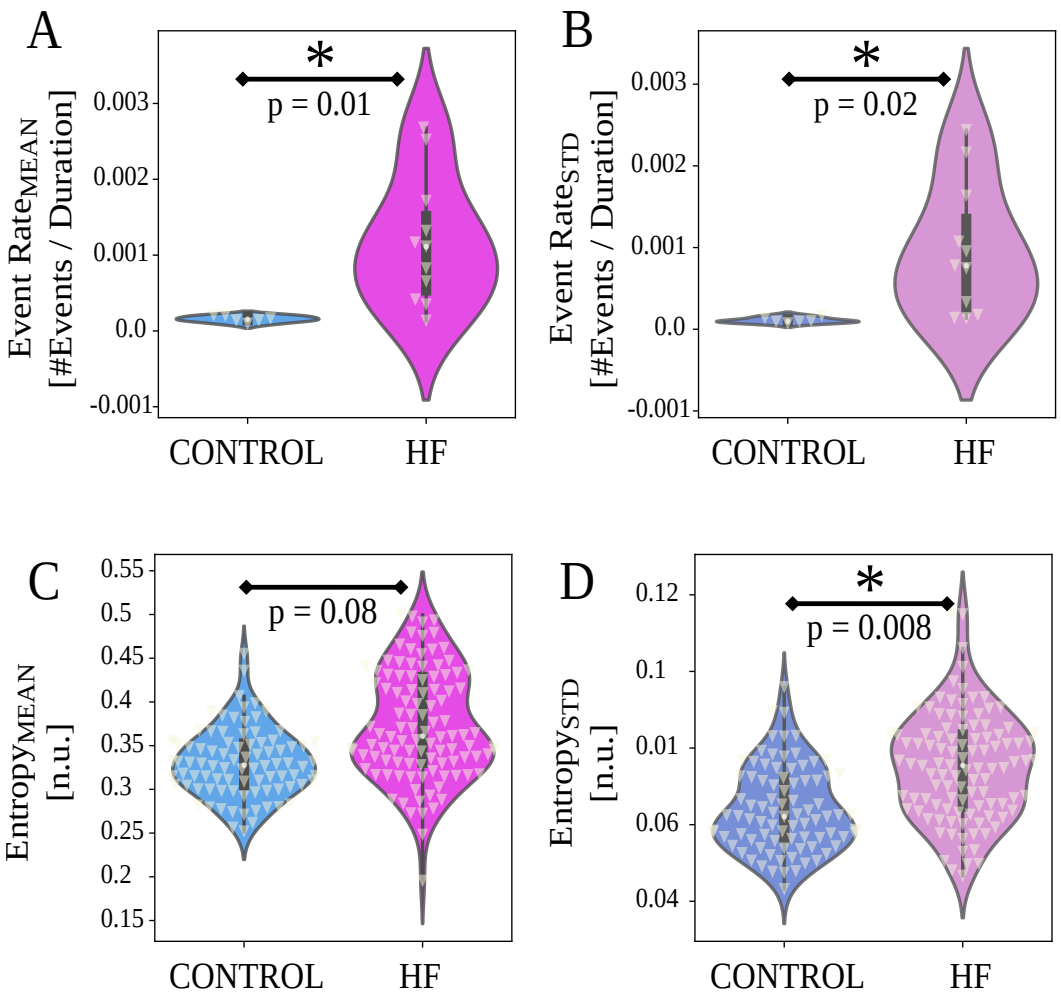

Figure 4. Event rate (ER) and entropy results between control and HF animals (horizontal axes). White triangles indicate data points. A-B) Heart failure (HF) group animals show higher ER_{MEAN} and ER_{STD} compared to control group ($p < 0.05$). C-D) HF group animals show higher entropy variability ($Entropy_{STD}$, Eq. (2), $p = 0.008$, in D), and no difference in $Entropy_{MEAN}$ (Eq. (2), $p = 0.08$, in C). For ER, p-values are from two-sample t-test or Wilcoxon rank-sum tests, depending on normality. For entropy, p-values are from linear mixed effects (LME, Eq. (2)) detailed in Methods.

and heart failure animals in Fig. 1A. A total of 17 Yorkshires (6 control, 11 HF, Fig. 1D) underwent the terminal experiment described in Fig. 1E. Upon the signal processing pipeline described above, we computed two event rate measures per animal as the final product representing the cofluctuations (ER_{MEAN}, ER_{STD}). As the metric representing the neural specificity, we computed two entropy measures per channel ($Entropy_{MEAN}$, $Entropy_{STD}$), resulting in a total of sixteen $Entropy_{MEAN}$ and sixteen $Entropy_{STD}$ per animal. Finally, we used these metrics to quantify: i) neural population dynamics (i.e., ER_{MEAN}, ER_{STD}), ii) neural specificity to target LVP, or cardiac control (i.e., $Entropy_{MEAN}$, $Entropy_{STD}$), and iii) Linkage between neural population dynamics and specificity (i.e., $Entropy_{MEAN,EVENT}$, $Entropy_{STD,EVENT}$).

Stellate Ganglion in Heart Failure Exhibits High Event Rate

Fig. 4A-B show event rate outcomes grouped by heart failure (HF) models and controls. HF animals show significantly higher event rates compared to control animals for both ER_{MEAN} ($p = 0.011$, effect size $d = 1.59$) and ER_{STD} ($p = 0.023$, $d = 1.48$). The cofluctuation time series for each animal is depicted in Fig. 6, where the event time series are computed. The 'events' or short-lived intervals where high cofluctuations exist are shown as level 1, leading to the event time series in Fig. 7. We observe that the cofluctuations are more localized in HF animals with greater heterogeneity.

HF Animal Models Have Heavy Tailed Cofluctuation Distributions

We qualitatively explored the statistical distribution of the cofluctuation time series. Fig. 5 shows log-normal fits for each animal group for $Cofluctuation_{MEAN}$ and $Cofluctuation_{STD}$ time series, along with 68% confidence interval (CI) bounds, mean of fit (μ_{FIT}) and standard deviation of fit (σ_{FIT}). Control animals (Fig. 5A-B) exhibit narrow confidence intervals, lower (μ_{FIT}) and (σ_{FIT}) values, and tighter log-normal fits. In contrast, HF animals (Fig. 5C-D) exhibit wider confidence intervals, higher (μ_{FIT}) and (σ_{FIT}) values, and poorer log-normal fits. Of note, HF animals have heavy tails ranging further outside of confidence bounds.

Stellate Ganglion Shows Greater Variation in Neural Specificity to LVP in Heart Failure

We next examined the neural specificity to LVP, quantified by entropy measures in Eq. (2). Fig. 4C-D shows $Entropy_{MEAN}$ and $Entropy_{STD}$, grouped by animals. Compared to the control group, stellate ganglion of HF animals exhibited significantly higher $Entropy_{STD}$ (variation in entropy, Fig. 4D, adjusted $\beta = 0.01$ n.u., 95% $CI = \pm 0.01$ n.u., $d_{RM} = 0.73$, $p = 0.009$). However, there is no significant difference in $Entropy_{MEAN}$ (mean entropy) between animal groups. (Fig. 4C, $\beta = 0.04$ n.u., ± 0.05 n.u., $d_{RM} = 0.82$, $p = 0.087$).

Neural Network Activity and Cardiac Control Linkage Depends on Animal Group and Cofluctuation Magnitude

We explored the nature of cardiac control inside and outside short duration regions of high cofluctuation, i.e. 'events', characterized by strongly coherent stellate neural activity patterns. Insight into how these events may be relevant to cardiac control is considered here in the context of how control differs inside and outside events and termed 'event entropy'.

First, we studied the extent to which event entropy differs inside and outside of events (Fig. 8A, C, event type as fixed effect in Eq. (9)). Second, we studied whether event entropy is sensitive to the animal type characterized here as control or HF (Fig. 8B, D, animal type as fixed effect in Eq. (9)).

Regardless of the animal group,

$Entropy_{MEAN,NON-EVENT}$ significantly exceeds $Entropy_{MEAN,EVENT}$ (Fig. 8A, $\beta = 0.007$ n.u., ± 0.004 n.u., $d_{RM} = 0.07$, $p < 0.001$). Similarly, $Entropy_{STD,NON-EVENT}$ significantly exceeds $Entropy_{STD,EVENT}$ (Fig. 8C, $\beta = 0.01$ n.u., ± 0.002 n.u., $d_{RM} = 0.29$, $p < 0.001$). An examination of the contribution of each animal group showed no significant difference between groups for $Entropy_{MEAN,EVENT}$ (Fig. 8B,

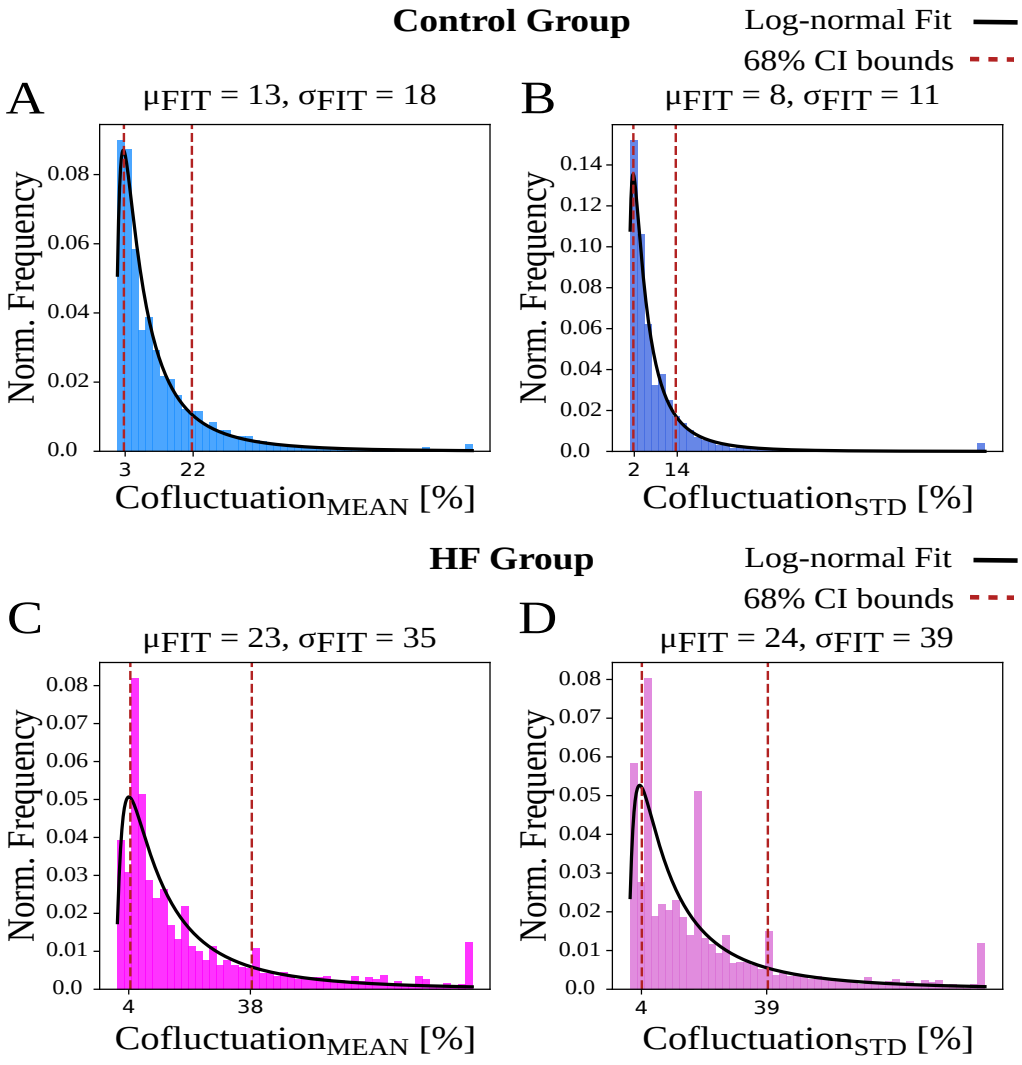

Figure 5. Cofluctuation histograms (calculated from mean or standard deviation of sliding spike rate, referred as $Cofluctuation_{MEAN}$ and $Cofluctuation_{STD}$, respectively) and log-normal fits for each animal group. μ_{FIT} and σ_{FIT} are the respective mean and standard deviation (STD) of fitted distribution, used for 68% confidence interval bounds. A-B) Control animals have narrower bounds and represent a better fit to log-normal distribution. C-D) Heart failure (HF) animals display more heavily skewed distributions that indicate heavy tails.

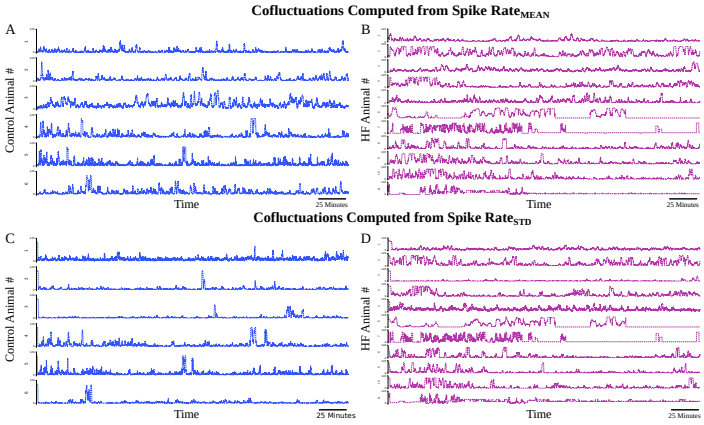

Figure 6. Cofluctuations time series at convergent C values for each animal. A) Cofluctuations from coactivity calculation from mean of sliding spike rate for control animals. B) Cofluctuations from coactivity calculation from mean of sliding spike rate for HF animals. C) Cofluctuations from coactivity calculation from standard deviation of sliding spike rate for control animals. D) Cofluctuations from coactivity calculation from standard deviation of sliding spike rate for HF animals.

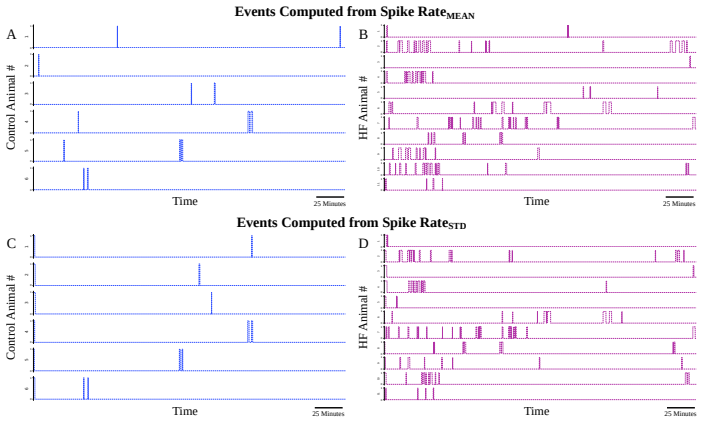

Figure 7. Events time series at convergent (C, T) pairs for each animal. A) Events from coactivity calculation from mean of sliding spike rate for control animals. B) Events from coactivity calculation from mean of sliding spike rate for HF animals. C) Events from coactivity calculation from standard deviation of sliding spike rate for control animals. D) Events from coactivity calculation from standard deviation of sliding spike rate for HF animals.

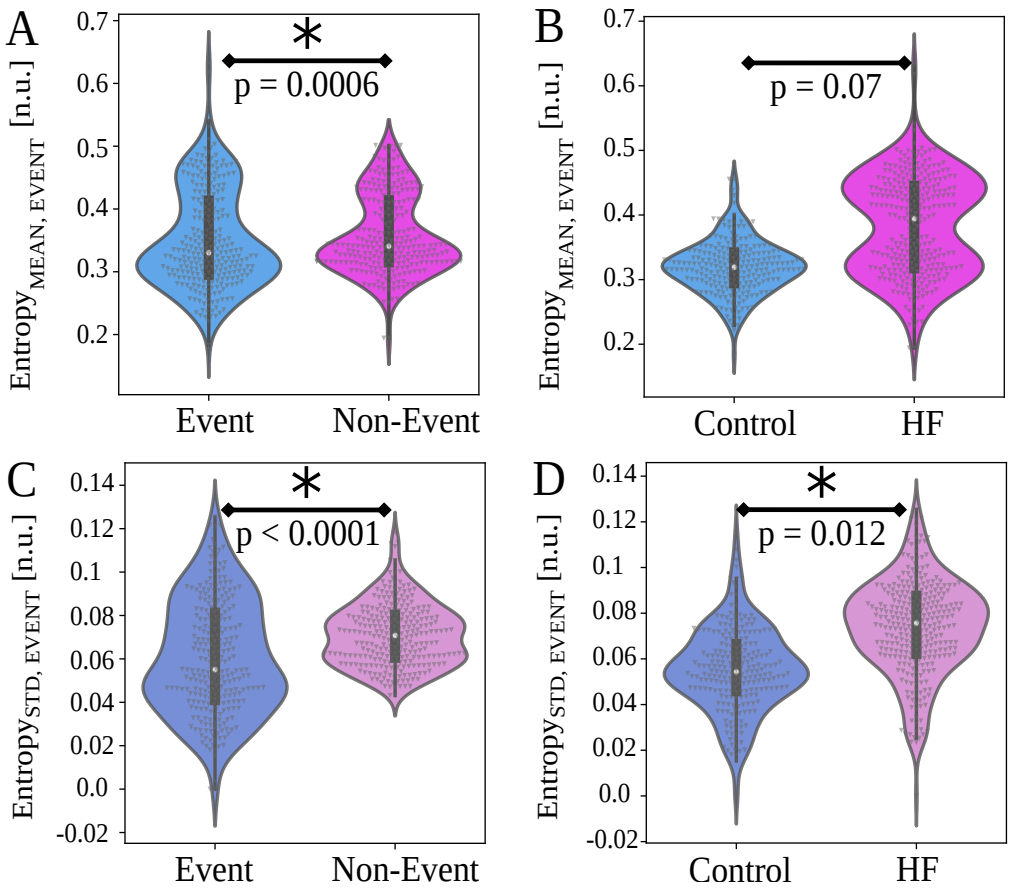

Figure 8. Event entropy Eq. (2) investigation involved consideration of entropy values inside and outside of event regions. A) There is significant difference between in $Entropy_{MEAN,EVENT}$ and $Entropy_{STD,EVENT}$ across all animals ($p = 0.0006$). B) There is no significant difference in $Entropy_{MEAN,EVENT}$ between animal groups ($p = 0.07$). C) There is significant difference in $Entropy_{STD,EVENT}$ between events and non-events across all animals ($p < 0.0001$). D) There is significant difference in $Entropy_{STD,EVENT}$ between animal groups ($p < 0.012$).

$\beta = 0.06$ n.u., ± 0.05 n.u., $d_{RM} = 1.13$, $p = 0.07$). On the other hand, HF animals exhibited an increase in $Entropy_{STD,EVENT}$ compared to control animals (Fig. 8D, $\beta = 0.02$ n.u., ± 0.02 n.u., $d_{RM} = 0.75$, $p = 0.012$). These analyses imply that the linkage between neural network function and cardiac control differs inside and outside of cofluctuation events and between animal groups in the stellate ganglion.

Discussion

In this work, we performed a novel investigation of SG neural population dynamics and neural specificity to continuous left ventricular pressure in control and heart failure Yorkshire pigs. The methods in this work are intended to measure the way population neural activity relates to closed-loop control of a target and how that computation changes in diseased states. This was applied here to closed-loop control of cardiac output where the assumed target was LVP.

The methods in this work involved

- *Neural Specificity* A measure of bias in neural activity toward 'sampling' of specific target states. The target specificity is a contrastive measure that compares neural sampling of a target relative to random sampling of the same target.
- *Neural Specificity Coherence* Entropy of neural specificity was used to measure coherence of neural specificity as a function of time.
- *Cofluctuation Events* The degree of coactivity in the dynamics of the mean and its standard deviation was measured between pairs of channels from minimum to maximum physical separation and this exposed short duration 'events' when cofluctuation was unusually high.
- *Event Entropy* Functional significance of cofluctuation events was evaluated by comparing differences in the degree of neural specificity coherence inside and outside of events.

Prevalence of Short-Lived Cofluctuations in SG Activity in HF

In prior work, we identified neural specificity toward near-peak systole of the LVP waveform in control animals (***Sudarshan et al., 2021***). Application of this metric and the construction of a related coherence measure provided insight into differences in neural processing dynamics between control and HF animals. Our results show that cardiac control exerted within diseased states has greater variation in entropy and thus less consistency for heart failure animals compared to control animals. This finding may extend to other pathologies for which the cardiac control hierarchy is disrupted.

Neural Network Activity is Linked to Cardiac Control

Based on the effect size (d_{RM}), event entropy magnitude appears to be higher with greater variation observed in HF animals compared to control animals (Fig. 8B-D). This implies a level of increased unpredictability and increased difficulty in cardiac control for animals in heart failure over control animals.

A limitation of this result is that the effect sizes for event versus non-event comparisons are small to medium, which potentially indicates a larger study is necessary to better understand the physiological contributions from event type. Another limitation of the study lies in the absence of multiple-class pathologies (i.e., different heart failure models or other reproducible models) and in the absence of stratified pathologies (i.e., animal models with varying degrees of heart failure). Measurement of these neurocardiac metrics during slow, quasi-static application of clinically-relevant stressors (***Akeju and Brown, 2017***; ***Chamadia et al., 2019***) should provide unique opportunities to investigate unresolved questions. Future studies should focus on expanding the dataset to examine how these metrics change with varying pathologies or varying disease models. We also cannot exclude possible effects of general anesthesia, open chest and open pericardial effects on our findings, though the effects are likely consistent across the groups studied in the same manner.

Conclusion

In this study, we looked, for the first time to our knowledge, at long-term studies of in vivo cardiac control in baseline states. The baseline states provide unique signatures that differentiate animals with heart failure and controls. We discovered the inputs (i.e., neural signals) and outputs (i.e., blood pressure) are linked, which led us to develop metrics to analyze the dynamical state of this networked control (***Gurel et al., 2022***). The primary observation has been that event-based processing within the stellate ganglion and its relationship to cardiac control is strongly modified by heart failure pathology. Our analysis is pointing to heart failure being best considered as a spectrum rather than a binary state. The magnitude of cofluctuation and neural specificity may give us a measure of the degree of heart failure and insight the extent to which cardiac control is compromised with respect to neural specificity and/or cofluctuation. Future therapies may benefit from being able to infer the degree of heart failure in terms neural markers as represented in this work, in a less invasive way. Intriguing connections involve the alignment of our work with a growing consensus in neuroscience. Spatiotemporal changes in neural activity and linkages with control targets are associated with behavioral changes and the onset and development of specific pathologies. For instance, spatiotemporal brain-wide cofluctuations were reported to reveal major depression vulnerability (***Hultman et al., 2018***). Neural ensembles were linked to visual stimuli in mice ***Miller et al.*** (***2014***). Another study reported that brain's functional connectivity is driven by high-amplitude cofluctuations and that these cofluctuations encode subject-specific information during experimental tasks (***Esfahlani et al., 2020***). Similar cofluctuations were also reported to inform olivary network dynamics in the form of state changes in learning new motor patterns in mice (***Wagner et al., 2021***). Unique co-activation patterns in spontaneous brain activity indicated a signature for conscious states in mice (***Gutierrez-Barragan et al., 2022***). Global brain activity has also been linked to higher level social behaviours (***Mague et al., 2022***). These parallel conclusions in cardiac and neuroscience studies indicate similar experimental methods used to measure neural integration relative to control targets. Such measurements may be instrumental to design and assess the efficacy of neurally-based clinical interventions both at the level of the brain and the stellate ganglion.

Acknowledgments

This work was funded by the National Institutes of Health, Office of The Director DP2 OD024323-01 and NHLBI R01 HL159001. NZG was funded by the National Science Foundation American Society of Engineering Education's Engineering Fellows Postdoctoral Fellowship Award ID #2127509. The authors would like to thank Prof. Jeffrey Ardell for fruitful discussions.

References

Ajijola OA, Chatterjee NA, Gonzales MJ, Gornbein J, Liu K, Li D, Paterson DJ, Shivkumar K, Singh JP, Herring N. Coronary sinus neuropeptide Y levels and adverse outcomes in patients with stable chronic heart failure. JAMA cardiology. 2020; 5(3):318–325.

Ajijola OA, Lellouche N, Bourke T, Tung R, Ahn S, Mahajan A, Shivkumar K. Bilateral cardiac sympathetic denervation for the management of electrical storm. Journal of the American College of Cardiology. 2012; 59(1):91–92.

Ajijola OA, Wisco JJ, Lambert HW, Mahajan A, Stark E, Fishbein MC, Shivkumar K. Extracardiac neural remodeling in humans with cardiomyopathy. Circulation: Arrhythmia and Electrophysiology. 2012; 5(5):1010–1116.

Ajijola OA, Yagishita D, Patel KJ, Vaseghi M, Zhou W, Yamakawa K, So E, Lux RL, Mahajan A, Shivkumar K. Focal myocardial infarction induces global remodeling of cardiac sympathetic innervation: neural remodeling in a spatial context. American Journal of Physiology-Heart and Circulatory Physiology. 2013; 305(7):H1031–H1040.

Ajijola OA, Yagishita D, Reddy NK, Yamakawa K, Vaseghi M, Downs AM, Hoover DB, Ardell JL, Shivkumar K. Remodeling of stellate ganglion neurons after spatially targeted myocardial infarction: neuropeptide and morphologic changes. Heart Rhythm. 2015; 12(5):1027–1035.

Akeju O, Brown EN. Neural oscillations demonstrate that general anesthesia and sedative states are neurophysiologically distinct from sleep. Current opinion in neurobiology. 2017; 44:178–185.

Ardell J, Andresen M, Armour J, Billman G, Chen PS, Foreman R, Herring N, O'leary D, Sabbah HN, Schultz HD, et al. Translational neurocardiology: preclinical models and cardioneural integrative aspects. The Journal of physiology. 2016; 594(14):3877–3909.

Armour J. Synaptic transmission in the chronically decentralized middle cervical and stellate ganglia of the dog. Canadian journal of physiology and pharmacology. 1983; 61(10):1149–1155.

Armour J. Activity of in situ stellate ganglion neurons of dogs recorded extracellularly. Canadian journal of physiology and pharmacology. 1986; 64(2):101–111.

Armour J, Collier K, Kember G, Ardell J. Differential selectivity of cardiac neurons in separate intrathoracic autonomic ganglia. American Journal of Physiology-Regulatory, Integrative and Comparative Physiology. 1998; 274(4):R939–R949.

Blaye-Felice MS, Hamon D, Sacher F, Pascale P, Rollin A, Duparc A, Mondoly P, Derval N, Denis A, Cardin C, et al. Premature ventricular contraction-induced cardiomyopathy: related clinical and electrophysiologic parameters. Heart Rhythm. 2016; 13(1):103–110.

Chamadia S, Pedemonte JC, Hahm EY, Mekonnen J, Ibala R, Gitlin J, Ethridge BR, Qu J, Vazquez R, Rhee J, et al. Delta oscillations phase limit neural activity during sevoflurane anesthesia. Communications biology. 2019; 2(1):1–10.

Chen WW, Xiong XQ, Chen Q, Li YH, Kang YM, Zhu GQ. Cardiac sympathetic afferent reflex and its implications for sympathetic activation in chronic heart failure and hypertension. Acta Physiologica. 2015; 213(4):778–794.

Deyell MW, Krahn AD, Goldberger JJ. Sudden cardiac death risk stratification. Circulation research. 2015; 116(12):1907–1918.

Esfahlani FZ, Jo Y, Faskowitz J, Byrge L, Kennedy DP, Sporns O, Betzel RF. High-amplitude cofluctuations in cortical activity drive functional connectivity. Proceedings of the National Academy of Sciences. 2020; 117(45):28393–28401.

Gao L, Pan YX, Wang WZ, Li YL, Schultz HD, Zucker IH, Wang W. Cardiac sympathetic afferent stimulation augments the arterial chemoreceptor reflex in anesthetized rats. Journal of Applied Physiology. 2007; 102(1):37–43.

Gao L, Schultz HD, Patel KP, Zucker IH, Wang W. Augmented input from cardiac sympathetic afferents inhibits baroreflex in rats with heart failure. Hypertension. 2005; 45(6):1173–1181.

Gurel NZ, Sudarshan KB, Tam S, Ly D, Armour JA, Kember G, Ajijola OA. Studying Cardiac Neural Network Dynamics: Challenges and Opportunities for Scientific Computing. Frontiers in Physiology. 2022; p. 798.

Gutierrez-Barragan D, Singh NA, Alvino FG, Coletta L, Rocchi F, De Guzman E, Galbusera A, Uboldi M, Panzeri S, Gozzi A. Unique spatiotemporal fMRI dynamics in the awake mouse brain. Current Biology. 2022; 32(3):631–644.

Han S, Kobayashi K, Joung B, Piccirillo G, Maruyama M, Vinters HV, March K, Lin SF, Shen C, Fishbein MC, et al. Electroanatomic remodeling of the left stellate ganglion after myocardial infarction. Journal of the American College of Cardiology. 2012; 59(10):954–961.

Hori Y, Temma T, Wooten C, Sobowale C, Chan C, Swid M, Ajijola OA. Cardiac afferent signaling partially underlies premature ventricular contraction–induced cardiomyopathy. Heart Rhythm. 2021; 18(9):1586–1595.

Hultman R, Ulrich K, Sachs BD, Blount C, Carlson DE, Ndubuizu N, Bagot RC, Parise EM, Vu MAT, Gallagher NM, et al. Brain-wide electrical spatiotemporal dynamics encode depression vulnerability. Cell. 2018; 173(1):166–180.

Kember G, Armour JA, Zamir M. Neural control hierarchy of the heart has not evolved to deal with myocardial ischemia. Physiological genomics. 2013; 45(15):638–644.

Lakens D. Calculating and reporting effect sizes to facilitate cumulative science: a practical primer for t-tests and ANOVAs. Frontiers in psychology. 2013; p. 863.

Ma R, Zucker IH, Wang W. Central gain of the cardiac sympathetic afferent reflex in dogs with heart failure. American Journal of Physiology-Heart and Circulatory Physiology. 1997; 273(6):H2664–H2671.

Mague SD, Talbot A, Blount C, Walder-Christensen KK, Duffney LJ, Adamson E, Bey AL, Ndubuizu N, Thomas GE, Hughes DN, et al. Brain-wide electrical dynamics encode individual appetitive social behavior. Neuron. 2022; 110(10):1728–1741.

MATLAB. version 7.10.0 (R2010a). Natick, Massachusetts: The MathWorks Inc.; 2021.

Mehra R, Tjurmina OA, Ajijola OA, Arora R, Bolser DC, Chapleau MW, Chen PS, Clancy CE, Delisle BP, Gold MR, et al. Research Opportunities in Autonomic Neural Mechanisms of Cardiopulmonary Regulation: A Report From the National Heart, Lung, and Blood Institute and the National Institutes of Health Office of the Director Workshop. JACC: Basic to Translational Science. 2022; .

Miller JeK, Ayzenshtat I, Carrillo-Reid L, Yuste R. Visual stimuli recruit intrinsically generated cortical ensembles. Proceedings of the National Academy of Sciences. 2014; 111(38):E4053–E4061.

Nakamura K, Ajijola OA, Aliotta E, Armour JA, Ardell JL, Shivkumar K. Pathological effects of chronic myocardial infarction on peripheral neurons mediating cardiac neurotransmission. Autonomic Neuroscience. 2016; 197:34–40.

Pinheiro JC, Bates DM. Unconstrained parametrizations for variance-covariance matrices. Statistics and computing. 1996; 6(3):289–296.

Sudarshan KB, Hori Y, Swid MA, Karavos AC, Wooten C, Armour JA, Kember G, Ajijola OA. A novel metric linking stellate ganglion neuronal population dynamics to cardiopulmonary physiology. American Journal of Physiology-Heart and Circulatory Physiology. 2021; 321(2):H369–H381.

Vaseghi M, Barwad P, Malavassi Corrales FJ, Tandri H, Mathuria N, Shah R, Sorg JM, Gima J, Mandal K, Sàenz Morales LC, et al. Cardiac sympathetic denervation for refractory ventricular arrhythmias. Journal of the American College of Cardiology. 2017; 69(25):3070–3080.

Vaseghi M, Zhou W, Shi J, Ajijola OA, Hadaya J, Shivkumar K, Mahajan A. Sympathetic innervation of the anterior left ventricular wall by the right and left stellate ganglia. Heart rhythm. 2012; 9(8):1303–1309.

Virtanen P, Gommers R, Oliphant TE, Haberland M, Reddy T, Cournapeau D, Burovski E, Peterson P, Weckesser W, Bright J, et al. SciPy 1.0: fundamental algorithms for scientific computing in Python. Nature methods. 2020; 17(3):261–272.

Wagner MJ, Savall J, Hernandez O, Mel G, Inan H, Rumyantsev O, Lecoq J, Kim TH, Li JZ, Ramakrishnan C, et al. A neural circuit state change underlying skilled movements. Cell. 2021; 184(14):3731–3747.

Wang HJ, Rozanski GJ, Zucker IH. Cardiac sympathetic afferent reflex control of cardiac function in normal and chronic heart failure states. The Journal of physiology. 2017; 595(8):2519–2534.

Wang HJ, Wang W, Cornish KG, Rozanski GJ, Zucker IH. Cardiac sympathetic afferent denervation attenuates cardiac remodeling and improves cardiovascular dysfunction in rats with heart failure. Hypertension. 2014; 64(4):745–755.

Wang W, Zucker IH. Cardiac sympathetic afferent reflex in dogs with congestive heart failure. American Journal of Physiology-Regulatory, Integrative and Comparative Physiology. 1996; 271(3):R751–R756.

Wang WZ, Gao L, Wang HJ, Zucker IH, Wang W. Interaction between cardiac sympathetic afferent reflex and chemoreflex is mediated by the NTS AT1 receptors in heart failure. American Journal of Physiology-Heart and Circulatory Physiology. 2008; 295(3):H1216–H1226.

Yoshie K, Rajendran PS, Massoud L, Kwon O, Tadimeti V, Salavatian S, Ardell JL, Shivkumar K, Ajijola OA. Cardiac vanilloid receptor-1 afferent depletion enhances stellate ganglion neuronal activity and efferent sympathetic response to cardiac stress. American Journal of Physiology-Heart and Circulatory Physiology. 2018; 314(5):H954–H966.

Yoshie K, Rajendran PS, Massoud L, Mistry J, Swid MA, Wu X, Sallam T, Zhang R, Goldhaber JI, Salavatian S, et al. Cardiac TRPV1 afferent signaling promotes arrhythmogenic ventricular remodeling after myocardial infarction. JCI insight. 2020; 5(3).

Supplementary Material 1

Cofluctuation and Event Rate Definitions

Coactivity Matrix

A $16x16$ correlation matrix, $4x4$ version is shown in Fig. 3B for $n = 4$ channels, is used to investigate spatial coherence among neural populations in different regions of the SG spanned by 16 electrodes (Supplementary Fig. 1). The coactivity matrix at each timestamp is found from Pearson's cross-correlation between all possible pairs of spike rate, causal channel, sliding mean and standard deviation. The sliding mean and standard deviation of spike rate are $Spike_{RateMEAN}$ and $Spike_{RateSTD}$, and are on the y-axis of Fig. 3A. These are referred to as 'spike rate' in what follows when both are implied. To fix ideas, consider Pearson's cross correlation coefficient (R) between channels 1 and 2, labeled as R_{12}: namely, the red and blue windows respectively in Fig. 3A. In the coactivity matrix depicted in Fig. 3B, there are $n = 4$ channels, hence $n - 1 = 3$ super-diagonals. These are vertically stacked in Fig. 3C at each timestamp beginning with the first super-diagonal as R_{12}, R_{23}, R_{34}. In this way, adjacent channels are placed at the bottom followed by super-diagonals corresponding to 2 and 3 channels of separation. The super-diagonal of the 16-channel LMA electrode correlation matrix has $n = 16$ channels separated by $500\mu m$ and $n(n-1)/2 = 120$ possible pairwise correlations (See Supplementary Fig. 1 for an example). This yields 120 rows in the stacked version of the coactivity matrix at each timestamp analogous to the same visualized in Fig. 3C for $n = 4$ channels.

Cofluctuations and Event Rate

The univariate cofluctuation time series is the percentage of coactivity matrix members, at each timestamp, that exceed a threshold Pearson's $R > C$, depicted in Fig. 3D. Discrete events are considered to begin at a time of up-crossing of the univariate cofluctuation time series through a threshold T. Each event ends at a down-crossing some time later, as shown in Fig. 3E. These discrete events capture spatiotemporal zones of high SG coactivity. Up-crossing times are respectively converted to an event rate (ER_{MEAN}, ER_{STD}) for the ($Spike_{RateMEAN}$, $Spike_{RateSTD}$) over a duration

$$(ER_{MEAN}, ER_{STD}) = \frac{(N_{MEAN}, N_{STD})}{EventsDuration} \tag{3}$$

where event rate, ER, has units $1/s$ and (N_{MEAN}, N_{STD}) are the number of upcrossings within the $EventsDuration$ considered.

Cofluctuation Probability Distribution

The cofluctuation time series at each threshold C (as in Fig. 3D) qualitatively approximates a log-normal distribution. The log-normal fits of cofluctuation time series (Fig. 5) are obtained using Python SciPy package, with statistics and random numbers module (scipy.stats) (***Virtanen et al., 2020***).

Bootstrapping and Selection of Convergent Thresholds

The event rate is calculated based on a pair of thresholds (C, T). The first threshold (C, Fig. 3D) is used to reduce the coactivity time series of matrices to a univariate cofluctuation time series. The univariate series is the percentage of coactivity matrix entries exceeding C at each timestamp. The cofluctuation time series is then used to define regions of high cofluctuation based on intervals where the time series exceeds a second threshold T. These regions are discrete 'events' that begin and end when the cofluctuation time series respectively up- and down-crosses through T (Fig. 3D). Bootstrapping of the event up-crossing timestamps is used to construct the event rate histogram of a threshold pair (C, T).

These histograms lead to a convergent choice of threshold pairs (C, T). The convergent (C, T) pair is taken as the location in (C, T) space where the confidence interval (CI) width shows apparent convergence. An upper bound on (C, T) is imposed so that there is sufficient data to compute the desired statistics.

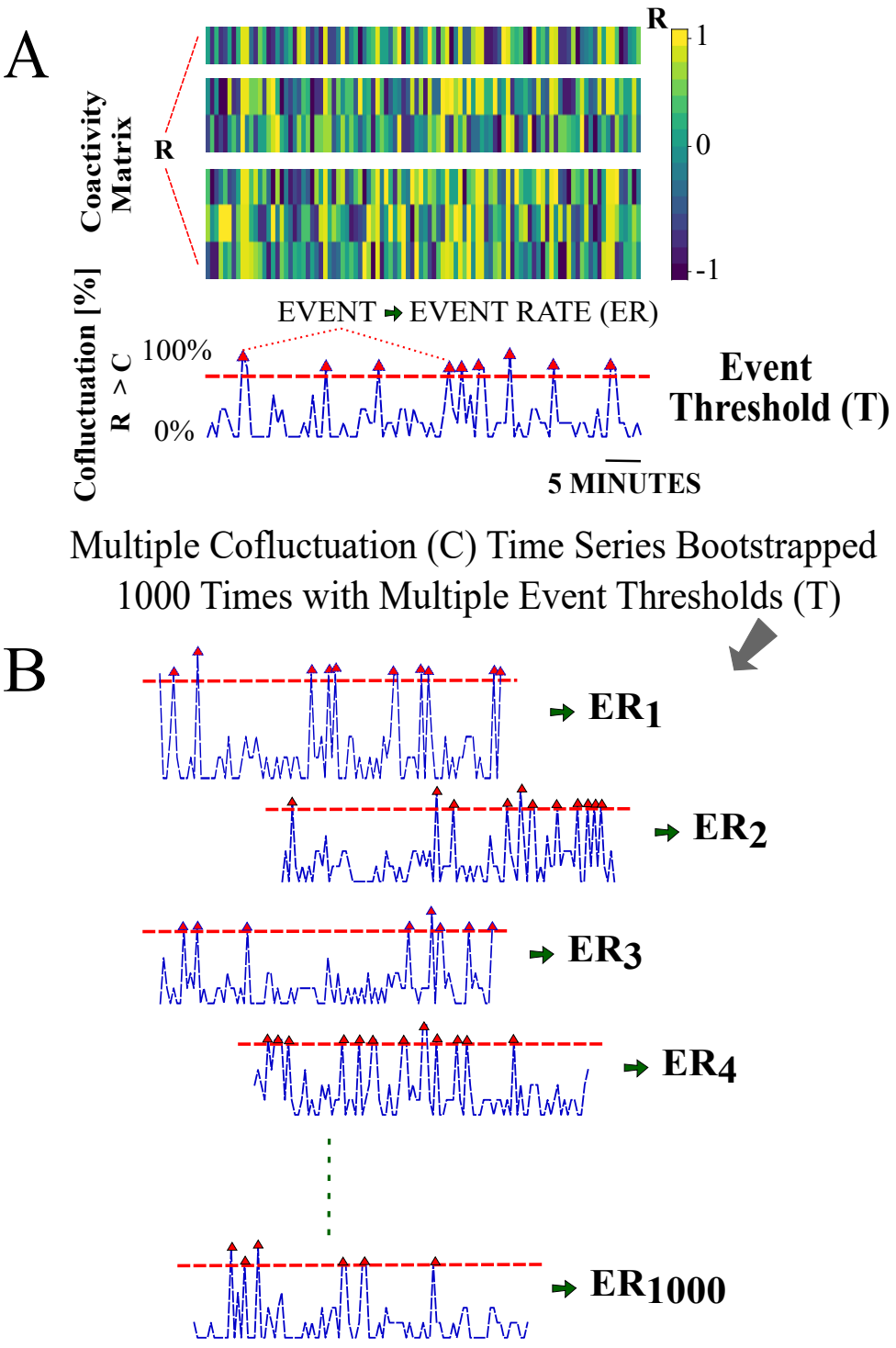

Fig. S1. Cofluctuation bootstrapping pipeline for individualized event rate (ER) for each animal - Part I. A) Coactivity matrix and cofluctuation time series for a cofluctuation threshold and event threshold pair (C, T). B) Cofluctuation time series with depicted events (red triangles are upcrossing timestamps) for a range of (C, T) pairs. Fig. S1A is further explained in Supplementary Figure labelled Fig. S5.

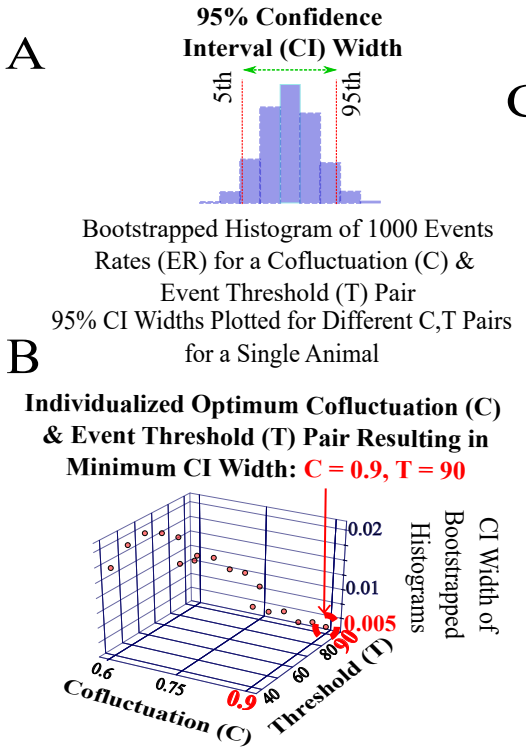

C

	Animal#	Optimum Cofluctuation (C)	Optimum Threshold (T)	Minimum CI Width
HEART FAILURE MODEL	1	0.9	70	0.005
	2	0.9	90	0.018
	3	0.75	90	0.003
	4	0.9	90	0.014
	5	0.9	90	0.003
	6	0.9	90	0.026
	7	0.9	90	0.011
	8	0.9	90	0.009
	9	0.9	90	0.014
	10	0.9	90	0.014
	11	0.9	90	0.004
CONTROL	1	0.9	60	0.001
	2	0.9	90	0.002
	3	0.75	90	0.004
	4	0.9	90	0.006
	5	0.9	90	0.004
	6	0.9	90	0.003

Fig. S2. Cofluctuation bootstrapping pipeline for individualized event rate (ER) for each animal - Part II. A) Bootstrapped histogram of ERs for a single (C,T) pair with 95% confidence interval (CI) width. B) Threshold pair (C,T) is chosen for an animal given non-zero ER and ER convergence. Depicted CI widths are found at all of the depicted 18 (C,T) pairs available on the axes grid. C) List of (C,T) pairs that show ER convergence with CI widths for each animal.

The procedure is visualized in Fig. S1A using a surrogate coactivity matrix R. Univariate cofluctuation time series are created from a range of thresholds C that inclusively vary over 60-90% with 15% increments. Discrete events are determined, shown as red up-crossing triangles in Fig. S1 A-B, for each of the thresholds C and considered over an inclusive range 40-90% with 10% increments of event thresholds T. Bootstrapped events provided the associated ER histogram of each (C,T) threshold pair and desired 95% CI width of each animal (Fig. S2A). A convergent (C,T) pair for an animal is provided in Fig. S2B $(C,T=0.9,90)$, that converged to a 95% CI width of 0.005. Following this approach, convergent (C,T) pairs and bootstrapped CI widths are listed for each animal in Fig. S2C.

Using these individualized convergent (C,T) pairs, original (i.e., not bootstrapped) data are used to calculate event rates for each animal. Note that event rates are calculated from both spike rate mean and standard deviation coactivity matrices, and referred to as ER_{MEAN} and ER_{STD}. These are then used in statistical analyses (one ER_{MEAN} and one ER_{STD} per animal) as shown in Fig. 2. A similar procedure was performed in the literature using neuroimaging time series data based on Pearson's R (***Esfahlani et al., 2020***) however the threshold selection process was qualitative. In this work, we have developed a quantitative approach for threshold selection.

Neural Specificity

The neural specificity metric (***Sudarshan et al., 2021***), Figs. S3 and S4, is used to evaluate the degree to which neural activity is biased toward control target states taken here as LVP. Briefly, this metric is computed in three stages

1. *Neural Sampling* The value of the target state (LVP) is 'sampled' at the timestamp of each spike occurrence. This sampling is assumed to approximate a quasi-stationary distribution over a causal (backward in time) sliding window of spiking activity that is updated at each new timestamp. The distribution is approximated as a normalized and sliding histogram of neurally sampled target states (LVP).
2. *Random Sampling* The normalized, sliding random sampling histogram is found at each spike occurrence in (1), but based on *all* available LVP samples within the same causal window referenced in (1), which approximates the random sampling limit.
3. *Neural Specificity* The normalized, sliding random sampling histogram (2) is subtracted from its neural sampling counterpart (1) to form the neural specificity contrastive measure.

Subtraction of the random sampling histogram from the neural sampling histogram allows for the discovery of the degree to which neural activity is biased, or specific, toward sampling control target states (LVP here) relative to random sampling. To explain the construction of the metric with LVP, a representative window is shown in Fig. S3A with the spikes shown as green dots over LVP waveform. The following steps outline the construction of the neural specificity metric, A, for a representative LVP window

1. *Neural Sampling*
   Following (***Sudarshan et al., 2021***), the normalized sliding window histogram of neurally sampled LVP_j at all spike times t_j and taken over M bins is defined for bin k as

$$H(SLVP_j)_k = \frac{h(SLVP_j)_k}{\Sigma_{k=1}^{k=m} h(SLVP_j)_k} \tag{4}$$

   Eq. (4) approximates the distribution of neural sampling of the target LVP at the green dots over a causal window in Fig. S3A. The resulting normalized histogram shown for one timestamp (green line) in Fig. S3B.
2. *Random Sampling* The normalized sliding window histogram at the random sampling limit of LVP_j is computed as in (1), but based on *all* LVP samples within the same causal window and defined as $H(LVP_j)_k$. This is depicted as sampling of the pink line in Fig. S3A over the

same causal window used to describe neural sampling of LVP. The result is shown for one timestamp as the normalized histogram (pink line) in Fig. S3B.

3. *Neural Specificity* The neural specificity, A_{jk}, for bin k is

$$A_{jk} = H(SLVP_j)_k - H(LVP_j)_k \tag{5}$$

A_{jk} is mapped to three levels $(less,\ same,\ greater)$ relative to random sampling. These are respectively defined as $(-1, 0, 1)$ and depicted as $(purple,\ teal,\ yellow)$ in Fig. S3C and S4A. As such, given the mapping threshold $\alpha > 0$ it follows that $(A_{jk} < -\alpha, A_{jk} < \alpha, A_{jk} > \alpha])$ is respectively $(-1, 0, 1)$ implying $(less,\ same,\ greater)$ neural specificity relative to random sampling and visually represented as $(purple,\ teal,\ yellow)$.

Entropy Definitions

Entropy

The neural specificity is reduced from a multivariate signal to a univariate signal by computing the Shannon entropy at each timestamp of the mapped neural specificity metric (Fig. 2), Eq. (5) mapping description). The entropy of the absolute change between adjacent normalized histogram bins is a measure of coherence in neural specificity. The absolute change in the mapped A_{jk} at time t_j and between adjacent bins $(k,\ k+1),\ k = 1, ..., m-1$ is the set $\Delta A_j = (0, 1, 2)$ with members $\Delta A_{ji}, i = 1, 2, 3$. Using a base 3 logarithm to scale the entropy between 0 and 1, the entropy E_j of the difference in the mapped A_{jk} at each timestamp t_j.

$$E_j = -\Sigma_{\Delta A_{ji}=1}^{3} p(\Delta A_{ji}) \ln_3(p(\Delta A_{ji})) \tag{6}$$

This unequally-sampled series is interpolated to the equally-sampled time series E.

Event Entropy

The neural specificity is a measure of specificity, or bias, of neural activity to target states. However, unusually high and short-lived cofluctuations indicate intervals in time, or 'events', when coactivity between channel pairs implies that SG processing has undergone sudden changes. Functional relevance of cofluctuation events is found by considering the extent to which neural specificity to the target (LVP here) is similar or different inside and outside these events.

Therefore, the functional relevance of cofluctuations in SG neural activity is examined by breaking the time-evolution of entropy of neural specificity into regions: 'event' regions (within event intervals) and 'non-event' regions (outside event intervals). The mean and standard deviation of event and non-event entropy time series per channel are computed for each experiment and collectively referred to as 'event entropy' where this is convenient.

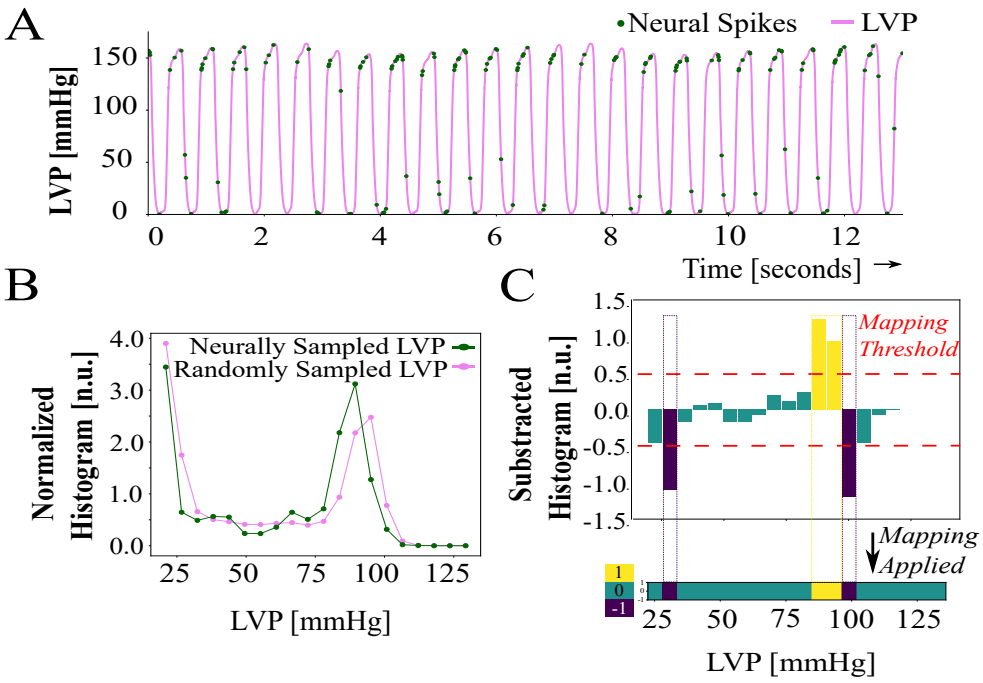

Fig. S3. Neural specificity and entropy computation - Part I. A) Neural specificity sample showing left ventricular pressure (LVP) and neural spikes. Spiking activity is more specific or biased (yellow), over random sampling, to LVP just below systolic pressures. B) Normalized histograms of random and neurally sampled LVP. C) Bars show subtracted histograms and colors indicate the specificity thresholded with $\alpha = 0.5$: specificity exceeding α is yellow, below $-\alpha$ is blue, and between the bounds $(-\alpha, \alpha)$ is teal.

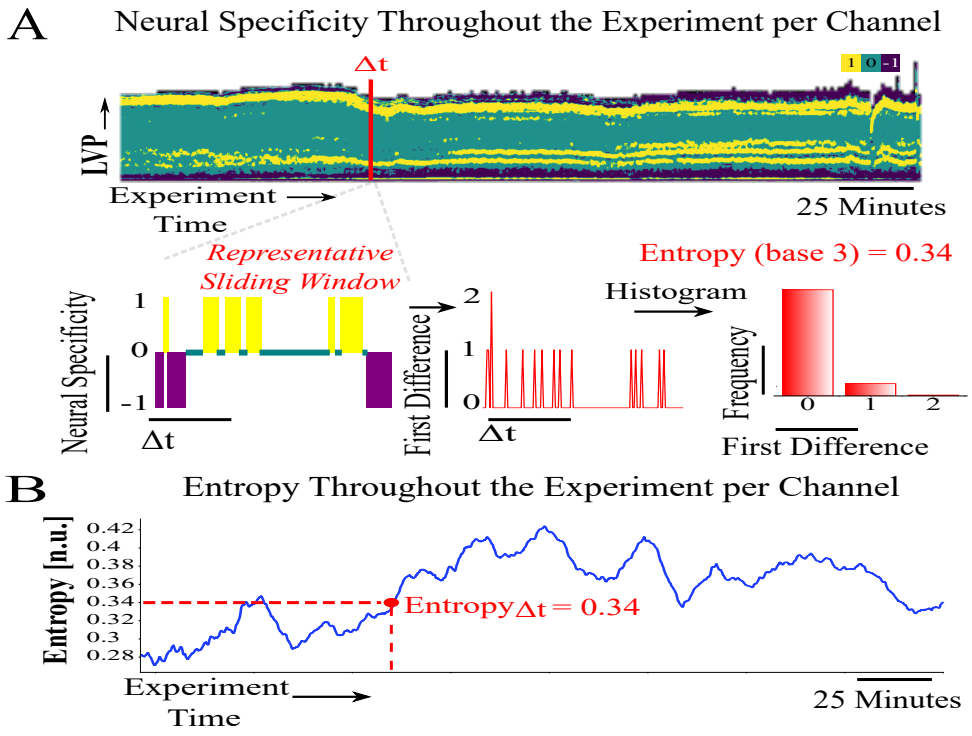

Fig. S4. Neural specificity and entropy computation - Part II. A) Sliding neural specificity time series (top) for a selected sliding window width Δt. Entropy of neural specificity, computed from red highlighted window of width Δt, absolute difference (shown for a sample at bottom). B) Entropy time series corresponding to the overall experiment, entropy sample computed from steps in D. An animated version is in supplementary file 1.

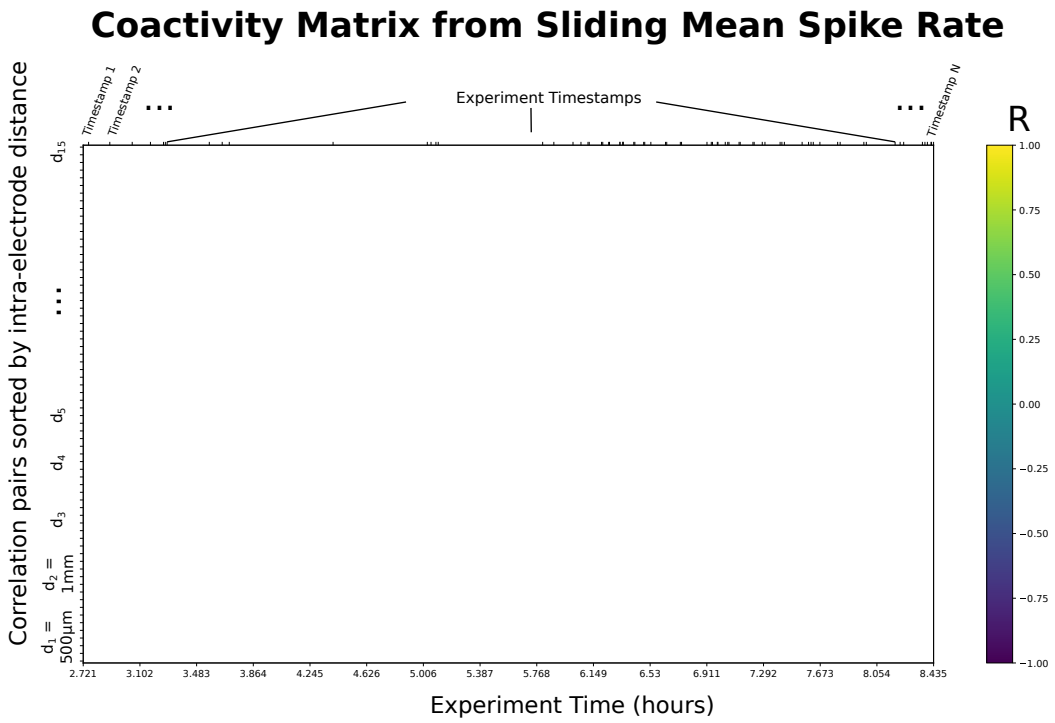

Fig. S5. Supplementary Figure for Fig. S1A. A sample coactivity matrix computed from the sliding (rolling) mean of spike rate for the 16-channel linear mapping array (LMA) used throughout an experiment. Y axis shows correlation pairs (i.e., Channel 1 vs. Channel 2). Correlation pairs are stacked such that the lowest row corresponds to channels separated by the minimum inter-electrode distance ($d_1 = 500\mu m$, 1-electrode away), and inter-electrode distance increasing from a separation of 1 to 15 channels at the top. For instance, the highest row shows the pair separated by the maximum inter-electrode distance ($d_{15} = 15 * 500\mu m = 7.5mm$, 15-electrodes away). The order corresponds to the super-diagonals of the 16 x 16 correlation matrix. Y axis includes 120 comparisons for 16 channels, colors indicate Pearson's correlation coefficients specified in the color legend.

Chapter 5

CONCLUSION

In this thesis, multi-channel, eight hour extracellular recordings from the stellate ganglion were studied with the help of a novel unsupervised spike detection and metrics algorithm. The spike detection algorithm extracted population activity from the stellate in baseline and stressed states in both healthy and diseased animals. This was followed by construction of metrics based on coactivity among populations and specificity to different phases of target data such as LVP and respiratory pressure. Hypotheses based on observations from metrics of both healthy and diseased animals were tested in Chapters 3 and 4.

In Chapter 3, the competitive masking algorithm and the neural specificity metric were developed in Python as an unsupervised multi processing software package. Based on recorded data, populations in the stellate exert integrative control with both cardiac and pulmonary afferent information. Population neural specificity with respect to different phases of LVP and RP showed the extent of integrative control and its dynamics throughout the course of an experiment. The introduction of the neural specificity metric in this work was useful to quantify change in various intrathoracic ganglia population with respect to different target signals and healthy and heart failure animals.

Spatial coherence between neural activities recorded across the stellate ganglion was measured using cofluctuation and event rates in Chapter 4. The coactivity matrix dynamically showed regions of cross correlation between all possible channels pairs in an experiment. Cofluctuation was extracted from the coactivity matrix as the proportion of channel pairs with correlation exceeding a threshold. In order to compare cofluctuations between animal groups, timestamps first exceeding a correlation threshold were defined as events and the corresponding rate was the event rate. Event rates were computed for a windowed mean and variation in spiking activity.

Linkages between the degree of spatial coherence of stellate activity and the corresponding degree of neural specificity to cardiopulmonary targets were also examined. To facilitate this, the neural specificity was reduced to an entropy time series and its mean and variation was compared between animal groups as a function of stellate activity spatial coherence. Higher spatial coherence was interestingly found to be coupled to greater variance in entropy with respect to LVP specificity in diseased animals compared to healthy animals.

The findings in this thesis indicate that spatio-temporal changes in stellate population activity and variations in uncertainty of LVP specificity may represent markers of specific pathologies such as premature ventricular contractions in baseline. This observation within the peripheral nervous systems is strikingly similar to studies of the brain: (i) Within the visual cortex, neural ensembles were reported to be linked to visual stimuli in mice [80], (ii) spatio-temporal changes in local field potentials similar to coactivity predicted major depressive disorder vulnerability in the brain [81], and (iii) high amplitude cofluctuations are suspected of representing functional connectivity in the brain [82]. Such changes observed in spatio-temporal coherence and specificity to control targets might reflect abnormality in cardio pulmonary control by the stellate ganglion in diseased states. Future studies focusing on probing stellate processing around regions of high co fluctuations in baseline and various stressed states would help in understanding open ended questions such as ventricular arrhythmia and sudden cardiac death.

5.1 LIMITATIONS AND FUTURE WORK

The neural specificity metric introduced in Chapter 3 was built to observe dynamics of neural population linkages to a control target. As seen in Chapter 3, stellate neurons integrate afferent information from cardiac and pulmonary regions. With respect to a target signal such as LVP, neural specificity does not indicate the functional type of the neurons as cardiac or pulmonary neurons but overall stellate population specificity to LVP. A majority of stellate neurons are not involved in receiving direct or indirect cardiopulmonary afferent information and sympathetic efferent cardiac outflow as detailed in Chapter 1. Information about neural function type in terms of whether

they receive afferent information, are involved in efferent outflow, or function as interneurons, is unknown and is a major experimental limitation. Future experiments can be designed by targeting activity of neurons based on physiological function to address this limitation.

The competitive masking spike detection algorithm detailed in Chapter 3 extracted population activity from multi channel extracellular recordings in an unsupervised manner. The spikes are detected as event crossing amplitude thresholds in an iterative manner and are not classified based on features such as action potential shapes or physiological function. Future works aimed at adding a spike sorting pipeline would serve to better interpret the metrics developed in the thesis and allow for better understanding of neural recruitment.

Hypotheses tested on the observations in the metrics for stressors performed in the experiments did not yield any statistical significance. This could be due to the short duration of stressors and future experiments could be designed to include long duration stressors in animals.

Other limitations with respect to multi-unit recordings compared to single-unit recordings, translational failure arising from animal models with anesthesia, lack of reproducible research from poor experimental design and a lack of public access data sets and code has been detailed in our latest review [83].

A final limitation lies in animal models not designed with varying degrees of pathology as indicated in Chapter 4 and this can be addressed in future studies.

Bibliography

[1] JA Armour. Physiological behavior of thoracic cardiovascular receptors. *American Journal of Physiology-Legacy Content*, 225(1):177–185, 1973. PMID: 4714399.

[2] J. Andrew Armour and David A. Hopkins. Localization of sympathetic postganglionic neurons of physiologically identified cardiac nerves in the dog. *Journal of Comparative Neurology*, 202(2):169–184, 1981.

[3] D.A Hopkins, P.M Gootman, N Gootman, and J.A Armour. Anatomy of medullary and peripheral autonomic neurons innervating the neonatal porcine heart. *Journal of the Autonomic Nervous System*, 64(2):74–84, 1997.

[4] J. A. Armour. Activity of in situ stellate ganglion neurons of dogs recorded extracellularly. *Canadian Journal of Physiology and Pharmacology*, 64(2):101–111, 1986. PMID: 3697827.

[5] J. A. Armour, K. Collier, G. Kember, and J. L. Ardell. Differential selectivity of cardiac neurons in separate intrathoracic autonomic ganglia. *American Journal of Physiology-Regulatory, Integrative and Comparative Physiology*, 274(4):R939–R949, 1998. PMID: 9575954.

[6] J. L. Ardell, M. C. Andresen, J. A. Armour, G. E. Billman, P.-S. Chen, R. D. Foreman, N. Herring, D. S. O'Leary, H. N. Sabbah, H. D. Schultz, K. Sunagawa, and I. H. Zucker. Translational neurocardiology: preclinical models and cardioneural integrative aspects. *The Journal of Physiology*, 594(14):3877–3909, 2016.

[7] Peter Hanna, Pradeep S Rajendran, Olujimi A Ajijola, Marmar Vaseghi, J Andrew Armour, Jefrrey L Ardell, and Kalyanam Shivkumar. Cardiac neuroanatomy-imaging nerves to define functional control. *Autonomic Neuroscience*, 207:48–58, 2017.

[8] Vasken Dilsizian and Jagat Narula. *Atlas of Cardiac Innervation*. Springer, 2016.

[9] Kalyanam Shivkumar, Olujimi A Ajijola, Inder Anand, J Andrew Armour, Peng-Sheng Chen, Murray Esler, Gaetano M De Ferrari, Michael C Fishbein, Jeffrey J Goldberger, Ronald M Harper, et al. Clinical neurocardiology defining the value of neuroscience-based cardiovascular therapeutics. *The Journal of physiology*, 594(14):3911–3954, 2016.

[10] J. O. Arndt, P. Brambring, K. Hindorf, and M. Röhnelt. The afferent discharge pattern of atrial mechanoreceptors in the cat during sinusoidal stretch of atrial strips in situ. *The Journal of Physiology*, 240(1):33–52, 1974.

[11] D G Baker, H M Coleridge, J C Coleridge, and T Nerdrum. Search for a cardiac nociceptor: stimulation by bradykinin of sympathetic afferent nerve endings in the heart of the cat. *The Journal of Physiology*, 306(1):519–536, 1980.

[12] Stephen R Peters, David R Kostreva, JA Armour, Edward J Zuperku, Franz O Igler, Robert L Coon, and John P Kampine. Cardiac, aortic, pericardial, and pulmonary receptors in the dog. *Cardiology*, 65(2):85–100, 1980.

[13] John Andrew Armour and GC Kember. Cardiac sensory neurons. *Basic and clinical neurocardiology*, pages 79–117, 2004.

[14] A. M. Brown. Excitation of afferent cardiac sympathetic nerve fibres during myocardial ischaemia. *The Journal of Physiology*, 190(1):35–53, 1967.

[15] A Malliani, PJ Schwartz, and A Zanchetti. A sympathetic reflex elicited by experimental coronary occlusion. *American Journal of Physiology-Legacy Content*, 217(3):703–709, 1969. PMID: 5807693.

[16] A. Malliani, G. Recordati, and P. J. Schwartz. Nervous activity of afferent cardiac sympathetic fibres with atrial and ventricular endings. *The Journal of Physiology*, 229(2):457–469, 1973.

[17] Y Uchida. Afferent sympathetic nerve fibers with mechanoreceptors in the right heart. *American Journal of Physiology-Legacy Content*, 228(1):223–230, 1975. PMID: 1147013.

[18] JE Norris, RD Foreman, and RK Wurster. Responses of the canine heart to stimulation of the first five ventral thoracic roots. *American Journal of Physiology-Legacy Content*, 227(1):9–12, 1974. PMID: 4843349.

[19] J. E. Norris, D. Lippincott, and R. D. Wurster. Responses of canine endocardium to stimulation of the upper thoracic roots. *American Journal of Physiology-Heart and Circulatory Physiology*, 233(6):H655–H659, 1977. PMID: 596462.

[20] B. J. Oldfield and Elspeth M. McLachlan. Localization of sensory neurons traversing the stellate ganglion of the cat. *Journal of Comparative Neurology*, 182(5):915–922, 1978.

[21] W.H. Vance and R.C. Bowker. Spinal origins of cardiac afferents from the region of the left anterior descending artery. *Brain Research*, 258(1):96–100, 1983.

[22] David A. Hopkins and J. Andrew Armour. Ganglionic distribution of afferent neurons innervating the canine heart and cardiopulmonary nerves. *Journal of the Autonomic Nervous System*, 26(3):213–222, 1989.

[23] Donald B Hoover, Angela V Shepherd, E Marie Southerland, J Andrew Armour, and Jeffrey L Ardell. Neurochemical diversity of afferent neurons that transduce sensory signals from dog ventricular myocardium. *Autonomic Neuroscience*, 141(1-2):38–45, 2008.

[24] MH Huang, M Horackova, RM Negoescu, S Wolf, and JA Armour. Polysensory response characteristics of dorsal root ganglion neurones that may serve sensory functions during myocardial ischaemia. *Cardiovascular Research*, 32(3):503–515, 1996.

[25] Z J Bosnjak and J P Kampine. Intracellular recordings from the stellate ganglion of the cat. *The Journal of Physiology*, 324(1):273–283, 1982.

[26] J. A. Armour. Synaptic transmission in thoracic autonomic ganglia of the dog. *Canadian Journal of Physiology and Pharmacology*, 61(8):793–801, 1983. PMID: 6138141.

[27] J. A. Armour. Synaptic transmission in the chronically decentralized middle cervical and stellate ganglia of the dog. *Canadian Journal of Physiology and Pharmacology*, 61(10):1149–1155, 1983. PMID: 6315203.

[28] Z. J. Bosnjak, J. L. Seagard, and J. P. Kampine. Peripheral neural input to neurons of the stellate ganglion in dog. *American Journal of Physiology-Regulatory, Integrative and Comparative Physiology*, 242(3):R237–R243, 1982. PMID: 7065217.

[29] Z J Bosnjak and J P Kampine. Cardiac sympathetic afferent cell bodies are located in the peripheral nervous system of the cat. *Circulation Research*, 64(3):554–562, 1989.

[30] J.C. Brandys, D.A. Hopkins, and J.A. Armour. Cardiac responses to stimulation of discrete loci within canine sympathetic ganglia following hexamethonium. *Journal of the Autonomic Nervous System*, 11(3):243–255, 1984.

[31] Z. J. Bosnjak and J. P. Kampine. Electrophysiological and morphological characterization of neurons in stellate ganglion of cats. *American Journal of Physiology-Regulatory, Integrative and Comparative Physiology*, 248(3):R288–R292, 1985. PMID: 2983572.

[32] S. Darvesh, D.M. Nance, D.A. Hopkins, and J.A. Armour. Distribution of neuropeptide-like immunoreactivity in intact and chronically decentralized middle cervical and stellate ganglia of dogs. *Journal of the Autonomic Nervous System*, 21(2):167–180, 1987.

[33] C. Butler, W. M. Watson-Wright, M. Wilkinson, D. E. Johnstone, and J. A. Armour. Cardiac effects produced by long-term stimulation of thoracic autonomic ganglia or nerves: implications for interneuronal interactions within the thoracic autonomic nervous system. *Canadian Journal of Physiology and Pharmacology*, 66(2):175–184, 1988. PMID: 2898282.

[34] C. K. Butler, F. M. Smith, J. Nicholson, and J. A. Armour. Cardiac effects induced by chemically activated neurons in canine intrathoracic ganglia. *American Journal of Physiology-Heart and Circulatory Physiology*, 259(4):H1108–H1117, 1990. PMID: 2221119.

[35] J. A. Armour. Peptidergic modulation of efferent sympathetic neurons in intrathoracic ganglia regulating the canine heart. *Proceedings of the Society for Experimental Biology and Medicine*, 191(1):60–68, 1989.

[36] M Horackova, M H Huang, J A Armour, D A Hopkins, and C Mapplebeck. Cocultures of adult ventricular myocytes with stellate ganglia or intrinsic cardiac neurones from guinea pigs: spontaneous activity and pharmacological properties. *Cardiovascular Research*, 27(6):1101–1108, 06 1993.

[37] M. Horackova, J. A. Armour, D. A. Hopkins, and M. H. Huang. Nitric oxide modulates signaling between cultured adult peripheral cardiac neurons and cardiomyocytes. *American Journal of Physiology-Cell Physiology*, 269(2):C504–C510, 1995. PMID: 7653533.

[38] M. Horackova, R.P. Croll, D.A. Hopkins, A.M. Losier, and J.A. Armour. Morphological and immunohistochemical properties of primary long-term cultures of adult guinea-pig ventricular cardiomyocytes with peripheral cardiac neurons. *Tissue and Cell*, 28(4):411–425, 1996.

[39] M Horackova and JA Armour. Ang ii modifies cardiomyocyte function via extracardiac and intracardiac neurons: in situ and in vitro studies. *The American journal of physiology*, 272:R766–75, 04 1997.

[40] Ian A. Reid. *Vasoactive Peptides*. McGraw-Hill Education, New York, NY, 2017.

[41] Frank Yanowitz, James B. Preston, and J. A. Abildskov. Functional distribution of right and left stellate innervation to the ventricles. *Circulation Research*, 18(4):416–428, 1966.

[42] WALTER C. RANDALL, MATHIAS SZENTIVANYI, JOHN B. PACE, JAMES S. WECHSLER, and MICHAEL P. KAYE. Patterns of sympathetic nerve projections onto the canine heart. *Circulation Research*, 22(3):315–323, 1968.

[43] JA Armour and Walter C Randall. Functional anatomy of canine cardiac nerves. *Acta anatomica*, 91(4):510–528, 1975.

[44] FA Kralios, L Martin, MJ Burgess, and K Millar. Local ventricular repolarization changes due to sympathetic nerve-branch stimulation. *American Journal of Physiology-Legacy Content*, 228(5):1621–1626, 1975. PMID: 1130566.

[45] J. L. Ardell, W. C. Randall, W. J. Cannon, D. C. Schmacht, and E. Tasdemiroglu. Differential sympathetic regulation of automatic, conductile, and contractile tissue in dog heart. *American Journal of Physiology-Heart and Circulatory Physiology*, 255(5):H1050–H1059, 1988. PMID: 3189569.

[46] Tomokazu Kawashima. The autonomic nervous system of the human heart with special reference to its origin, course, and peripheral distribution. *Anatomy and embryology*, 209(6):425–438, 2005.

[47] Ji-Min Cao, Lan S. Chen, Bruce H. KenKnight, Toshihiko Ohara, Moon-Hyoung Lee, Jerome Tsai, William W. Lai, Hrayr S. Karagueuzian, Paul L. Wolf, Michael C. Fishbein, and Peng-Sheng Chen. Nerve sprouting and sudden cardiac death. *Circulation Research*, 86(7):816–821, 2000.

[48] Ji-Min Cao, Michael C. Fishbein, Jay B. Han, William W. Lai, Angela C. Lai, Tsu-Juey Wu, Lawrence Czer, Paul L. Wolf, Timothy A. Denton, I. Peter Shintaku, Peng-Sheng Chen, and Lan S. Chen. Relationship between regional cardiac hyperinnervation and ventricular arrhythmia. *Circulation*, 101(16):1960–1969, 2000.

[49] Peng-Sheng Chen, Lan S Chen, Ji-Min Cao, Behrooz Sharifi, Hrayr S Karagueuzian, and Michael C Fishbein. Sympathetic nerve sprouting, electrical remodeling and the mechanisms of sudden cardiac death. *Cardiovascular Research*, 50(2):409–416, 05 2001.

[50] SHENGMEI ZHOU, JI-MIN CAO, ZACH D. TEBB, TOSHIHIKO OHARA, HSUN-LUN A. HUANG, CHIKAYA OMICHI, MOON-HYOUNG LEE, BRUCE H. KENKNIGHT, LAN S. CHEN, MICHAEL C. FISHBEIN, HRAYR S. KARAGUEUZIAN, and PENG-SHENG CHEN. Modulation of qt interval by cardiac sympathetic nerve sprouting and the mechanisms of ventricular arrhythmia in a canine model of sudden cardiac death. *Journal of Cardiovascular Electrophysiology*, 12(9):1068–1073, 2001.

[51] JEROME TSAI, JI-MIN CAO, SHENGMEI ZHOU, MOSHE SWISSA, ADAM W. CATES, BRUCE H. KENKNIGHT, LAN S. CHEN, HRAYR S. KARAGUEUZIAN, and PENG-SHENG CHEN. T wave alternans as a predictor of spontaneous ventricular tachycardia in a canine model of sudden cardiac death. *Journal of Cardiovascular Electrophysiology*, 13(1):51–55, 2002.

[52] Shengmei Zhou, Lan S. Chen, Yasushi Miyauchi, Mizuho Miyauchi, Saibal Kar, Simon Kangavari, Michael C. Fishbein, Behrooz Sharifi, and Peng-Sheng Chen. Mechanisms of cardiac nerve sprouting after myocardial infarction in dogs. *Circulation Research*, 95(1):76–83, 2004.

[53] Gordon F. Tomaselli and Douglas P. Zipes. What causes sudden death in heart failure? *Circulation Research*, 95(8):754–763, 2004.

[54] Seongwook Han, Kenzaburo Kobayashi, Boyoung Joung, Gianfranco Piccirillo, Mitsunori Maruyama, Harry V. Vinters, Keith March, Shien-Fong Lin, Changyu Shen, Michael C. Fishbein, Peng-Sheng Chen, and Lan S. Chen. Electroanatomic remodeling of the left stellate ganglion after myocardial infarction. *Journal of the American College of Cardiology*, 59(10):954–961, 2012.

[55] Bich Lien Nguyen, Hongmei Li, Michael C. Fishbein, Shien-Fong Lin, Carlo Gaudio, Peng-Sheng Chen, and Lan S. Chen. Acute myocardial infarction induces bilateral stellate ganglia neural remodeling in rabbits. *Cardiovascular Pathology*, 21(3):143–148, 2012.

[56] Olujimi A Ajijola, Jonathan J Wisco, H Wayne Lambert, Aman Mahajan, Elena Stark, Michael C Fishbein, and Kalyanam Shivkumar. Extracardiac neural remodeling in humans with cardiomyopathy. *Circulation: Arrhythmia and Electrophysiology*, 5(5):1010–1116, 2012.

[57] Olujimi A. Ajijola, Daigo Yagishita, Naveen K. Reddy, Kentaro Yamakawa, Marmar Vaseghi, Anthony M. Downs, Donald B. Hoover, Jeffrey L. Ardell, and Kalyanam Shivkumar. Remodeling of stellate ganglion neurons after spatially targeted myocardial infarction: Neuropeptide and morphologic changes. *Heart Rhythm*, 12(5):1027–1035, 2015.

[58] Keijiro Nakamura, Olujimi A. Ajijola, Eric Aliotta, J. Andrew Armour, Jeffrey L. Ardell, and Kalyanam Shivkumar. Pathological effects of chronic myocardial infarction on peripheral neurons mediating cardiac neurotransmission. *Autonomic Neuroscience*, 197:34–40, 2016.

[59] William A. Huang, Noel G. Boyle, and Marmar Vaseghi. Cardiac innervation and the autonomic nervous system in sudden cardiac death. *Cardiac Electrophysiology Clinics*, 9(4):665–679, 2017. Contemporary Challenges in Sudden Cardiac Death.

[60] Marmar Vaseghi, Robert L. Lux, Aman Mahajan, and Kalyanam Shivkumar. Sympathetic stimulation increases dispersion of repolarization in humans with myocardial infarction. *American Journal of Physiology-Heart and Circulatory Physiology*, 302(9):H1838–H1846, 2012. PMID: 22345568.

[61] Marmar Vaseghi, Wei Zhou, James Shi, Olumiji A. Ajijola, Joseph Hadaya, Kalyanam Shivkumar, and Aman Mahajan. Sympathetic innervation of the anterior left ventricular wall by the right and left stellate ganglia. *Heart Rhythm*, 9(8):1303–1309, 2012.

[62] Olujimi A. Ajijola, Daigo Yagishita, Krishan J. Patel, Marmar Vaseghi, Wei Zhou, Kentaro Yamakawa, Eileen So, Robert L. Lux, Aman Mahajan, and Kalyanam Shivkumar. Focal myocardial infarction induces global remodeling of cardiac sympathetic innervation: neural remodeling in a spatial context. *American Journal of Physiology-Heart and Circulatory Physiology*, 305(7):H1031–H1040, 2013. PMID: 23893167.

[63] Daigo Yagishita, Ray W. Chui, Kentaro Yamakawa, Pradeep S. Rajendran, Olujimi A. Ajijola, Keijiro Nakamura, Eileen L. So, Aman Mahajan, Kalyanam Shivkumar, and Marmar Vaseghi. Sympathetic nerve stimulation, not circulating norepinephrine, modulates t-peak to t-end interval by increasing global dispersion of repolarization. *Circulation: Arrhythmia and Electrophysiology*, 8(1):174–185, 2015.

[64] Sumeet S Chugh, Kyndaron Reinier, Carmen Teodorescu, Audrey Evanado, Elizabeth Kehr, Mershed Al Samara, Ronald Mariani, Karen Gunson, and Jonathan Jui. Epidemiology of sudden cardiac death: clinical and research implications. *Progress in cardiovascular diseases*, 51(3):213–228, 2008.

[65] Marmar Vaseghi and Kalyanam Shivkumar. The role of the autonomic nervous system in sudden cardiac death. *Progress in cardiovascular diseases*, 50(6):404, 2008.

[66] Mark J. Shen and Douglas P. Zipes. Role of the autonomic nervous system in modulating cardiac arrhythmias. *Circulation Research*, 114(6):1004–1021, 2014.

[67] Keiichi Fukuda, Hideaki Kanazawa, Yoshiyasu Aizawa, Jeffrey L. Ardell, and Kalyanam Shivkumar. Cardiac innervation and sudden cardiac death. *Circulation Research*, 116(12):2005–2019, 2015.

[68] Douglas P Zipes. Contemporary approaches to treating arrhythmias. *Nature Reviews Cardiology*, 12(2):68–69, 2015.

[69] Olujimi A Ajijola, Nicholas Lellouche, Tara Bourke, Roderick Tung, Samuel Ahn, Aman Mahajan, and Kalyanam Shivkumar. Bilateral cardiac sympathetic denervation for the management of electrical storm. *Journal of the American College of Cardiology*, 59(1):91–92, 2012.

[70] Marmar Vaseghi, Jean Gima, Christopher Kanaan, Olujimi A Ajijola, Alexander Marmureanu, Aman Mahajan, and Kalyanam Shivkumar. Cardiac sympathetic denervation in patients with refractory ventricular arrhythmias or electrical storm: intermediate and long-term follow-up. *Heart rhythm*, 11(3):360–366, 2014.

[71] Marmar Vaseghi, Parag Barwad, Federico J. Malavassi Corrales, Harikrishna Tandri, Nilesh Mathuria, Rushil Shah, Julie M. Sorg, Jean Gima, Kaushik Mandal, Luis C. Sàenz Morales, Yash Lokhandwala, and Kalyanam Shivkumar. Cardiac sympathetic denervation for refractory ventricular arrhythmias. *Journal of the American College of Cardiology*, 69(25):3070–3080, 2017.

[72] Koji Yoshie, Pradeep S. Rajendran, Louis Massoud, Janki Mistry, M. Amer Swid, Xiaohui Wu, Tamer Sallam, Rui Zhang, Joshua I. Goldhaber, Siamak Salavatian, and Olujimi A. Ajijola. Cardiac trpv1 afferent signaling promotes arrhythmogenic ventricular remodeling after myocardial infarction. *JCI Insight*, 5(3), 2 2020.

[73] Yuichi Hori, Taro Temma, Christian Wooten, Christopher Sobowale, Christopher Chan, Mohammed Swid, and Olujimi A. Ajijola. Cardiac afferent signaling partially underlies premature ventricular contraction–induced cardiomyopathy. *Heart Rhythm*, 18(9):1586–1595, 2021. Focus Issue: Atrial Fibrillation.

[74] Joseph Hadaya and Jeffrey L Ardell. Autonomic modulation for cardiovascular disease. *Frontiers in physiology*, 11:617459, 2020.

[75] Michael S. Lewicki. A review of methods for spike sorting: the detection and classification of neural action potentials. *Network*, 9 4:R53–78, 1998.

[76] Hernan Gonzalo Rey, Carlos Pedreira, and Rodrigo Quian Quiroga. Past, present and future of spike sorting techniques. *Brain Research Bulletin*, 119:106–117, 2015. Advances in electrophysiological data analysis.

[77] Baptiste Lefebvre, Pierre Yger, and Olivier Marre. Recent progress in multi-electrode spike sorting methods. *Journal of Physiology-Paris*, 110(4, Part A):327–335, 2016. SI: GDR Multielectrode.

[78] Matthias H. Hennig, Cole Hurwitz, and Martino Sorbaro. *Scaling Spike Detection and Sorting for Next-Generation Electrophysiology*, pages 171–184. Springer International Publishing, Cham, 2019.

[79] Andrew Collette. *Python and HDF5*. O'Reilly, 2013.

[80] Jae eun Kang Miller, Inbal Ayzenshtat, Luis Carrillo-Reid, and Rafael Yuste. Visual stimuli recruit intrinsically generated cortical ensembles. *Proceedings of the National Academy of Sciences*, 111(38):E4053–E4061, 2014.

[81] Rainbo Hultman, Kyle Ulrich, Benjamin D Sachs, Cameron Blount, David E Carlson, Nkemdilim Ndubuizu, Rosemary C Bagot, Eric M Parise, Mai-Anh T Vu, Neil M Gallagher, et al. Brain-wide electrical spatiotemporal dynamics encode depression vulnerability. *Cell*, 173(1):166–180, 2018.

[82] Farnaz Zamani Esfahlani, Youngheun Jo, Joshua Faskowitz, Lisa Byrge, Daniel P. Kennedy, Olaf Sporns, and Richard F. Betzel. High-amplitude cofluctuations in cortical activity drive functional connectivity. *Proceedings of the National Academy of Sciences*, 117(45):28393–28401, 2020.

[83] Nil Z Gurel, Koustubh B Sudarshan, Sharon Tam, Diana Ly, J Andrew Armour, Guy Kember, and Olujimi A Ajijola. Studying cardiac neural network dynamics: Challenges and opportunities for scientific computing. *Frontiers in Physiology*, page 798, 2022.